Electron Method for Touchless Electrostatic Potential Sensing of Neighboring Spacecraft

by

M. T. Bengtson

B.S., Embry-Riddle Aeronautical University, 2016

M.S., Embry-Riddle Aeronautical University, 2017

A thesis submitted to the

Faculty of the Graduate School of the

University of Colorado in partial fulfillment

of the requirements for the degree of

Doctor of Philosophy

Department of Aerospace Engineering Sciences

2020

Committee Members:

Prof. Hanspeter Schaub

Prof. Zoltan Sternovsky

Prof. Delores Knipp

Prof. Robert Marshall

Dr. Emily Bohner

Bengtson, M. T. (Ph.D., Aerospace Engineering Sciences)

Electron Method for Touchless Electrostatic Potential Sensing of Neighboring Spacecraft

Thesis directed by Prof. Hanspeter Schaub

Touchless potential sensing is a technique which can provide valuable insight into spacecraft-environment interactions, enable missions which leverage electrostatic forces and torques between multiple charged spacecraft for relative motion control, and mitigate risk during rendezvous and docking in harsh space environments. This dissertation investigates a promising method for touchless potential sensing in which electrons emitted by a target object are detected and analyzed by a co-orbiting spacecraft. Secondary electrons and photoelectrons are emitted from the target with very small initial energies. The electrons are accelerated toward the sensing spacecraft, which is at a known positive potential relative to the target, where they are measured by an energy analyzer. The ultimate energy of the electron population is equal to the potential difference between the two craft (plus the small initial energy). Thus, given the potential difference between the two craft and the potential of the sensing spacecraft, the potential of the target object is accurately determined.

Both active and passive sensing cases are possible. In the active case, an electron beam is in use to force a charge onto the target. This beam produces secondary electrons which are then measured by the sensing craft to monitor the forced potential of the target. Passive sensing allows for the natural, unforced potential of the target to be measured. In this case, photoelectrons and secondaries produced by the ambient plasma currents are naturally emitted from the target and then measured by the sensing craft.

The prospects, feasibility, and challenges of electron-based touchless potential sensing are analyzed using both theory and simulations. Case studies are presented which show that potential sensing is feasible for a range of relevant operating conditions. Development of an experimental facility is described in detail, followed by discussion of an experimental campaign to demonstrate the efficacy of the electron method for a variety of representative materials and voltages. Both the active

and passive sensing cases are considered. Finally, the effects of target geometry and differential charging on the sensing process are considered. The results of this work will be important for numerous missions in the near-future as humankind looks to extend its presence in geosynchronous orbit, cis-lunar space, and beyond.

Dedication

To the truth. May we seek it, find it, and cherish it.

To my family who taught me to love the truth. Thank you for endless love and support.

Acknowledgements

First and foremost, thank you to my advisor, Dr. Hanspeter Schaub, for his guidance and support. His willingness to support the development and operation of the vacuum chamber allowed me to conduct experiments which made my time at CU particularly rewarding and enjoyable. Thank you to my committee members, Dr. Zoltan Sternovsky, Dr. Delores Knipp, Dr. Robert Marshall, and Dr. Emily Bohner for their guidance and advice on this research. Thank you, Emily, for all of your mentorship and wise advice regarding grad school and career decisions.

To my Master's and undergraduate advisors, Dr. Katariina Nykyri and Dr. Anatoly Strelstov, thank you for giving me a chance to learn about research, teaching me space physics, and inspiring me to pursue a career in research. I gratefully acknowledge the AFRL spacecraft charging group: Dale Ferguson, Ryan Hoffmann, and Dan Engelhart. Thank you for providing so much technical advice these past few years and for the opportunity to postdoc with you. When I interned at AFRL in 2016, I had a brief conversation with Dale in which he recommended that I check out Dr. Schaub's group as a possibility for grad school, so thank you for that tip as well!

I am thankful for my coworkers on the electrostatics team in the AVS Lab. Thank you Jordan Maxwell, Kieran Wilson, and Dalton Turpen for being valuable team members and sounding boards for research challenges. Also, thank you, Dalton, for building so much hardware for the chamber.

Finally, thank you to my Mom and Dad, my sister, Miranda, and my extended family for all of their love and support. I love you all.

I also gratefully acknowledge support from the NDSEG Fellowship for this research.

Contents

Chapter

Tables

Table

Figures

Figure

Chapter 1

Introduction

1.1   Motivation

Though spacecraft charging has been studied for decades, little work has been done on how to remotely sense the charge on a space object. This dissertation investigates a promising method for touchlessly sensing the potential of a space object from a nearby spacecraft dozens of meters away in geosynchronous orbit (GEO) or other high orbits. Numerous applications exist which would greatly benefit from touchless potential sensing capability. First, this technology would enable on-orbit measurements of spacecraft surface charge, providing valuable insight into spacecraft-environment interactions. Most spacecraft do not have sensors to detect when they are charged to large potentials and at risk of arcing which means that identifying causes of satellite anomalies is tenuous [42, 83]. Many future space missions are planned which involve docking and rendezvous maneuvers in GEO or the outer radiation belt. NASA's Lunar Gateway program, for example, requires rendezvous and docking maneuvers to be conducted in harsh charging environments such that expected conditions during docking can produce potential differences of thousands of volts between different spacecraft [50]. This creates substantial risk of electrostatic discharge during first contact as well as unwanted electrostatic forces and torques. Further, as the GEO ring becomes increasingly congested, satellite operators are looking to extend the lifetime of satellites and reduce overall costs by conducting missions to service old satellites or salvage them for parts [35, 44, 94, 119]. In February 2020, the first commercial mission to service and refuel a GEO satellite was successfully completed. Figure 1.1 shows the view from the Mission Extension Vehicle-1 as it approaches Intelsat
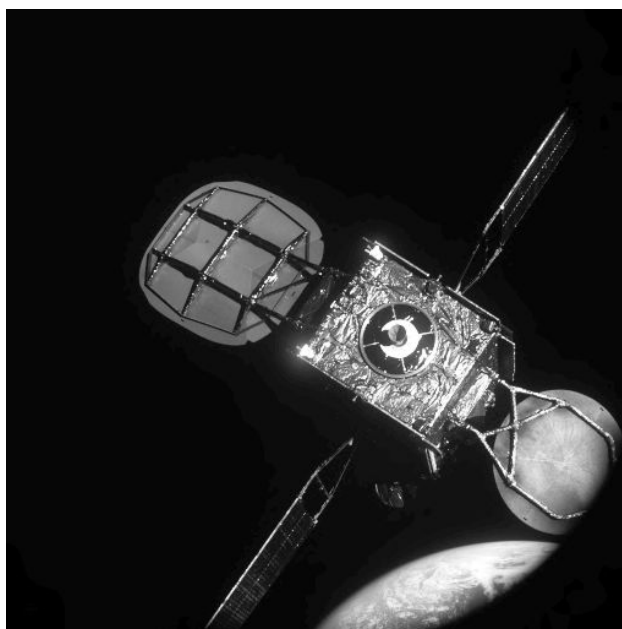
Figure 1.1: Mission Extension Vehicle-1 approaches Intelsat 901 during the first commercial mission extension service in February 2020 (Image credit: Northrop Grumman).

901 from a distance of 20 m[1] . Such missions require multiple spacecraft operating in very close proximity and interfacing with each other. To mitigate the risk of electrostatic discharges and perturbations, it is imperative that the surface potential on each spacecraft be monitored during approach and first contact. Additionally, the space debris problem at GEO has been studied extensively [84, 3, 89], and the need for active debris removal has been clearly established [82]. The electrostatic tractor (ET) is one promising concept which leverages electrostatic interactions between the debris and the tractor for contactless debris removal [100, 9, 5]. Figure 1.2 shows a concept of operation for the ET. This technology offers significant advantages in terms of risk mitigation because the debris can be removed without physical contact between the debris and tractor. Further, Coulomb torques can be used to remotely detumble a spinning debris object prior to making physical contact [16, 15]. Figure 1.3 shows a concept of operations for electrostatic detumbling. Such technologies represent a paradigm shift from previous attitudes toward spacecraft

---

[1] Northrop Grumman Successfully Completes Historic First Docking of Mission Extension Vehicle with Intelsat 901 Satellite, https://news.northropgrumman.com/news/releases/northrop-grumman-successfully-completes-historic-first-docking-of-mission-extension-vehicle-with-intelsat-901-satellite, Accessed 2020-10-03.
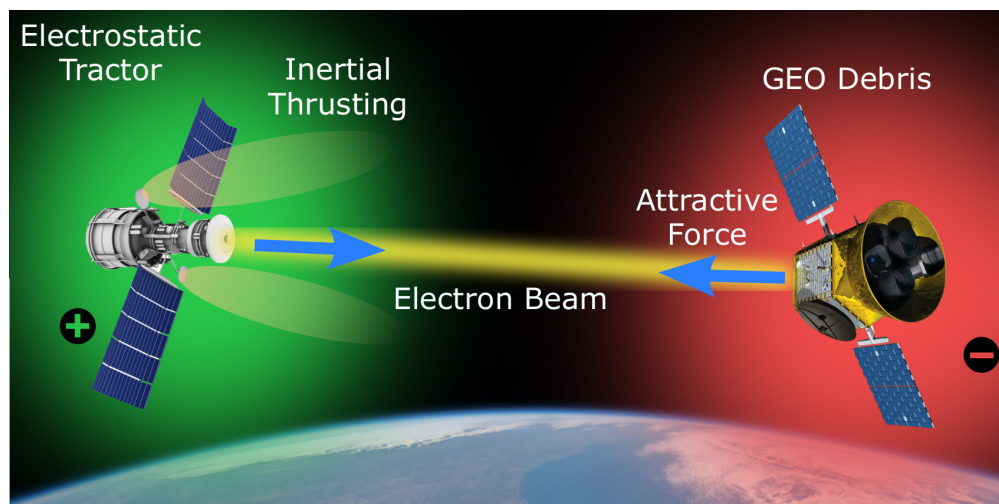
Figure 1.2: Electrostatic tractor concept of operations.

charging because they seek to leverage charged spacecraft to do useful work, rather than trying to mitigate the charging. Similar concepts include using Coulomb forces to electrostatically inflate large gossamer structures [106, 107] and maintenance of charged spacecraft formations without the use of conventional propellant [70, 101]. For these and other technologies which seek to actively use Coulomb forces and torques, there is a strong need for the capability to measure the voltage on another object without making physical contact.

Similarly, Reference [25] shows that there are significant risks of charging and arcing for future human missions to the lunar surface, especially in shadowed regions near the poles which have been targeting for exploration. Without proper precautions, a discharge could occur between an astronaut during extravehicular activity and a large space structure which would be fatal to the astronaut [21]. The potentials of astronauts and other objects must be monitored and controlled to ensure mission safety and success. Another significant challenge for lunar missions is mitigation of lunar dust which sticks to spacesuits, instruments, camera lenses, and other critical surfaces [47]. Recent research proposes the use of electron beams to intentionally charge surfaces and electrostatically remove the dust [38]. This further underscores the need for monitoring and controlling the potential of various surfaces during future crewed missions beyond low Earth orbit (LEO). The ability to remotely sense electrostatic potential on another object is critical to ensure safe proximity
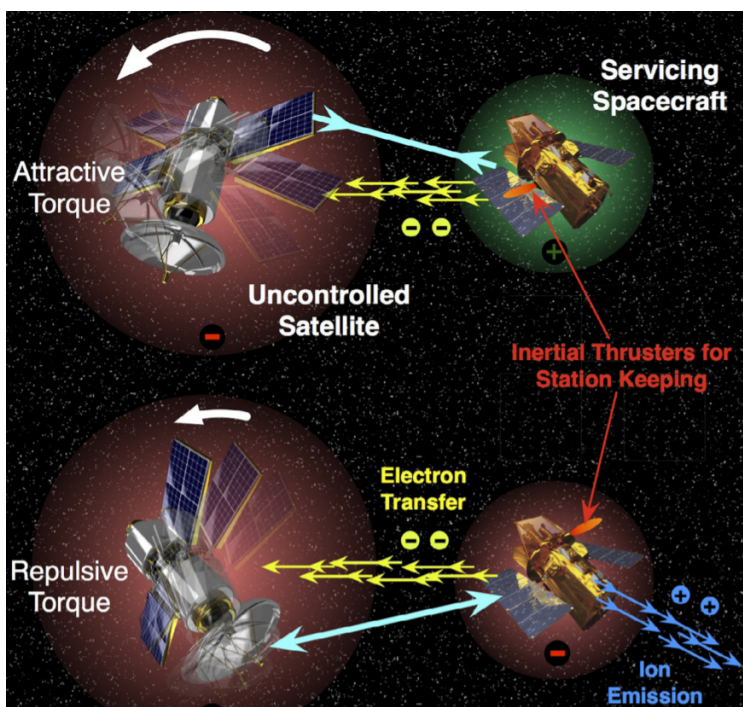
Figure 1.3: Electrostatic detumbling of an uncontrolled space debris object [16].

operations in all regions of the space environment.

This dissertation investigates a method which uses electrons to meet the need for contactless measurement of elecrostatic potential on a nearby space object in GEO or other high orbits. The proposed concept works by using a co-orbiting sensing spacecraft to measure the energies of secondary electrons or photoelectrons which are emitted from a target object [10, 12, 11]. Figure 1.4 provides a concept of operations. Low-energy electrons are generated on the target surface and accelerated toward the sensing spacecraft, which is at a known positive potential, where they are measured by an energy analyzer. The ultimate energy of the electrons is equal to the potential difference through which they are accelerated (plus their small initial energy), which is equal to the potential difference between the two spacecraft. Therefore, given the potential of the sensing spacecraft, the potential of the target can be accurately determined. In low-Earth orbit (LEO), the environmental plasma is cold and dense, which limits natural spacecraft charging and also shields out forces around charged objects within a few centimeters. The electron method is highly appli-
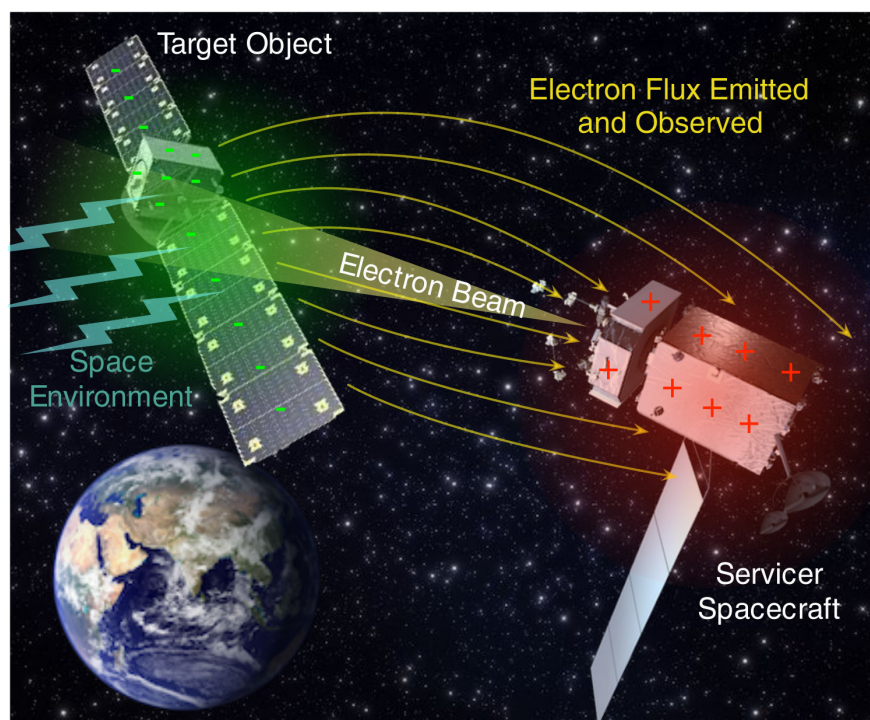
Figure 1.4: Concept figure depicting operation of the electron method for touchless electrostatic sensing.

cable to sparse plasma environments like that at GEO because objects naturally charge to kilovolt level potentials and Debye shielding lengths are on the order of 100s of meters.

Both active and passive sensing modes are possible, depending on the application. In the active case, an electron beam is directed from the sensing craft toward the target object to transfer charge, generating Coulomb forces and torques. Secondary electrons are created on the target surface by the incident electron beam and are then accelerated toward the sensing craft where they are measured. The forced potential of the target is thus determined. Active sensing is highly relevant for applications such as the electrostatic tractor in which an electron beam is already in use to transfer charge. In the passive case, the target surface is exposed to sunlight, which produces photoelectrons, and to environmental electron and proton fluxes, which produce secondary electrons. Both the photoelectrons and secondary electrons are then accelerated away from the target surface and detected by the sensing craft to determine the natural, unforced potential of the target. Passive sensing is useful when the natural potential of a target is to be measured, such as

to determine the risk of electrostatic discharge prior to docking. The touchless sensing concept is most readily applied in space environments with sparse plasma, such as GEO, other high Earth orbits, and cislunar or deep space. In LEO, the cold, dense plasma both limits the magnitude of spacecraft charging and also shields out Coulomb forces over a few centimeters. Thus touchless sensing is not applicable in such environments, so the focus of this work is on sensing in sparse plasma environments.

It is emphasized that the electron sensing method does not require new hardware to be developed, but rather uses existing hardware in novel ways to meet the needs of future space missions. Electron energy analyzers have extensive flight heritage and are ubiquitous on-orbit, both for operational (e.g. [91, 81, 20, 115]) and planned satellites [79, 85, 53].

1.2 Relevant Physics

1.2.1 Spacecraft Charging

Spacecraft become electrically charged through interactions with various currents in the space environment. These currents include the thermal electron and ion currents (I_e, I_i), secondary electron emission, which can be stimulated by both incident electrons and ions (I_{see}), backscattered electron currents (I_{bs}), the photoelectric current when the object is exposed to sunlight (I_{ph}), and currents from any active electron or ion beams (I_{beam}), which could either be directed toward or emitted from a given object. Figure 1.5 shows these currents interacting with a spacecraft. The equilibrium potential of an object is determined by the balance of these currents, which depend on the potential:

$$I_e(\phi) + I_i(\phi) + I_{\text{see}}(\phi) + I_{\text{bs}}(\phi) + I_{\text{ph}}(\phi) + I_{\text{beam}}(\phi) = 0. \tag{1.1}$$

Various theoretical and empirical models are available for each of the currents. Secondary and photo- emission models are discussed in the following sections, and further discussions are available in References [75, 65, 63]. The right-hand side of Equation 1.1 can be made non-zero to consider time-variation of spacecraft charging. However, for typical spacecraft in GEO, equilibrium potential
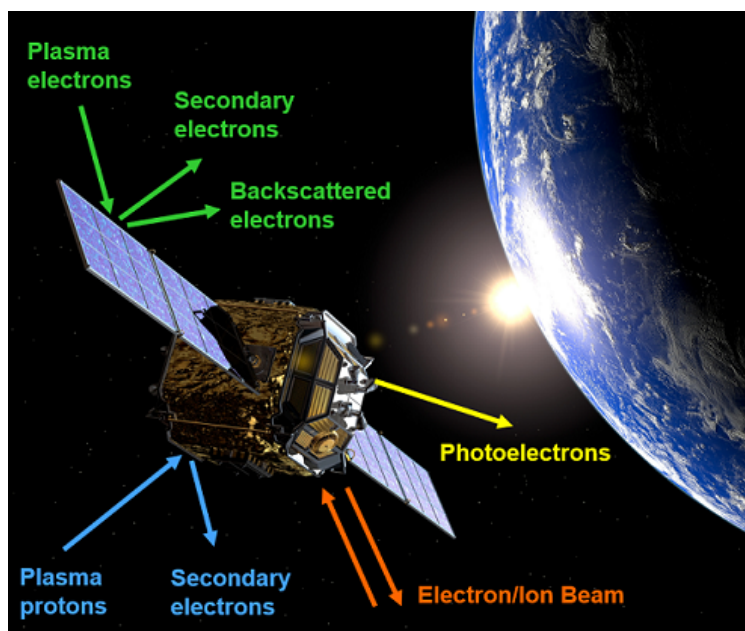
Figure 1.5: The balance of currents determines the equilibrium potential of a spacecraft.

is achieved within a few milliseconds, so it is sufficient here to consider only the equilibrium case [75]. For forced charging applications, such as the electrostatic tractor or space weather missions which seek to constrain charging to a small value, the beam current dominates the other currents and determines the spacecraft potential. In natural charging scenarios, the photoelectron current often dominates.

1.2.2   Secondary Electron Emission

Secondary electrons are created when an energetic electron (known as the primary electron) strikes a surface. The incident particle liberates electrons within the material, some of which escape the surface as secondary electrons (SE's), as shown in Figure 1.6. Alternatively, if the incident electron reflects off the surface, it is a backscattered electron (BSE). Figure 1.7 shows an example spectra obtained by irradiating a surface with an electron beam. The SE spectrum has a peak at one third the work function of the material, which is in the range of 2-3 eV for most surfaces [26].
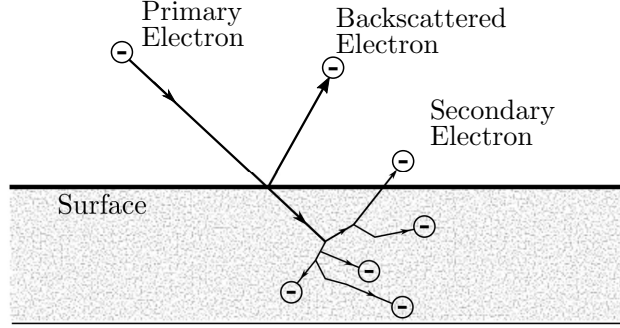
Figure 1.6: Secondary electron and backscatter electron generation.

One commonly used model for the initial energy distribution of SE's is the Chung-Everhart model:

$$f(E) = \frac{(E - E_F - \phi)}{(E_F - E)^4},$$

(1.2)

where $f(E)$ is the relative number of electrons generated, E is the secondary electron energy in eV, E_F is the Fermi energy of the surface material in eV, and ϕ is the work function of the material in eV. Aluminum, for example, has a work function of 4.0 eV and a Fermi energy of 11.7 eV [4]. Conventionally, electrons with energies less than 50 eV are considered SE's whereas electrons with energies from 50 eV to the beam energy are considered BSE's. However, the 50 eV threshold is based primarily in convention, and evidence suggests that SE's may dominate the population at energies greater than 50 eV [29]. The peak of BSE's near the incident beam energy E_0 is due to incident electrons which are scattered nearly elastically. SE's carry almost no information about the incident electrons. The angular distribution of SE's follows a cosine law which is weakly dependent on the primary incidence angle [19].

The number of secondaries emitted for each incident particle is known as the secondary electron yield (SEY or δ), which varies as a function of the incident particle energy. Figure 1.8 shows a typical SEY curve. It is common for materials to have a yield larger than unity for a range of incident energies, known as the crossover points, $E_1 < E_0 < E_2$. This indicates that multiple secondaries are emitted for every incident particle. For an incident beam impacting a surface with landing energies in this range, the surface charges positively, even though it is being bombarded with an electron beam. The maximum number of secondary electrons per primary
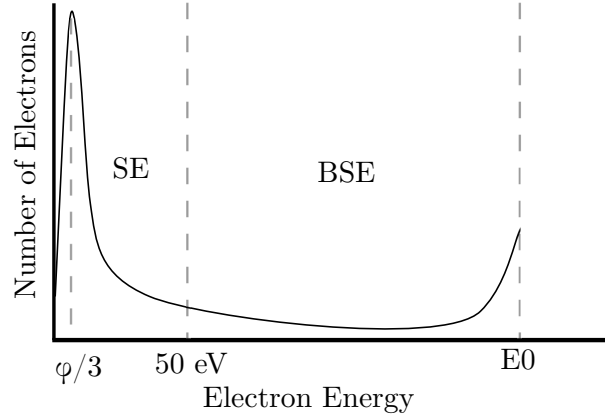
Figure 1.7: Example of an SE and BSE energy spectrum for a typical spacecraft material.

electrons is produced at the maximum point of the yield curve, δ_{max}. Above the energy, E_{max}, higher energy incident primaries produce fewer secondaries, because the energy is deposited deeper in the material where electrons have a lower probability of escaping to the surface. Larger primary incident angles produce larger numbers of secondaries because more energy is deposited closer to the surface (however, the initial angular distribution of the secondaries remains virtually the same).

1.2.3 Photoelectron Emission

Photoelectrons are emitted when light shines on a surface and the energy of the light is greater than the work function of the surface, as expressed by the well-known equation:

$$E = \frac{hc}{\lambda} - \phi, \tag{1.3}$$

where E is the maximum energy of the photoelectron in eV, hc is the product of Planck's constant and the speed of light (equal to 1240 eV nm), λ is the wavelength of the light in nm, and ϕ is the work function of the surface in eV. Initial photoelectron energies are often modeled as a Maxwellian distribution with a temperature of 1-2 eV, though higher energy photons can produce characteristic structure in the spectra [43, 114]. The maximum energy at which a photoelectron can be emitted is always limited by Equation 1.3.

The number of emitted electrons depends on the intensity of the light. In space, the photo-
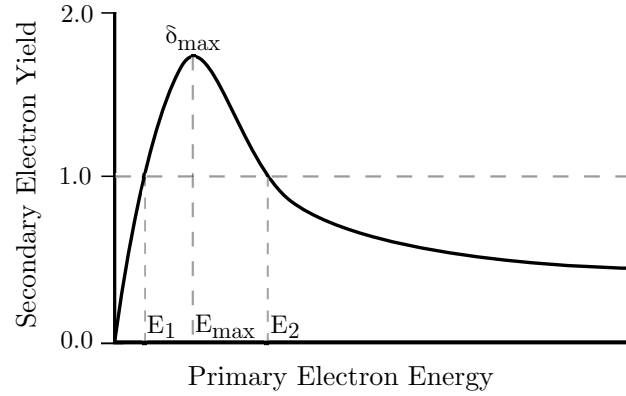
Figure 1.8: Example secondary electron yield curve for a typical spacecraft material.

electron current (when a surface is exposed to sunlight) is given by:

$$I_{\mathrm{ph}} = \begin{cases} j_{\mathrm{ph}} A e^{-qV/k_{\mathrm{B}}T_{\mathrm{ph}}} & V > 0 \\ \\ j_{\mathrm{ph}} A & V \leq 0 \end{cases} \qquad (1.4)$$

where j_{ph} is the photoelectron flux in $\mathrm{A\,m^{-2}}$, A is the sunlit area in $\mathrm{m^2}$, $q\phi$ is the surface potential in eV and $k_B T_{\mathrm{ph}}$ is the thermal energy of the ejected photoelectrons in eV [75]. For objects in Earth orbit, a photoelectron flux in the range of $j_{\mathrm{ph}} = 40\ \mathrm{\mu A\,m^{-2}}$ is commonly assumed [75]. The photocurrent is only emitted from surfaces which are exposed to the sunlight. Note that this current is constant for negatively charged spacecraft and quickly vanishes as the spacecraft charge goes positive, because the photoelectrons are attracted back to the surface.

Figure 1.9 shows an example of the photoelectron yield, Y, as function of photon energy for aluminum [43, 95]. According to Reference [75], a photon incident at an angle relative to the surface normal deposits energy closer to the surface where photoelectrons can more easily escape. Therefore, the photoelectron yield has an angular dependence of the form:

$$Y(\theta) \approx \frac{Y(0)}{\cos\theta}, \qquad (1.5)$$

where $Y(0)$ is the photoelectron yield at normal incidence and θ is the angle of incidence [68]. At the same time, however, the photoemission depends on the surface reflectance, which also varies approximately with a cosine dependence [77]. Therefore, the cosine terms from these two factors
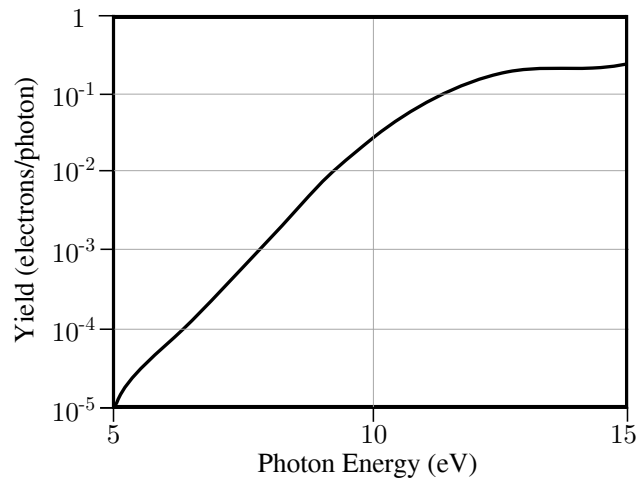
Figure 1.9: Example photoelectron yield curve for Aluminum [95].

cancel each other out. The only remaining angular dependence of photoemission is the cosine term that comes from the effective area being illuminated varying with angle.

Because photoemission depends on surface reflectance, the photoelectron yield also has a strong dependence on surface condition. Rough surfaces and polished surfaces of the same material may charge to very different potentials in the same space conditions [74]. Further, photoemission takes place in the first few atomic layers of a surface, so the presence of oxide layers and other contaminants strongly affects the photoyield such that emission from atomically clean samples may differ drastically from technical materials [43]. Spacecraft material properties vary dynamically with exposure to the space environment, even for science missions with strict contamination requirements [97].

1.2.4   Differential Charging

Secondary and backscatter currents depend strongly on the material properties of the surface, so different materials can charge to different potentials, even in the same environment. One consequence of this is that spacecraft can become differentially charged such that adjacent components on a spacecraft develop large potential differences. This leads to arcs and electrical discharges which can damage spacecraft electronics, degrade solar panel performance, and contaminate surfaces,

among other harmful effects. Spacecraft design standards recommend that all exterior surfaces on a spacecraft be electrically connected, such that the entire surface floats at the same potential [48, 92]. This recommendation is not always followed, however, and differential charging and arcing remain problematic [40]. Differentially-charged spacecraft present an interesting case for touchless sensing which is investigated in Chapter 6.

1.2.5 Self-Measurement of Charging

In electron-based touchless sensing, measuring the energy of electrons gives the potential difference between the target and sensing craft. To obtain an absolute value for the target potential, it is necessary to know the potential of the active, sensing craft. In GEO and other tenous plasma regimes, a satellite can measure its own potential in several different ways. The first method involves deploying antenna booms which are electrically isolated from the spacecraft and extend far enough away from the satellite bus such that they float at the plasma potential. By measuring the potential difference between the satellite frame and the boom tips, the spacecraft potential is determined. This method has been successfully used to measure the potential on several notable missions including SCATHA [87], the Van Allen Probes [98], and MMS [112], among others. The second method involves measuring charged particle spectra and observing the energy of distinct spectral features which shift depending on the spacecraft potential. For example, a low-energy ion with an energy of 3 eV would be measured at an energy of 103 eV by a spacecraft charged to -100 V. Thus, the apparent energy of the low-energy ion line can be used to determine the spacecraft charge. This method has been used to measure charging on the Van Allen Probes using data from a proton mass spectrometer [98]. Additionally, standardized charge monitor instruments which utilize this method have been proposed and designed [49]. Throughout this work, it is assumed that the sensing spacecraft has the ability to measure its own potential. Thus, by measuring the potential difference between the two objects, the absolute potential of the target is determined.

1.3   Literature Review

Several other methods have been proposed for remotely characterizing the electrostatic potential of an object in space. In Reference [42], numerous options for remote detection of spacecraft arcing are considered, such as observing surface glows, x-ray bremsstrahlung, or radio and optical emissions from arcs. Subsequent campaigns have successfully measured arc rates on GPS spacecraft using ground-based radio telescopes [40]. However, there remains a need to directly measure the voltage of a spacecraft, rather than only detecting the occurrence of arcs. It is unlikely that relevant signals can be detected from the ground, so other efforts focus on sensing potential from a nearby co-orbiting spacecraft.

Reference [17] discusses how the charge on one satellite in a two-craft formation can be estimated from the relative motion dynamics, which are driven by the Coulomb force, using range and range rate measurements. However, this method only provides an estimate of the electrostatic potential with low spatial and temporal resolution which are insufficient for most future applications. In Reference [36], a method is proposed for sensing charge by directly measuring the electric field around an object. This paper focuses on how to use the electric field measurements to obtain a charge estimate and then develop an electrostatic model of the target, but does not consider the significant challenges of obtaining a direct electric field measurement near a charged object in plasma.

One promising technique being developed in the AVS Laboratory at the University of Colorado Boulder uses bremsstrahlung x-rays emitted from the target and detected by a nearby sensing spacecraft [118]. Laboratory experiments have shown that this method is effective at touchlessly sense the potential on a target [117]. Further, this method allows for target material characterization by analyzing characteristic x-rays embedded in the bremsstrahlung signal.

The electron method for remote potential sensing has been successfully used to determine the charge distribution on the surface of planetary bodies. Data from the Electron Reflectometer on the Lunar Prospector mission shows evidence of electron beams flowing upward from the lunar
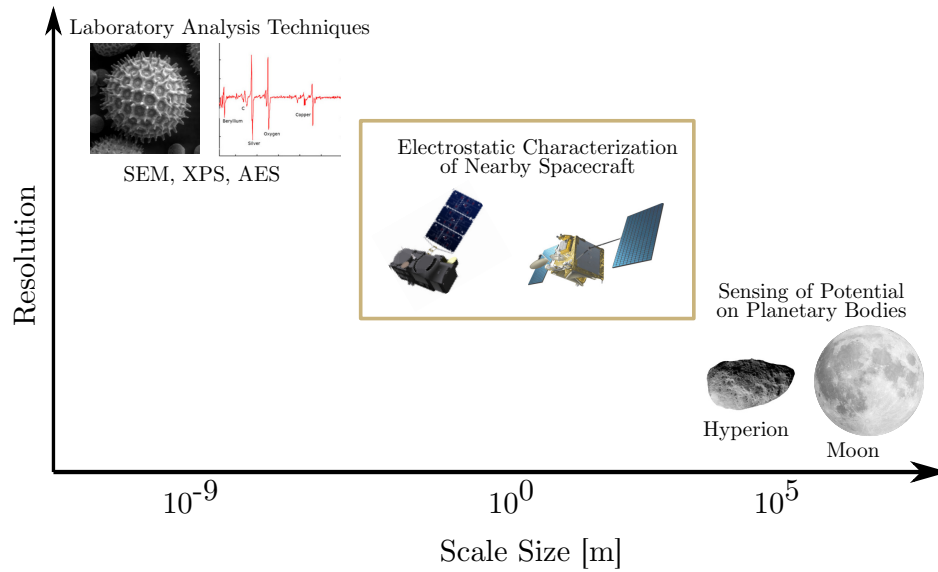
Figure 1.10: Comparison of remote sensing of spacecraft potential to other applications which use electrons to analyze a surface.

surface [59, 58]. The energy of the electron population indicate lunar surface potentials ranging from a few V to -4 kV, depending on the Moon's location within or outside of the magnetosphere and exposure to sunlight [55, 56]. By estimating the currents to a given location on the lunar surface, the Lunar Prospector data also enables estimation of the secondary emission properties of lunar regolith [57]. Similarly, electron population data from the electron spectrometer on the Cassini spacecraft shows evidence of strong surface charging on Saturn's moon Hyperion [88]. The measured surface potentials of -200 V closely match predicted values from surface charging models.

Secondary electrons and photoelectrons are also commonly used in laboratory techniques to analyze surfaces at the nanoscale. Techniques such as scanning electron microscopy (SEM), X-ray photoelectron spectroscopy (XPS), and Auger electron spectroscopy (AES) use information carried by backscattered, secondary, and photo- electrons emitted from a surface to characterize a sample with remarkable resolution. Figure 1.10 shows the electron method for remote sensing of spacecraft potential in context with existing applications which use electrons for touchless characterization. Laboratory sample analysis techniques are very common, but are applied on the nanoscale in highly controlled environments and with separation distances between sample and detector of a

few centimeters. On the opposite end of the graph, spacecraft have estimated the potential and material properties of planetary bodies using electrons, though there are very few examples of this in the literature. In this case, target scale sizes are on the order of tens of thousands of meters with separations between target and detector of tens of kilometers. The research presented herein extends these techniques to characterize spacecraft on the scale size of meters with separation distances between target and detector of tens of meters.

1.4   Research Overview & Challenges

The goal of this research is to investigate the use of secondary electrons and photoelectrons for sensing the elecrostatic potential of an object from a nearby spacecraft. Several key challenges are identified. First, it is apparent that the sensing process depends on an extensive parameter space. Two spacecraft are involved, both of whose physical sizes, shapes, attitudes, and voltages impact the sensing process. The separation distance between the two spacecraft, the space weather environment, the material properties on the target object, and the design of the electron detector on the sensing craft all also impact the potential sensing. Further, the possible voltages on the target object range from a few volts to tens of kilovolts, over five orders of magnitude, depending on the location, application, and local space weather. The sizable number of variables makes it challenging to obtain analytical insight about the problem. Next, a suitable vacuum chamber facility, including a variety of electron sources and an electron energy analyzer, must be developed to allow for experimental study of touchless potential sensing. The development, testing, and use of this facility represents a substantial expenditure of time, energy, and capital. Finally, the research requires a simulation framework be developed to accurately simulate trajectories of electrons near the surface of charged spacecraft with sufficient speed to allow for thorough consideration of the broad parameter space. To achieve the research objective, the research is separated into five goals:

(1) Determine the broad prospects, feasibility, and challenges of electron-based touchless potential sensing.

(2) Develop a space simulation facility suitable for conducting touchless potential sensing experiments.

(3) Investigate active sensing of a target using secondary electrons stimulated by an electron beam emitted from the sensing craft.

(4) Investigate passive sensing of the target using photoelectrons or secondary electrons emitted through interactions with the natural space environment.

(5) Consider complex sensing scenarios, in which the target object has spacecraft representative geometries or is differentially charged.

The successful accomplishment of these goals and the overall research objective represents a significant contribution to the fields of spacecraft charging and charged astrodynamics. The outcomes of this work will be critical for future space missions which involve multiple objects operating in close proximity in harsh charging environments.

Chapter 2

Feasibility and Challenges

2.1   Introduction

The first research objective is to develop understanding about the touchless sensing concept and to demonstrate that it is feasible given realistic operating conditions. One primary question is: how many electrons emitted from the target object can be measured by the sensing craft? To address this topic, numerical simulations are developed to model the trajectories of electrons in the vicinity of two charged spacecraft. The simulation development and implementation are described in the following section. The simulations are then used to model how the captured secondary or photoelectron current depends on the spacecraft sizes, potentials, and separation distances. Two specific case studies are presented to demonstrate that touchless sensing is feasible for realistic operating conditions including both active and passive modes. Finally, the factors which affect the maximum distance at which sensing is possible are discussed, along with important factors for designing or selecting an electron energy analyzer. The understanding developed in this chapter provides a solid foundation upon which the rest of this dissertation builds.

2.2   Simulation Framework

To estimate the signal emitted by the target object which is captured by the sensing craft, the trajectories of electrons around charged spacecraft are simulated using MATLAB. For the purposes required here, it is sufficient to model each spacecraft as a single sphere so that the electric field is computed straightforwardly. The simulation is also limited to a 2-D planar case, but in Chapter 6,

the simulation framework is extended to 3-D cases with arbitrarily shaped spacecraft.

First, voltages are assigned to the sensing craft and target object, and then the charges are computed using the capacitance matrix [102, 104]:

$$\begin{bmatrix} q_S \\ q_T \end{bmatrix} = [C(\rho)] \begin{bmatrix} V_S \\ V_T \end{bmatrix} \tag{2.1}$$

$$[C(\rho)] = \frac{\rho}{k_c(\rho^2 - R_S R_T)} \begin{bmatrix} R_S \rho & -R_S R_T \\ -R_S R_T & R_T \rho \end{bmatrix}, \tag{2.2}$$

where $[C(\rho)]$ is the 2×2 capacitance matrix, V_S and V_T are the sensing craft and target object voltages respectively, q_S and q_T are the charges, R_S and R_T are the object radii, ρ is the center-to-center separation distance, and k_c is the Coulomb constant. This formulation includes mutual capacitance effects between the two spacecraft. Next, the total electric field at a given point is found by the following equation:

$$\boldsymbol{E} = k_c \frac{q_S \boldsymbol{r}_S}{r_s^3} + k_c \frac{q_T \boldsymbol{r}_T}{r_T^3}, \tag{2.3}$$

where $\boldsymbol{r}_S$ and $\boldsymbol{r}_T$ are the distances from the given point to the center of the sensing craft and target object, respectively. The force on each electron each timestep is given by the Lorentz force:

$$\mathbf{F} = q(\mathbf{E} + \mathbf{v} \times \mathbf{B}), \tag{2.4}$$

where q is the electron charge, $\mathbf{v}$ is the velocity of each particle relative to the magnetic field which co-rotates with earth, and $\boldsymbol{B}$ is the magnetic field. For the present simulations, a magnetic field strength of 100 nT directed out of the simulation plane was selected to represent the field at GEO. Mutual repulsion between electrons is neglected. Similarly, there are assumed to be no interactions with plasma in the surrounding environment. The spacecraft are assumed to be perfectly geostationary so the velocity of the electrons with respect to the spacecraft is also the velocity with respect to the B field.

Secondary electrons have an initial kinetic energy distribution that can be modeled by the

the Chung-Everhart distribution [26]:

$$f(E) = \frac{(E - E_F - \phi)}{(E_F - E)^4}, \tag{2.5}$$

where $f(E)$ is the relative number of electrons generated, E is the secondary electron energy in eV, E_F is the Fermi energy of the surface material in eV, and ϕ is the work function of the material in eV. Further, it is known that secondary electrons are emitted with an angular distribution given by a cosine law. Therefore, the following distribution is used to give the initial 2-D angle-energy distribution of the electrons [29]:

$$f(E, \theta) = \frac{(E - E_F - \phi)}{(E_F - E)^4} \cos \theta, \tag{2.6}$$

where θ is the initial angle defined relative to the surface normal. This distribution is sampled to generate initial velocities for the simulated electrons.

Given the electric field, Lorentz force, and initial conditions, the electron motions are integrated using the Boris algorithm, which is widely considered the best method for simulating the motion of charged particles in electric and magnetic fields [18, 93]. Runge-Kutta integrators, which are commonly used in other dynamics simulations, do not conserve constants of motion, such as gyromotion or energy, in charged particle simulations. The Boris algorithm is a leapfrog type method which conserves constants of motion for charged particles. This algorithm is implemented as follows:

$$\mathbf{h} = \frac{q\mathbf{B}\,\mathrm{d}t}{2m} \tag{2.7}$$

$$\mathbf{s} = \frac{2\mathbf{h}}{1 + \mathbf{h} \cdot \mathbf{h}} \tag{2.8}$$

$$\mathbf{v}^- = \mathbf{v}_j + \left(\frac{q}{2m}\right)\mathbf{E}\,\mathrm{d}t \tag{2.9}$$

$$\mathbf{v}' = \mathbf{v}^- + \mathbf{v}^- \times \mathbf{h} \tag{2.10}$$

$$\mathbf{v}^+ = \mathbf{v}^- + \mathbf{v}' \times \mathbf{s} \tag{2.11}$$

$$\mathbf{v}_{j+1} = \mathbf{v}^+ + \left(\frac{q}{2m}\right)\mathbf{E}\,\mathrm{d}t \tag{2.12}$$

$$\mathbf{x}_{j+1} = \mathbf{x}_j + \mathbf{v}_{j+1}\,\mathrm{d}t, \tag{2.13}$$
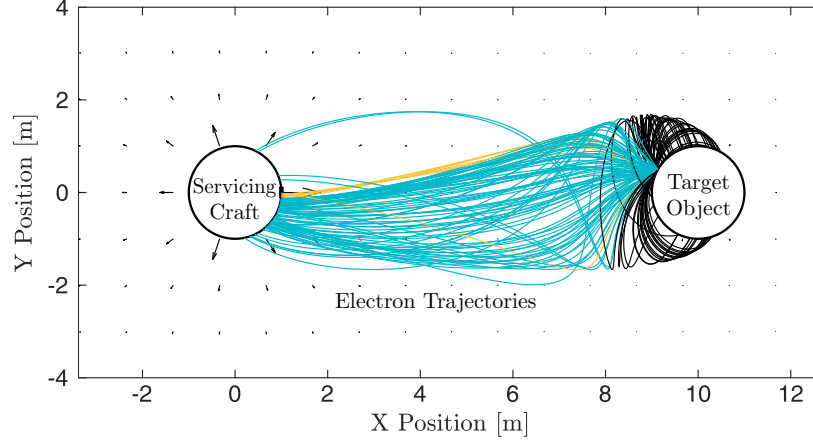
Figure 2.1: Electron trajectories for a low charging levels where $V_T = +20$ V and $V_S = +100$ V. Black lines indicate particles which do not escape the potential well of the target, blue lines indicate particles which hit the servicing craft, and yellow lines are for particles which enter a detector on the servicer.

where $\mathbf{x}_j$ and $\mathbf{v}_j$ are the position and velocity vectors at a given timestep j, and $\mathbf{h}$, $\mathbf{s}$, $\mathbf{v}'$, $\mathbf{v}^+$, and $\mathbf{v}^-$ are intermediate calculations.

Figure 2.1 shows example electron trajectories for a case where a 1 m radius target object is charged to +20 V, a 1 m radius servicing craft is charged to +100 V, and the two objects are separated by 10 m. The particles are generated 0.5 m above the x-axis on the target object. The target is slightly positive, so some of the secondary electrons, denoted by the black trajectories, do not have enough energy to escape the potential well and thus return to the target. Other electrons escape the target object and impact the servicing craft (blue trajectories), and a small number (in this case, 6 out of the 150 simulated particles) enter a 25 cm^2 sensor on the front of the servicing craft (yellow trajectories). The magnetic field has a small effect in this case. This simulation demonstrates that even if the target object is charged positively, the servicing craft can measure the energy of the electron population, as long as it is more positive than the target.

Figure 2.2 shows results for a case with high magnitude charging. In this case, the servicing craft is charged to +20 kV, the target object is charged to -20 kV, and electrons are generated on the target between 0 and 20 cm above the x-axis. Here, the black lines indicate electrons which miss the servicing craft entirely and fly off into space. As these particles have much higher energy
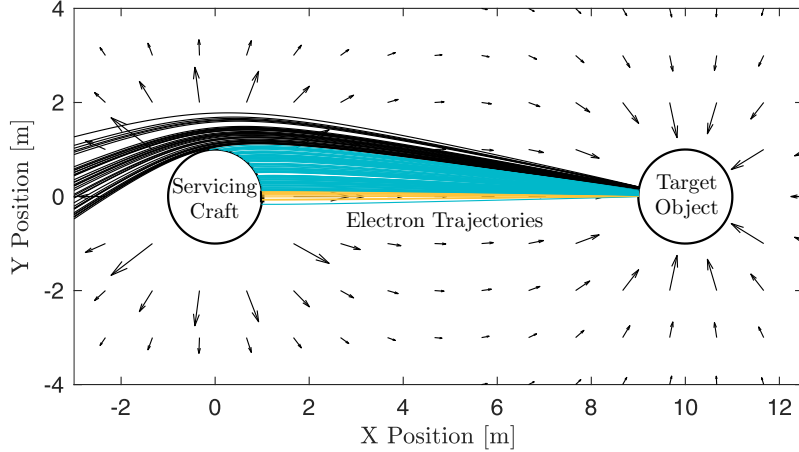
Figure 2.2: Electron trajectories for a high charging levels where $V_T = $ -20 kV and $V_S = $ +20 kV. Black lines indicate particles which escape to space, blue lines indicate particles which impact the servicing craft, and yellow lines are for particles which enter a detector on the servicer.

compared to the previous example, the effect of the magnetic field is negligible in this case.

2.3   Parameter Trade Studies

An important quantity for investigating the prospects and challenges of the electron touchless sensing method is the fraction, defined as α, of the emitted secondary electron (or photoelectron) current, I_{SEE}, which is captured by the detector on the servicing craft, I_{SEC}:

$$\alpha = \frac{I_{\mathrm{SEC}}}{I_{\mathrm{SEE}}}. \tag{2.14}$$

This fraction is a function of the object potentials, the separation distance, the relative attitudes, and the geometry of the two satellites. A broad range of simulations are run to investigate this parameter space and obtain insight into the operating conditions of the electron sensing concept.

Figure 2.3 shows the fraction α plotted as a function of the servicing craft voltage, V_S, and the separation distance, L. In this simulation, the target object voltage, V_T, is held fixed at -100 V. Both spacecraft are assumed to be spheres of radius 1 m, the detector on the servicing craft is defined to be 25 cm^2, and the secondaries are generated along a 40 cm^2 area on the target object surface centered about the line of separation. The results show that the captured current depends most significantly on the separation distance. For separation distances of a few craft radii, the
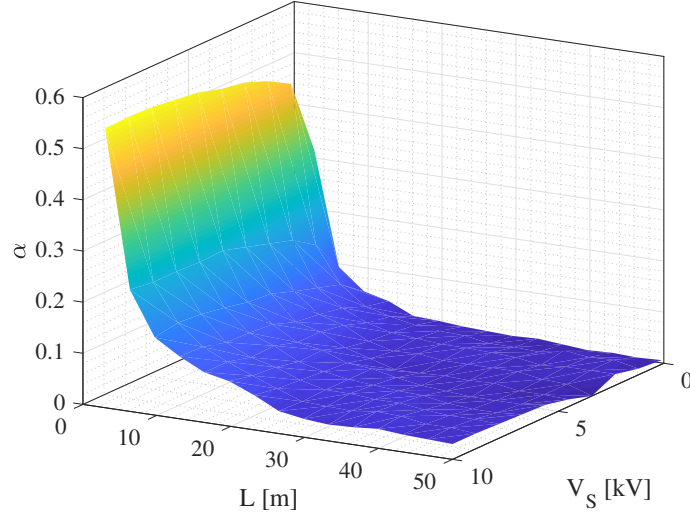
Figure 2.3: Fraction of electrons captured, α, as a function of separation distance and servicing craft voltage.

captured current is tens of percent of the emitted current. Beyond 10 m separation, the captured current decreases from tens of percent to a few percent of the emitted current. For forced charging applications where I_{SEE} is large, the remote potential sensing method would be feasible at operating distances of 10s of meters, as is shown explicitly in the next section. For other applications where I_{SEE} is small, it may be necessary to operate at separations of a few craft radii to obtain a sufficient signal to noise ratio. Sections 2.4.1 and 2.4.2 provide case studies for specific operating conditions within each regime.

Figure 2.4 shows how α depends on the voltage of both the servicing and target craft. The separation distance is fixed at 12 m and the same assumptions regarding the initial condition of the secondaries and the detector size are made again here. The highest value of α occurs when V_T is at the lowest magnitude potential and V_S is at the highest. This occurs because the electrons are not strongly accelerated away from the target at which they are generated, but are strongly accelerated toward the servicing craft. Therefore, the servicing craft collects a large fraction of the secondaries. Conversely, when V_T is large negative and V_S is small positive, α is very small. In this case, the electrons gain most of their energy when leaving the target surface and their trajectories
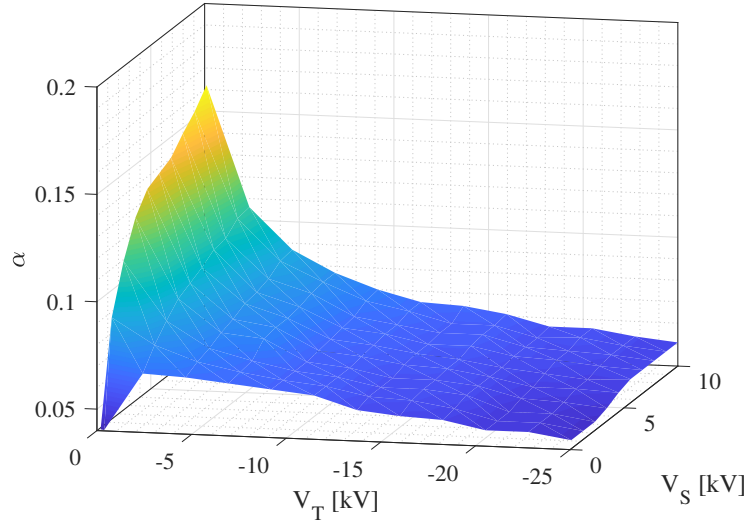
Figure 2.4: Fraction of electrons captured, α, as a function of the target object and servicing craft voltages.

are essentially determined before they are influenced by the servicing craft electric field. Therefore, only those electrons which are accelerated along the line between the two craft will be captured by the detector. Interestingly, α is lowest where both V_T and V_S are small in magnitude. In this case, the electrons are not accelerated strongly and therefore travel slowly away from the target surface. Therefore, the initial velocities of the electrons are important and the initial cosine angular distribution has time to expand such that only a small percentage of the electrons map onto the detector.

2.4   Case Studies

2.4.1   Electrostatic Tractor Case Study

To demonstrate feasibility of remote potential sensing application to the electrostatic tractor (ET), a case study is conducted. Reference [64] provides an example operating condition for the ET: a servicing craft of 2 m radius is charged to $V_S = 21.4$ kV and a target object of radius 0.935 m is charged to $V_T = $ -14.6 kV. The two spacecraft are separated by a distance of 12.5 m. The electron beam energy is $E_{\text{beam}} = 40$ keV and the beam current is $I_{\text{beam}} = 520$ μA. Further, it is

assumed that the beam diameter is 20 cm and the beam impacts the target sphere centered on the line of separation. The secondary electron emission current model is given by:

$$I_{\text{SEE}} = -4\delta_M I_{\text{beam}}\kappa, \tag{2.15}$$

where

$$\kappa = \frac{E_{\text{eff}}/E_{\text{max}}}{(1 + E_{\text{eff}}/E_{\text{max}})^2}, \tag{2.16}$$

and

$$E_{\text{eff}} = E_{\text{beam}} - qV_S + qV_T. \tag{2.17}$$

δ_M is the peak of the secondary electron yield curve and E_{max} is the energy at which this peak occurs [34]. Typical secondary emission values for aluminum of $\delta_M = 1$ and $E_{\text{max}} = 300$ eV are assumed [75], so $I_{\text{SEE}} = 163$ µA.

The secondary electron current captured by the detector on the servicing craft, I_{SEC}, is found by:

$$I_{\text{SEC}} = \alpha I_{\text{SEE}}, \tag{2.18}$$

where α is between 0 and 1. The trajectories of 5000 particles are simulated. For these conditions, the numerical simulation results show that 14.1% of the secondary electrons are captured by the 25 cm^2 detector centered on the tractor satellite. Therefore, $\alpha = 0.141$ and $I_{\text{SEC}} = 23.0$ µA. Note that the number of electrons simulated is varied to ensure that α converges as the number of particles increases. 5000 particles is determined to be a sufficient number of particles, and $\alpha = 0.141$ remains constant even for larger numbers of particles.

The flux of secondary electrons occurs at a very narrow range of energies corresponding to the potential difference between the two craft plus the initial energy distribution of the electrons. The captured secondary current is converted to a flux so that it can be compared to the ambient electron flux. The captured secondary flux, F_{SEC}, is modeled as a population distributed according to the Chung-Everhart model [26]. It is assumed the debris object is aluminum, so values of 11.7 eV and 4.08 eV are taken for the Fermi energy and work function, respectively. A bi-Maxwellian
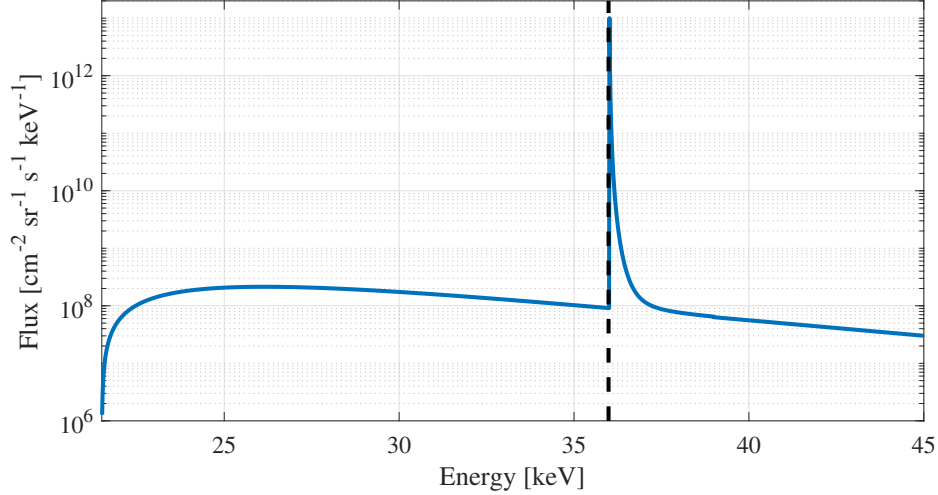
Figure 2.5: Electron fluxes for the electrostatic tractor remote potential sensing case study. The peak at 36 keV is the electron population from the target, which has been superimposed on a representative plasma background.

plasma background is assumed:

$$F = \sum_{i=1}^{2} n_i \sqrt{\frac{q}{2\pi T_i m_e}} \frac{qV_S}{k_B T_i} \exp\left(\frac{qV_S}{k_B T_i}\right), \tag{2.19}$$

where k_B is the Boltzmann constant and m_e is the electron mass, and other parameters are selected to be representative of storm-time conditions in GEO: $n_1 = 0.3$ cm^3, $T_1 = 4$ keV, $n_2 = 0.2$ cm^3, and $T_2 = 7$ keV [30].

Figure 2.5 shows the electron flux at the sensing craft, including both the ambient plasma and the secondary electron population. The dashed black line shows the expected value of the secondary population energy, equal to the potential difference between the servicing craft and target object: $V_S - V_T = 36.0$ keV. Next, the response of a realistic energetic particle detector to the secondary electron population is modeled. Numerous electron energy analyzers have been utilized in laboratory and on-orbit missions. Electrostatic analyzer-type instruments use electric fields to filter between particles of different energies. These detectors can measure energies ranging from a few eV to tens of keV (30–50 keV typical) and have energy resolutions of $\Delta E/E = 7$–20%. To model the response of an instrument, it is assumed that the instrument can measure in the range of tens of keV with an energy resolution of $\Delta E/E = 8\%$ and a geometric factor of 6.6

$\times 10^{-3}$ cm^2 sr keV (equal to that measured for the MMS electrostatic analyzers during in-flight calibration [91]). Figure 2.6 shows the count rates which would be observed by an instrument with the given parameters. The dashed black line indicates the actual value of the electron energy peak (36.0 keV). The energy bin which ranges from 34.1 to 36.9 keV is several orders of magnitude higher than the background. This is because the detected secondary electron current is already large and the secondary electrons are limited to a very narrow energy range. Even for geometries in which the majority of the secondary electrons escape into space, the signal peak from a small percentage of captured electrons provides sufficient information for the potential of the target object to be determined. Subtracting the potential of the servicing craft from the bin edges of the electron peak gives a range of values for the target potential between 12.7 and 15.5 keV or an accuracy of 5%–13%. Using an instrument with finer energy resolution would reduce these values. In light of these results, the proposed method for remote potential sensing is feasible with currently existing detector capabilities and for operating conditions relevant to forced charging applications such as the ET.
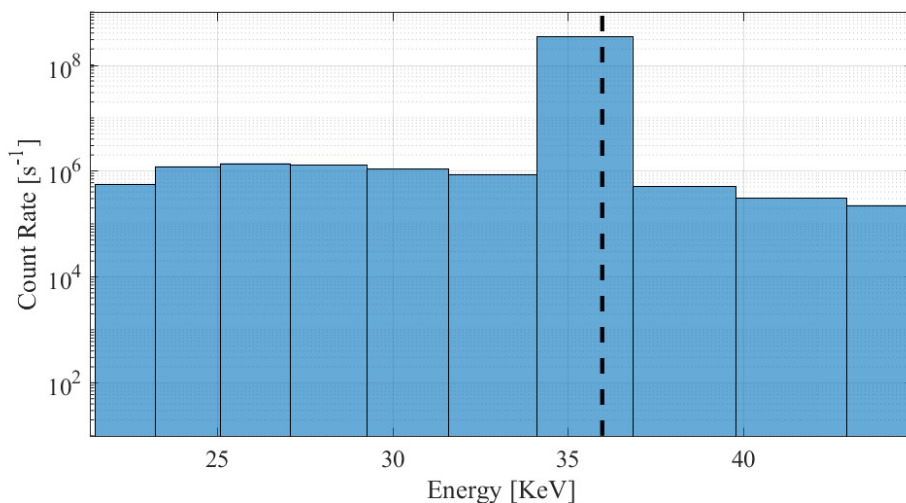
Figure 2.6: Binned electron fluxes for the electrostatic tractor remote potential sensing case study.
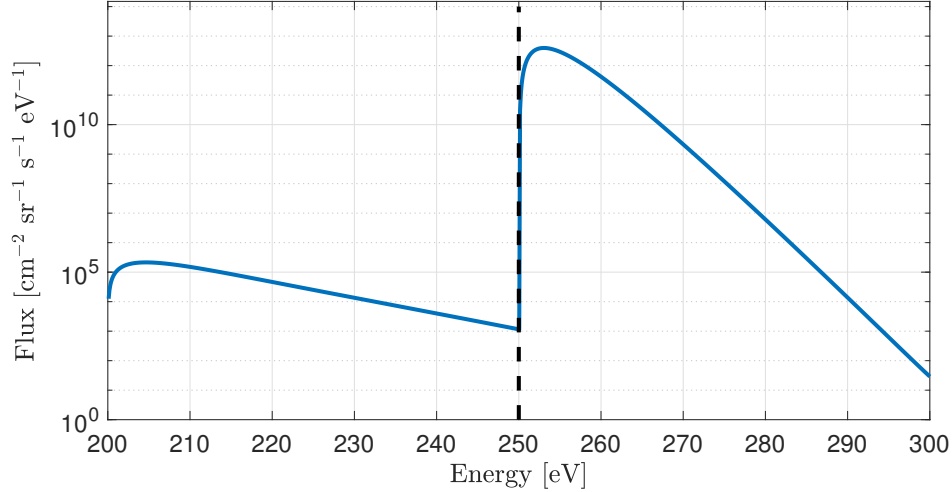
Figure 2.7: Electron fluxes for the natural charging remote potential sensing case study. The distribution at 250 eV is the electron population from the target object, which has been superimposed on a representative plasma background.

2.4.2   Passive Sensing Case Study

Another case study is presented to determine the feasibility of passive sensing of potential using photoelectrons. An operating condition is assumed in which the sensing craft and target object are spheres of 1 m radius, separated by 8 m, with $V_S = 200$ V and $V_T = $ -50 V. The target is assumed to be a conducting, aluminum sphere with $j_{ph} = 40$ µA m^2 and $k_B T_{ph} = 2$ eV. The electrons are again given an initial cosine angular distribution. It is assumed that the half of the target sphere facing the servicing craft is in sunlight. Under these conditions, only 2.8% of the emitted photoelectrons are captured by the sensor on the servicing craft. This percentage is small because photoelectrons are generated on a large area of the target craft, but only a small area maps back to the sensor. Assuming the sunlit area is a circle, the emitted photoelectron current is 126 µA. Given $\alpha = 0.028$, the current captured by the servicing craft sensor is 3.5 µA. The photoelectron population is modeled as a Maxwellian distribution with a temperature of 2 eV [51]. The same bi-Maxwellian distribution used in the previous section is used again here for the ambient plasma. Figure 2.7 shows the photoelectron population flux superimposed on the bi-Maxwellian background. The dashed black line indicates the potential difference between the two

spacecraft. The peak photoelectron flux is several orders of magnitude larger than the background flux, therefore the signal is easily detectable given current energy analyzer capabilities. In light of this result, touchless potential sensing is feasible for passive sensing of small potentials using photoelectrons.

2.5 Maximum Sensing Distance

There are numerous applications for which it would be highly beneficial to sense potential over distances of tens of meters. However, it is worthwhile to consider the factors which limit the maximum distance for which touchless potential sensing is feasible. Possible limiting factors include collisions with particles in the ambient plasma, electron gyrorotation and drift motion due to the electric and magnetic fields, and decrease in the measured signal as a function of increasing distance.

The average distance a particle travels in a plasma before colliding with another particle is called the mean free path, which is given by:

$$\lambda_{\mathrm{mfp}} \approx 64\pi \lambda_D \frac{\Lambda}{\ln \Lambda}, \tag{2.20}$$

where λ_D is the Debye length and Λ is the plasma parameter [8]. The $\ln \Lambda$ term is a correction factor which accounts for the fact that most collisions only cause small deflections. Collisions between particles may result in energy loss from the electron whose energy is related to the potential difference between the target and sensing craft. Thus, in a collisional plasma, information about the target potential would not be communicated to the sensing craft via the electrons. However, assuming conservative values for plasma density in GEO of 1 cm^{-3} and temperature of 4 keV, the mean free path at GEO is on the order of 10^{12} km. Clearly, energy loss due to scattering interactions with plasma particles is not a limiting factor.

Another possible limiting factor to consider is the gyromotion of a charged particle in a magnetic field. The gyroradius is given by:

$$r_g = \frac{mv_\perp}{|q|B}, \tag{2.21}$$

where r_g is the gyroradius, m is the particle mass, $v_\perp$ is the velocity of the particle in the direction perpendicular to the field, and B is the magnetic field magnitude. Figure 2.8 shows the gyroradius of an electron assuming a magnetic field strength of 100 nT (representative of the typical field strength at GEO). The gyroradius of a 0.5 keV electron is approximately 750 m whereas that for a 1 keV electron is over 1 km (assuming the particles are moving perpendicular to the field). If a sensing craft is to measure electrons emitted from the target directly, it should be within a gyroradius of the target (though of course, the gyroradius depends on the energy of the particle, which is not known until a first measurement is made).
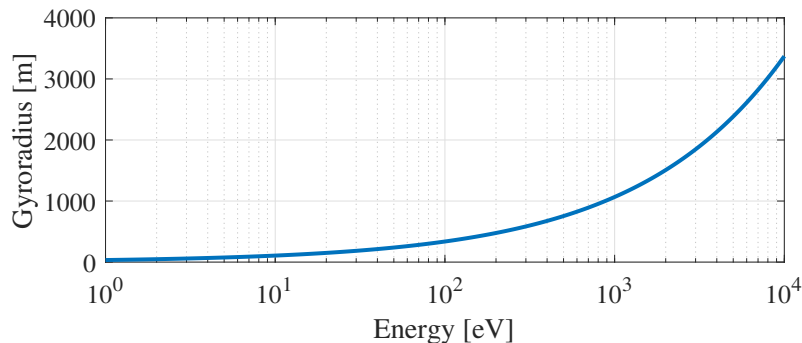
Figure 2.8: Electron gyroradius in a 100 nT magnetic field.

At distances beyond a gyroradius, the orientation of the magnetic field with respect to the sensing and target spacecraft must be considered. Figure 2.9 shows a 2D simulation of sensing from a large separation distance with a favorable magnetic field alignment. A 5 m radius target craft is located at the origin and charged to -100 V. A 5 m radius sensing craft is located at X = 1000 m. The magnetic field has a magnitude of 100 nT and points along the vector from the target to the sensing craft. In this case, the electrons initially spread out from the target, but then are guided by the magnetic field toward the sensor. Obviously the gyrorotation about the magnetic field induces some out-of-plane motion, but the electron population indeed travels toward the sensor, so it is reasonable to expect the sensor could detect the population and subsequently determine the target potential. Aiming and focusing an electron beam to hit a target at such distances would be extremely difficult, so the electron population would likely be naturally generated at such distances.
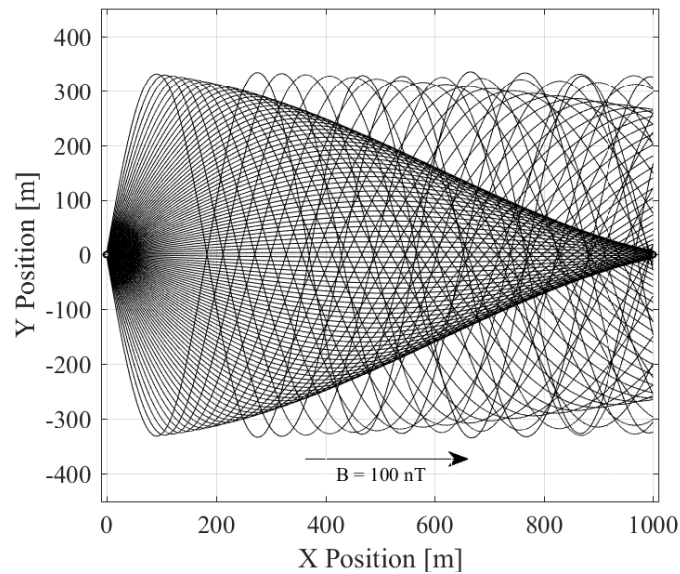
Figure 2.9: Trajectories of electrons emitted from the -100 V target when the +100 V servicer is separated along a magnetic field line.

However, no signal is measurable if the sensor is more than a gyroradius away and if the magnetic field points in a direction that is orthogonal to the target-sensor alignment. Figure 2.10 shows results for the same setup as in the previous example, except with the 100 nT field pointing in the Y direction. In this case, the electrons are bound by the field line and do not make it to the sensing craft on the right side of the figure. Therefore, sensing at distances beyond a gyroradius is possible with favorable alignment with respect to the magnetic field.

Assuming sensing from within a gyroradius, the most significant limiting factor is the spreading out of the electron signal which results in a smaller signal measured by the sensing craft. As shown in Figure 2.3, the ratio of electrons emitted by the target to electrons captured by the sensing craft falls off quickly as a function of separation distance. This means that the maximum distance at which a signal can be measured depends on the secondary or photoelectron current produced, the voltages on each craft, the geometry of the target, and the capabilities of the sensor. Figures 2.3 and 2.4 show how the expected signal varies as a function of the craft voltages and
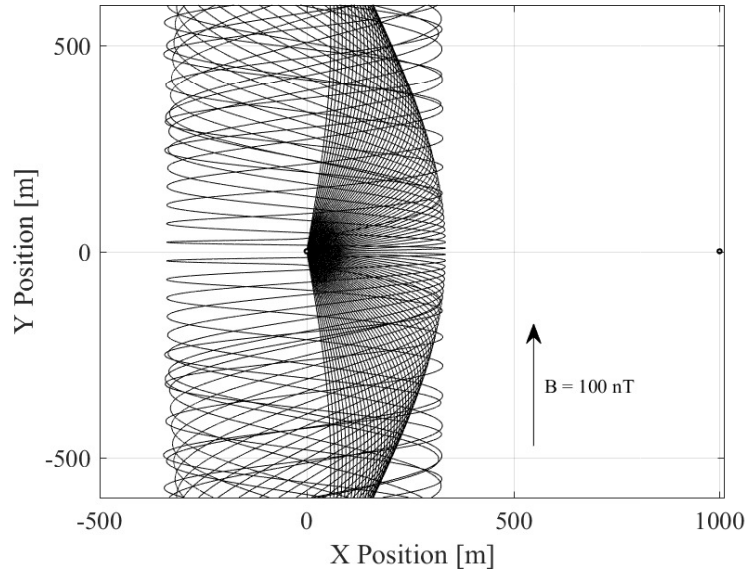
Figure 2.10: Trajectories of electrons emitted from the -100 V target when the +100 V servicer is separated orthogonal to the magnetic field.

separation distance. Chapter 6 discusses how target geometry affects the sensing physics. Given realistic sensor capabilities and expected signal magnitudes, a maximum separation distance on the order of dozens of meters is reasonable. If the spacecraft are separated along a magnetic field line, sensing at farther distances is possible. If necessary for specific mission requirements, the sensing spacecraft could move into relative orbit such that it crosses the field line which connects it to the target.

2.6   Instrument Design Considerations

The electron method for touchless potential sensing requires the use of an instrument to measure the energy of an electron population and infer the potential difference between the target and servicer. Instrument requirements can be derived from the mission requirements for touchless sensing, as is discussed below.

One key figure of merit for an electron energy analyzer is the energy range. The instrument must be able to measure electron energy distributions at energies corresponding to the potential

difference between the target and sensing craft. For the electrostatic tractor case study, the expected potential difference is 36 kV. Spacecraft have been measured to charge naturally to 10-20 kV negative for severe space weather conditions in GEO [54, 76]. Therefore, an instrument to measure such charge levels must be able to measure electron energy distributions in the range of tens of kV. Top-hat electrostatic analyzers have flown on numerous space missions with energy ranges from 10 eV to around 30 keV [91, 81, 115]. The HOPE instrument on the Van Allen Probes has an impressive energy range of 1 eV to 50 keV [46]. Other electrostatic analyzer designs offer measurement of energies up to 200 keV [69]. Therefore, the capability to measure electron distributions in the range needed for touchless sensing already exists.

The next critical factor in designing an instrument for touchless sensing is energy resolution. Electrostatic analyzers which have flown on space physics have energy resolutions in the range of $\Delta E/E = $ 7-15% [115, 46]. For the electrostatic tractor application, an energy resolution of $\Delta E/E = 7\%$ at an energy of 36 kV would give an energy bin width of 2.5 kV. Though this is a large uncertainty in voltage, it is still useful for applying feedback for Coulomb force and torque control. Most space physics missions require high time cadences at the expense of energy resolutions. The MMS mission for example, takes a full 3D electron distribution in 30 ms, but only requires an energy resolution of 20%. This is because the space physics processes MMS measures occur on very short time scales. In contrast, spacecraft charging variations and relative motion dynamics occur on time scales of minutes to hours. Therefore, an instrument designed specifically for touchless sensing would likely achieve improved energy resolution but at the cost of lower time resolution than instruments which have flown to date.

Other instrument figures of merit include the field-of-view and the sensitivity. Unlike space physics missions which measure particles coming from all directions, the electrons which carry information about the target potential are highly directional. The instrument field-of-view should be defined based on the size of the target object to be measured and the separation distance between target and sensor. The sensing craft must also be able to provide pointing control to ensure electrons emitted from the target are able to enter the detector. Finally, the instrument

should be sensitive enough to measure currents at the expected magnitude. Again, this is highly mission dependent as the secondary current for the electrostatic tractor is quite large, whereas currents used for passive sensing are much smaller. The minimum measurable current should be defined based on the expected current emitted from the target and the separation distance.

2.7   Results & Summary of Research Goal 1

In this section, a simulation framework has been developed to model the trajectories of electrons around charged spacecraft. Simulations have been run to obtain insight into the sensing process and, most importantly, how the expected signal varies with the potentials on both the target and servicer as well as the separation distance. Case studies have been conducted to clearly establish that touchless potential sensing is feasible. Using either secondaries from an active electron beam or the photoelectron current, the potential on an object can be sensed over distances of tens of meters in GEO with realistic instrumentation. Additionally, the factors which affect the maximum separation distance for which sensing is possible have been discussed, along with considerations for designing an appropriate instrument to measure the electron energy distributions. The next chapters build upon the understanding gained in this chapter to demonstrate and analyze touchless sensing through laboratory experiments and more complex simulations.

Chapter 3

Development of an Experimental Facility

3.1   Motivation for Experimental Study

Emission of secondary electrons and photoelectrons from surfaces has been studied for decades (e.g. [19]), and numerous studies report measurements of emission characteristics for specific materials (e.g. [29, 71]). However, several key differences exist between the literature and touchless spacecraft potential sensing which underscore the need for new experiments specific to touchless sensing. First, experiments to study and measure electron emission are generally conducted in the presence of zero or very small electric fields. In some cases, the detector or target is biased by a few volts. However, touchless sensing involves emission from surfaces charged to hundreds of volts or even tens of kilovolts. Further, most experiments in the literature use a flat plate target with a full hemispherical detector to measure electrons emitted into the full 2-π steradian hemisphere. In contrast, touchless potential sensing is conducted on spacecraft with complex geometries using detectors which only measure electron fluxes at a point. Similarly, most studies on secondary and photoemission involve separation distances of a few centimeters, whereas in space, sensing electrons from separation distances of tens of meters is to be expected. Most experimental studies on electron emission consider pure materials that have been atomically cleaned. However, significant differences in emission properties exist between pure materials and technical materials (i.e. those which are actually used to build spacecraft) due to the presence of oxide layers, surface contaminants, and differences in surface roughness [6, 32]. Depending on the materials, age, and cleanliness/contamination requirements of a given mission, actual material properties may deviate

from those provided in databases [31, 23, 41]. Clearly, there are significant differences between existing results in the literature on electron emission and the current work. Touchless potential sensing involves high magnitudes of charging, complex-shaped targets, large separation distances, and the presence of numerous technical materials. Therefore, it is prudent to investigate the effect of these factors through dedicated laboratory experiments in addition to numerical simulations.

In the present study, experiments are used wherever possible to demonstrate the feasibility of touchless sensing and to investigate the effects of various geometries, materials, and differential charging on the sensing. To this end, a space environment simulation chamber is developed and used for experimental study. Because the chamber is limited in size, computer simulations (discussed in detail in the following chapters) are also developed to investigate touchless sensing for spacecraft scales and separation distances which cannot be tested experimentally. Specific experiments are recreated in the simulations, allowing for direct comparison which serves to validate the simulations. Then, the simulations are used to model full-scale spacecraft and sensing scenarios.

3.2   Description of ECLIPS Chamber

The Electrostatic Charging Laboratory for Interactions between Plasma and Spacecraft (ECLIPS) is a bell-jar style vacuum chamber which is 56 cm in diameter. The chamber was donated by the Air Force Research Laboratory to the AVS Laboratory at the University of Colorado in 2016. Since then, the chamber has undergone a massive overhaul and has been developed into a dedicated facility for experimental spacecraft charging and charged astrodynamics research. Figure 3.1 shows a picture of the chamber. The full capabilities of the chamber are described below. Due to the bell-jar design, several sources are mounted to the chamber lid, which moves up and down, whereas most of the sensors and other experiment components are bolted to the floor inside the chamber. This creates challenges with experiment alignment and repeatability since there are several centimeters of sway in the lift mechanism. To rectify this problem, a two-column lift has been designed and installed which ensures that the lid returns to a repeatable location each time the chamber is opened and closed. Figure 3.2 shows the chamber with the new lift mechanisms.

3.2.1 Vacuum Environment

An Agilent IDP-15 scroll pump is used to bring the chamber from atmospheric pressure down to the required operating pressure for the turbomolecular pump, which is between 100 and 200 mTorr. The turbomolecular pump is capable of pumping the chamber pressure down to the upper µTorr range within a few hours and to the low µTorr range overnight (depending on the cleanliness of the experimental components). After several days of continuous pumping, a chamber base pressure in the upper 10^{-7} Torr has been achieved. An MKS Vacuum Sentry Valve isolates
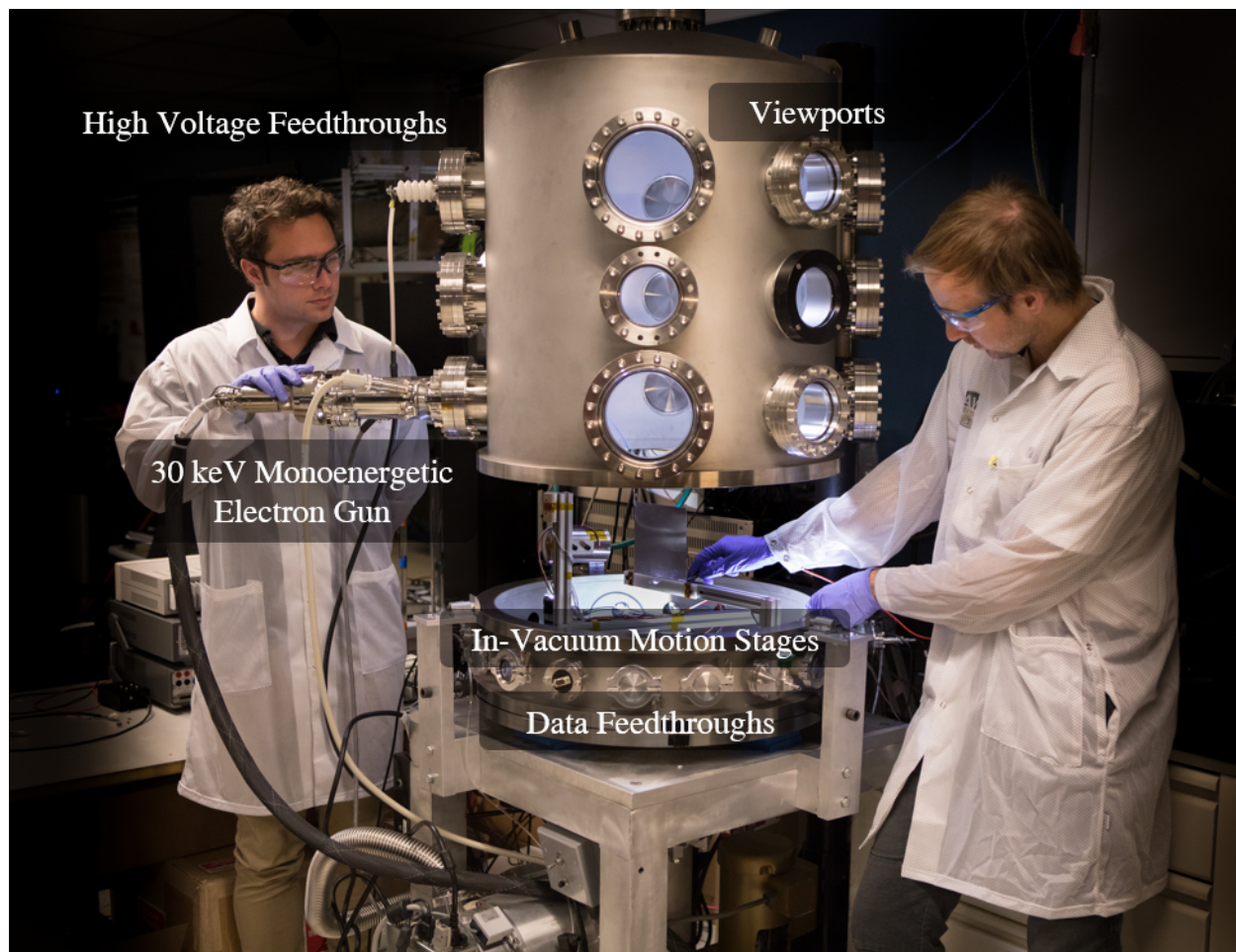
Figure 3.1: ECLIPS Space Environment Chamber.
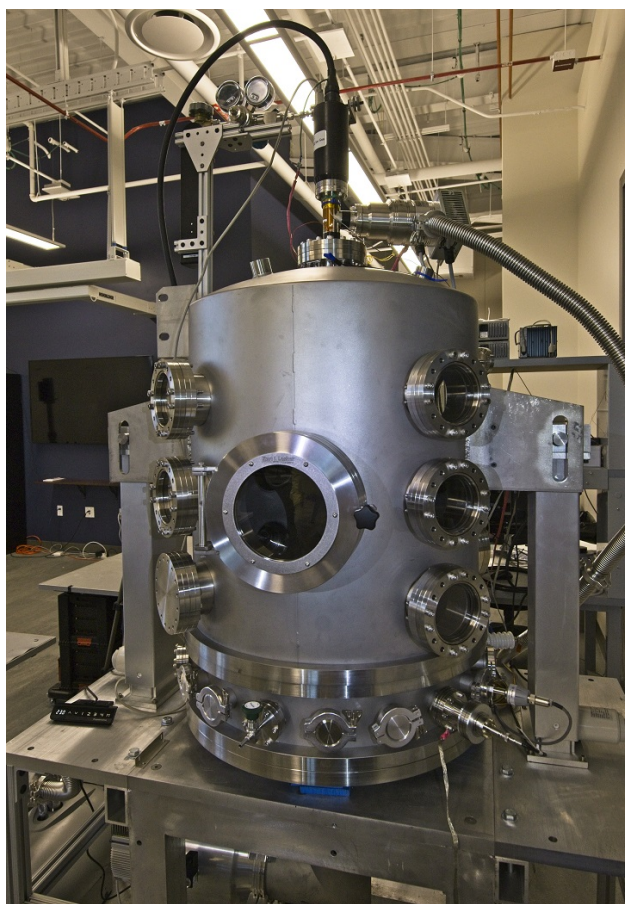
Figure 3.2: New lift mechanisms which improve the chamber stability and positioning repeatability.

the turbopump and chamber from the scroll pump in the event of a power outage, allowing the turbopump to spin down safely in vacuum.

An Agilent ConvecTorr gauge provides pressure measurements from atmosphere down to 1 mTorr. When the turbopump is powered on, an Agilent IMG-300 inverted magnetron gauge (IMG) is used to measure the pressure in the range of 10^{-3} to 10^{-11} Torr (or down to the chamber base pressure). The vacuum gauges interface with an Agilent XGS-600 gauge controller which then displays continuous pressure measurements from atmosphere to the base pressure.

3.2.2   In-Vacuum Motion Stages

Many experiments require the ability to move various components inside the vacuum chamber without breaking vacuum. To meet this need, a 2-D motion system has been designed, built, and installed to provide motion capability during experiments. To maximize the usable volume inside the chamber, a cylindrical motion system is used. A Newmark Systems RM-3 vacuum compatible rotary stage is used for rotational motion. A custom-built motion stage was designed and built in the AVS Lab to provide linear motion. Figure 3.3 shows a picture of the linear stage in the vacuum chamber. The stepper motor is at the bottom of the picture, connected to the drive rod which moves the carriage (to which a vertical post is mounted) back or forth. Depending on the needs of a given experiment, the linear stage can be mounted on top of the rotational stage to provide full positioning access along any plane in the chamber. Figure 3.4 shows the linear stage
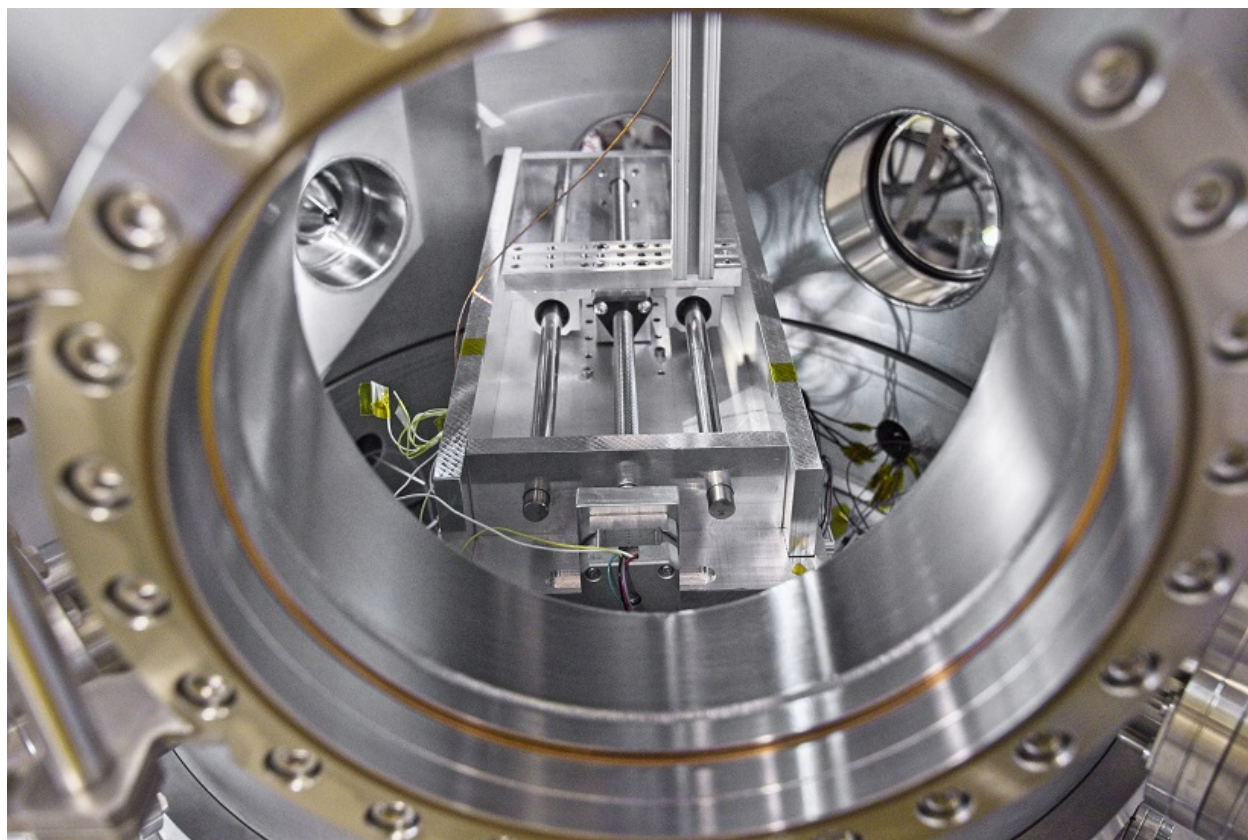
Figure 3.3: Linear motion stage mounted inside the chamber as viewed through the 10 inch port.
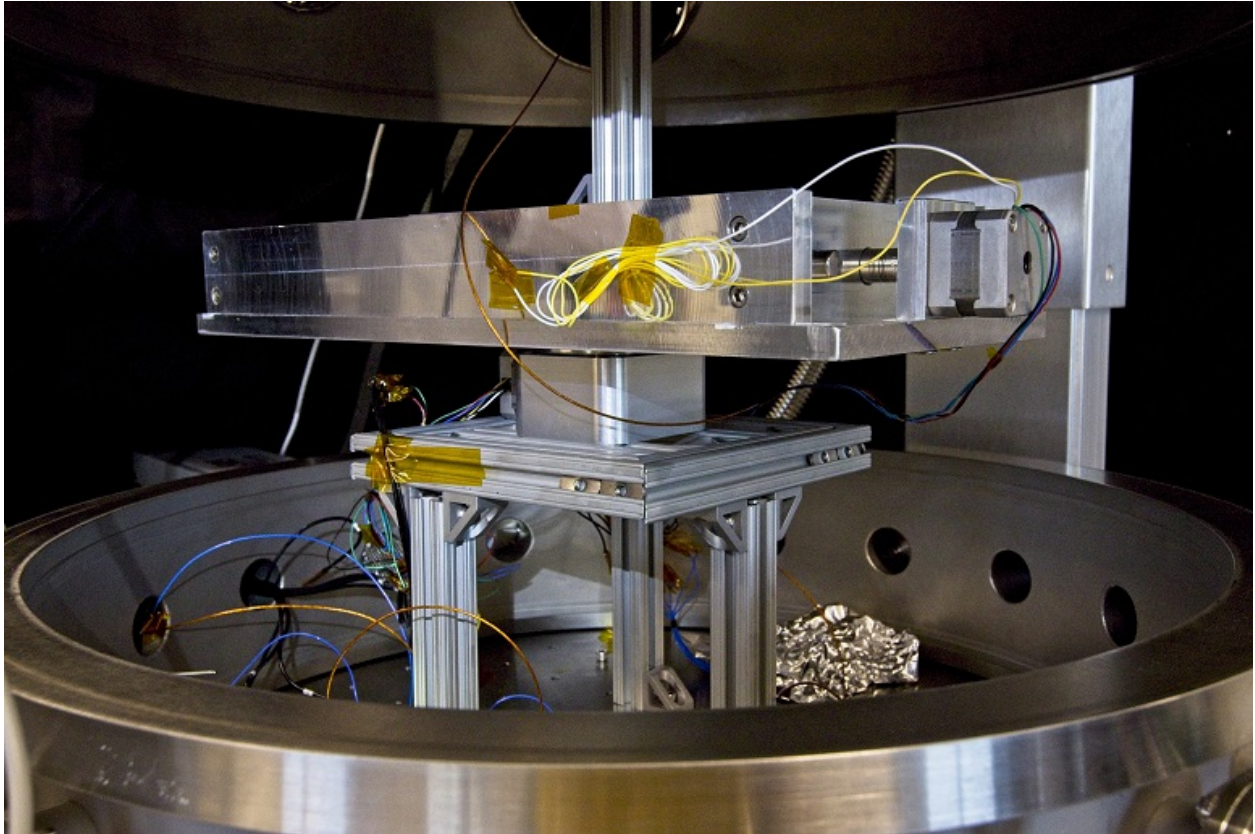
Figure 3.4: 2D motion system with the linear stage mounted on top of the rotational stage.

mounted on top of the rotational stage. For other experiments, the rotational and linear stages are used separately. Both systems contain only low-outgassing greases. A Keithley 2301A-30-3 power supply, controllable via LabVIEW, is used to provide power to the in-vacuum stepper motors. The driver system to command steps to the motors was built in-house using a SparkFun RedBoard system.

In its current form, the rotational stage provides accurate positioning to within $2°$. The linear stage provides accurate positioning on the order of a millimeter. The motion system is used to consider the effect of relative geometries between target and sensor on touchless sensing, but high-precision motion control is not required. Therefore, the positioning resolution of the motion system is sufficient for the present research. Limitations of the current design are that the stepper motors do not have encoders to check for missed steps, and there is no truth value for locating

the stages within the chamber. To address these limitations, future improvements should install encoders to check for missed steps, homing switches to provide an absolute position reference, and a laser distance measurement device to more accurately measure distances and angles between components in a given experimental setup. Further, it is known that the stepper motors produce large amounts of heat during operation, and sufficient heat dissipation paths do not exist while the system is under vacuum. The steppers are currently limited to a duty cycle of 50% to prevent overheating. Future improvements should also consider adding in-vacuum thermocouples for real-time monitoring of the stepper motor temperatures.

3.2.3   Sources

3.2.3.1   Monoenergetic Electron Gun

A Kimball Physics EMG-4212 monoenergetic electron gun provides a primary electron source for experiments. The electron gun is capable of emitting electrons in an energy range of 1 keV to 20 keV with currents between 10 nA and 100 µA. The electron beam can be focused to achieve a desired spot size, deflected to strike a given target, and rasterized to output a scan pattern. A phosphor screen can be installed in the chamber to characterize the size and shape of the electron beam. Figure 3.5 shows an example of the beam hitting the phosphor screen with an energy of 5 keV, a focus voltage of 500 V, an x-deflection of +60 V, and a y-deflection of -25 V. The beam size can be reduced to a spot on the order of millimeters by further increasing the focus voltage. Note that the blue polygon is the actual beam. The orange glow is light emitted from the electron gun's tantalum filament which is visible when the chamber is dark. The electron gun must be run in vacuum environments less than 10^{-5} torr.

3.2.3.2   Vacuum Ultraviolet Light

A Hamamatsu L10706 deuterium lamp provides an in-vacuum light source to stimulate photoemission from surfaces. The source emits from 115 nm to 400 nm with a primary peak at 160 nm or 7.75 eV and in a cone of 7.5°. For comparison, the dominant ultraviolet line in the near-Earth
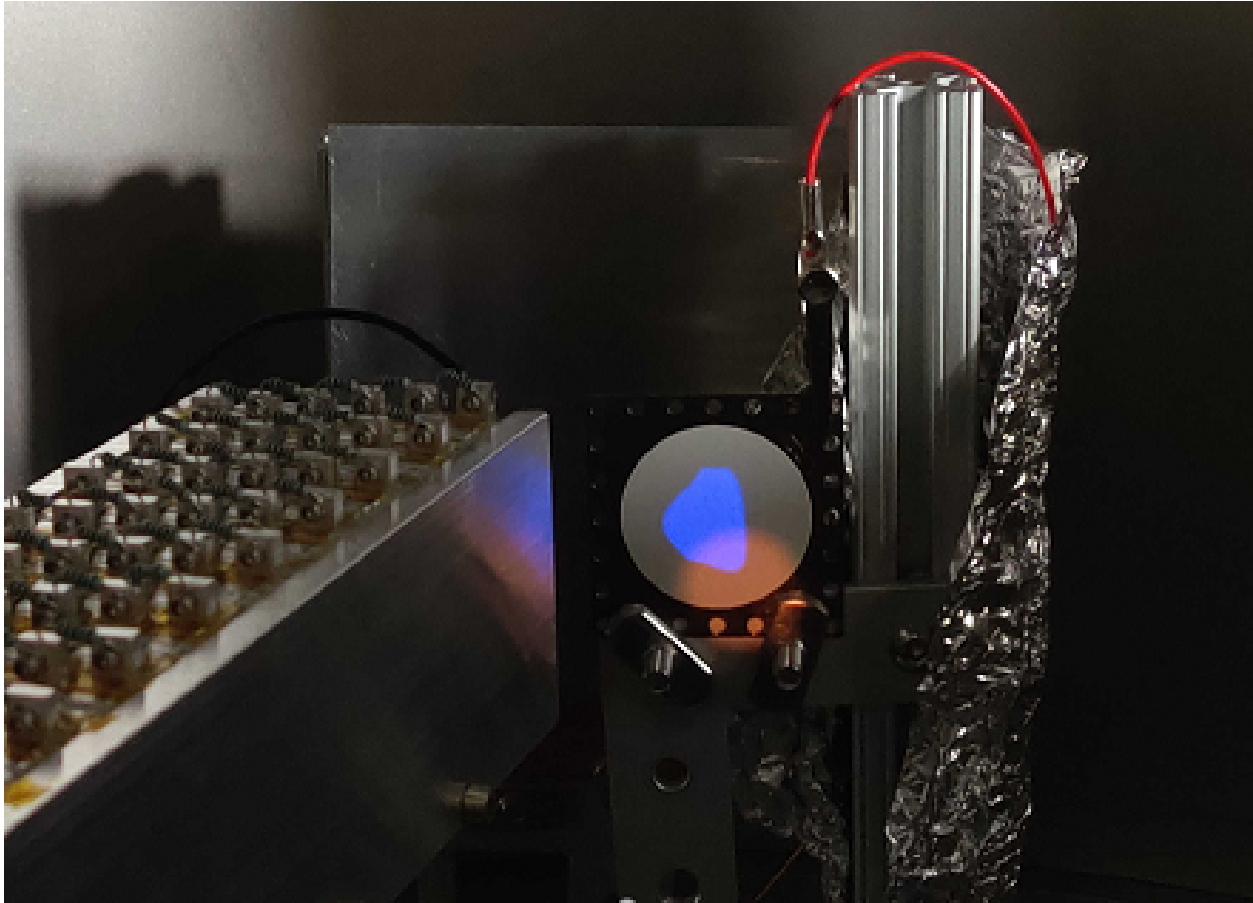
Figure 3.5: Electron beam spot visible on the phosphor screen.

space environment comes from the solar Lyman alpha line at a wavelength of 121.6 nm and an energy of 10.2 eV. The lamp is air-cooled using pressurized air from the building.

3.2.4 Detectors

3.2.4.1 Electron Energy Analyzer

One important instrument for the present work is an electron energy analyzer to measure energy spectra of the secondary electrons and photoelectrons generated on target objects. Various energy analyzer designs have been in use for decades and have extensive flight heritage. Options range from relatively simple energy analyzers, such as the retarding potential analyzer or parallel plate analyzer, to increasingly complex designs such as cylindrical, hemispherical, and top hat

analyzers. While top hat analyzers are ubiquitous on modern space physics missions (e.g. [20, 81, 91, 115]), other designs, such as the retarding potential analyzer, also fly on a wide variety of missions [72, 61, 22], often as part of a suite of analyzers.

The goal for the experimental work discussed herein is to demonstrate feasibility and obtain a solid understanding of the physics of electron-based touchless potential sensing. In light of this goal, a retarding potential analyzer (RPA) is selected as an appropriate instrument for this work. If touchless potential sensing can be demonstrated using a straightforward, inexpensive instrument, then it stands to reason that obtained insights will hold if a more advanced instrument is used.

In total, three RPAs were designed and built to measure electron energy distributions in experiments, with each design iteratively improving upon the previous. All of the experimental results presented in this dissertation were taken with the third and final RPA. The RPA consists of a front grounded grid and a variable voltage discriminating grid in front of a hollow-cylinder detector. The detector aperture is 1.27 cm in diameter. The mesh grids have a 90% transmission, with wire radii of approximately 0.01 mm, and distances between the wires of 0.3 mm. The detector itself is also 1.27 cm in diameter and is 10 cm long to reduce secondary electron escape from within the detector. Figure 3.6 shows the operating principle of the RPA. Incoming electrons with energies less than $E < qV$, where V is the voltage on the discriminating grid, are unable to overcome the potential barrier to enter the device and are thus rejected. Electrons with sufficient energy to overcome the potential barrier, i.e., with $E > qV$, enter the detector and are collected. An electron energy spectrum is take by sweeping through the voltages applied to the discriminating grid and measuring the current on the detector at each step. Figure 3.7 shows a picture of the RPA, both with and without the exterior grounded housing. A Keithley 2401 SourceMeter, controllable via LabVIEW, is used to record the current collected by the electron energy analyzer.

Several possible improvements are suggested for future research using this RPA. First, the RPA operates by collecting a current versus voltage curve, and the electron distribution is found by differentiating this curve. It is possible, however, to directly measure the electron distribution by operating the RPA in a modulated discriminating grid mode. In this case, a small sinusoidal voltage
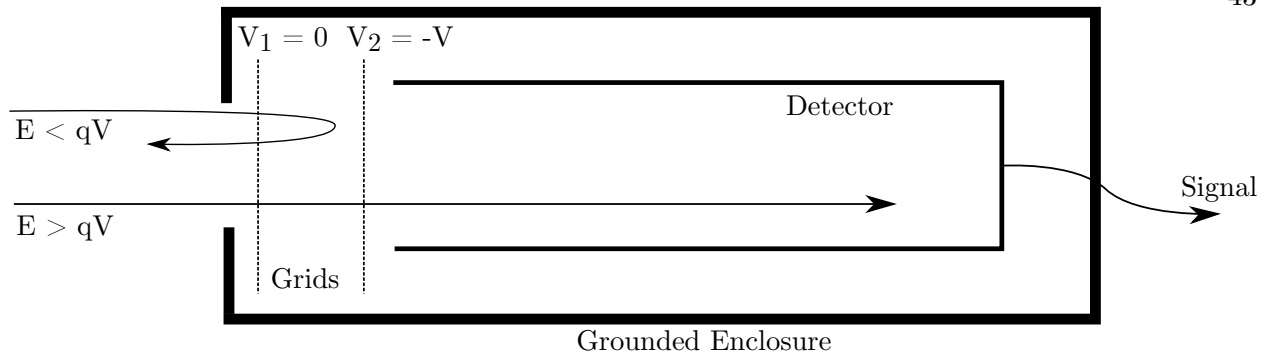
Figure 3.6: RPA operating principle.
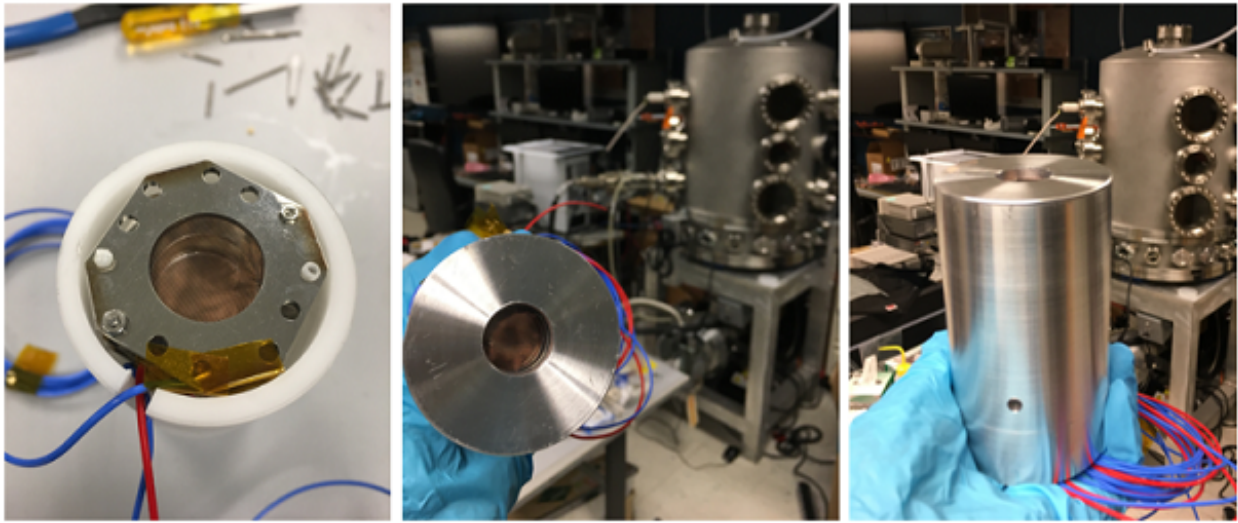
Figure 3.7: RPA, both with and without the grounded housing, used to measure electron spectra.

is added to the voltage on the discriminating grid. The output signal coupled to the sinusoidal wave is measured and electrons with energies within the range of the sinusoidal signal are directly measured. Another possible improvement is to add an electron multiplier or microchannel plate to the instrument, which would amplify the incoming electron signal and allow for measurement of very low (or even single particle) electron fluxes. Finally, future studies could consider using a different energy analyzer design (such as a cylindrical mirror or hemispherical analyzer) to touchlessly sense potential, depending on the requirements of a given experiment.

3.2.4.2   Magnetometer

A vacuum-safe version of the Stefan-Mayer FLC3-70 3-axis fluxgate magnetometer is used to measure magnetic fields. This device can measure magnetic fields up to ±200 µT with an accuracy of $1\% \pm 0.5$ µT. A typical magnetic field near the center of the chamber during experiment conditions (i.e. with the pumps running) has a horizontal component of 2.5 µT and a vertical component of 39.7 µT (positive downward). In comparison, the IGRF-13 model[1] predicts a horizontal component of 20.8 µT and a vertical component of 47.4 µT [109]. The measured total field magnitude is approximately 40 µT, whereas the IGRF-13 model predicts a magnitude of 52 µT. It is known that several components in the vacuum chamber, including the pump motors, stepper motors, and most significantly, the inverted magnetron gauge, contribute magnetic fields inside the chamber. The magnetometer measures the combination of the magnetic fields from these sources plus the geomagnetic field, which accounts for the discrepancy between the measured field and the IGRF-13 model.

3.2.4.3   Residual Gas Analyzer

A Stanford Research Systems residual gas analyzer (RGA) is used to detect and characterize traces of gas present in the vacuum system. The RGA is capable of measuring constituents with masses out to 200 amu with a resolution of 1 amu. Figure 3.8 shows an example spectrum taken by the RGA when the IMG measured a chamber pressure of 1.0 µTorr. Peaks corresponding to common gas constituents are labeled. One of the primary contributors to the chamber base pressure is water, which adsorbs on to the chamber walls when the chamber is exposed to atmosphere. Future chamber improvements should include venting the chamber with nitrogen, which is known to desorp from surfaces at a much faster rate than water. Alternatively, a bake-out system could be used to heat the chamber walls, increasing the rate at which water molecules leave the surface. A chamber base pressure in the 10^{-7} Torr range could likely be achieved with these improvements. There is

---

[1] International Geomagnetic Reference Field (IGRF), 13th Generation Calculator, http://geomag.bgs.ac.uk/data_service/models_compass/igrf_calc.html, Accessed 2020-09-17.

also a large contribution from hydrocarbons with masses from 80-200 amu. The peaks at 41, 43, 55, 57, 69, and 71 amu correspond to a known signature from turbopump oil [1]. Low-outgassing materials are used throughout the chamber, such as acetal plastic, PTFE, or PEEK, with vacuum-safe lubricants used in the motion system. However, these materials also outgas in small amounts. The presence of fingerprints or other contaminants also contribute to the residual gas environment. As these heavier particles are ionized in the RGA, the long hydrocarbon chains break into smaller units, creating a near continuous spectrum above 80 amu.
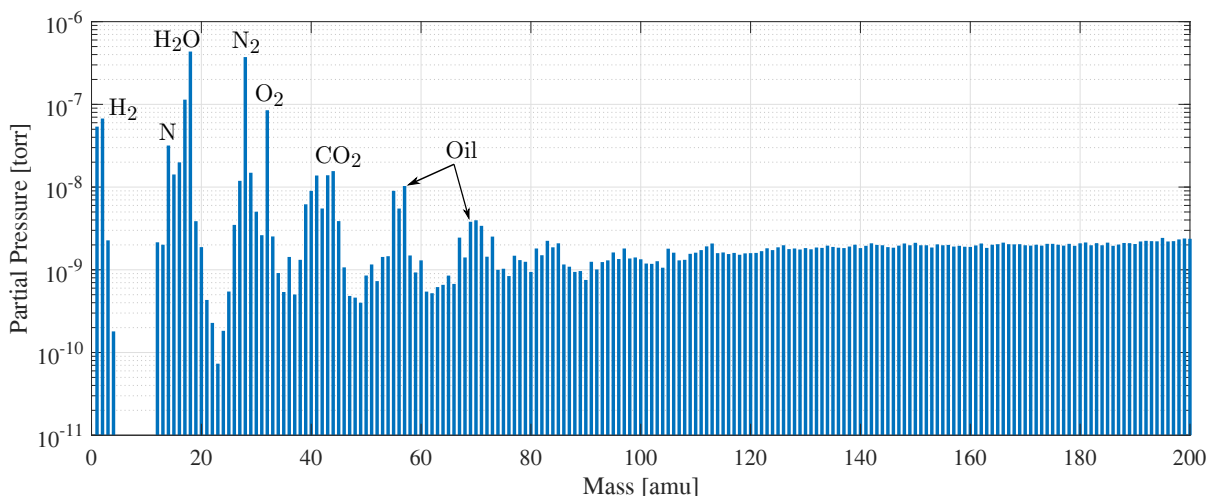
Figure 3.8: Residual gas mass spectrum taken by the RGA for a chamber pressure of 1.0 µTorr.

The RGA can also be used to provide a total pressure measurement by summing the partial pressures. In this case, the sum of partial pressures gives a total chamber pressure of 1.6 µTorr which is close to the IMG measured value of 1.0 µTorr.

The stepper motors for the in-vacuum motion stage cause a significant rise in the chamber pressure when operated, often increasing the pressure by several µTorr in less than a minute when first powered on. To determine the cause of this, an RGA spectrum was collected while the stepper motors were operating. Figure 3.9 shows the difference between this spectrum and the baseline spectrum shown in Figure 3.8, which was taken with the steppers off. The gas with the largest partial pressure is water vapor. The stepper motors are known to heat up during operation in

vacuum due to the lack of convective cooling. Water vapor adsorbed to the stepper motors boils off quickly when the motors become hot, thus creating the sudden pressure increase. As the motors are continually used, the water is removed and eventually the pressure rise is reduced. Other notable peaks include atomic hydrogen, nitrogen, and carbon dioxide. The presence of these gases may indicate there is a dead volume of air trapped inside the stepper motors which escapes when they are moved.
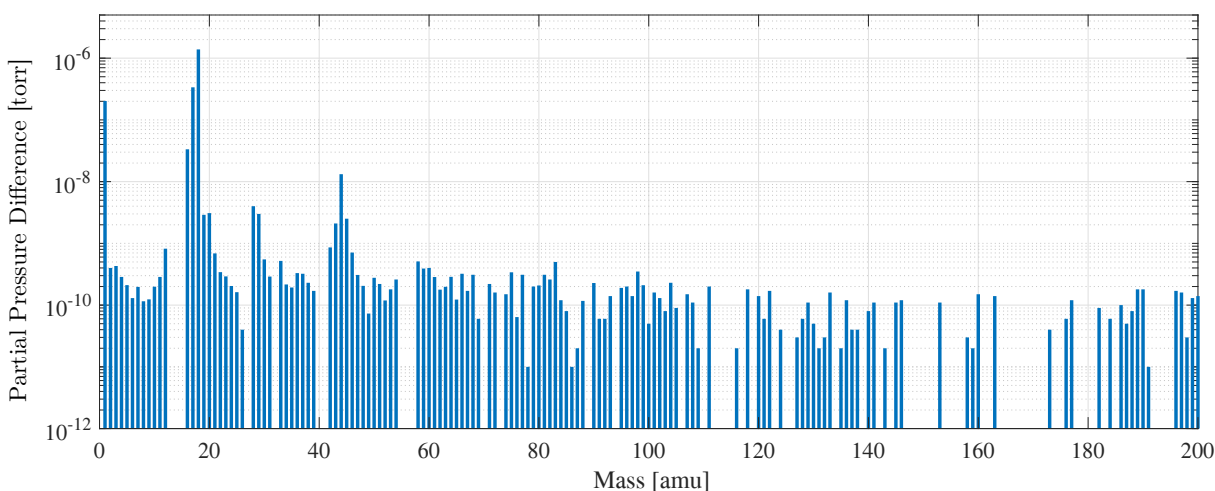
Figure 3.9: Contribution to the vacuum chamber residual gas environment from the motion system stepper motors.

3.2.5   High Voltage Power Supplies

A variety of high-voltage power supplies are available to supply voltage to the RPA discriminating grid, target objects, or any other experiment components as required. These include a Spellman CZE3000 (0 to 30 kV), two Spellman SL300s (0 to 3 kV), a Matsusada CZ9 (0 to 30 kV), and two Matsusada AU-30R1 high-voltage supplies (0 to 30 kV). The Matsusada AU series units are highly preferable to use whenever possible as they have superior voltage resolution to the other units. These provide a maximum current output of 1 mA, though typical current draws are <1 µA. Additionally, the units are computer-controlled via fiber optic cables which provides additional electrical isolation between the high-voltage and control units. All units are controllable via Lab-

VIEW except for the Spellman SL300s, which are manual control only. When output voltages are <1 kV, a Keithley DMM6500, which also interfaces with LabVIEW, measures the voltage output from the power supplies to obtain a truth value.

3.3   Results & Summary of Research Goal 2

A space environment simulation facility has been designed and developed to provide a suitable environment for experimental studies of touchless potential sensing. The ECLIPS chamber provides the required experimental capabilities for the current work, which includes a source of energetic electrons, a VUV light, in-vacuum motion, a charged particle energy analyzer, and high-voltage sources. Additional detectors, such as the RGA and magnetometer, allow for the vacuum environment to be thoroughly characterized and monitored during data collection. In addition to providing experimental capability required for the current work, the facility also provides a highly-capable space simulation chamber which will be useful for a broad range of spacecraft charging and charged astrodynamics experiments in the future.

Chapter 4

Active Sensing

4.1 Motivation

The previous chapter investigated numerous aspects of electron-based touchless potential sensing using both theoretical understanding and numerical tools. The goal of this chapter is to physically demonstrate the electron method for touchless sensing through laboratory experiments. Specifically, the active sensing case, which uses an electron beam, is considered here, whereas passive sensing with environmental currents is considered in Chapter 5.

Several factors motivate an experimental campaign. First, physical demonstration of touchless potential sensing provides more confidence in the efficacy of the electron method than is possible with only simulations and theory. This is especially true in light of the uncertainty surrounding material properties of space objects which may be targeted for potential sensing in future debris removal missions. Further, experiments provide valuable insight into what physics, if any, is not being captured in the simulations and theoretical foundations. The goals of the experimental research are defined as follows:

(1) demonstrate touchless potential sensing for a variety of common spacecraft materials,

(2) investigate the accuracy of the electron method for a wide range of operating conditions,

(3) determine the effect of relative geometries between the target and sensor.
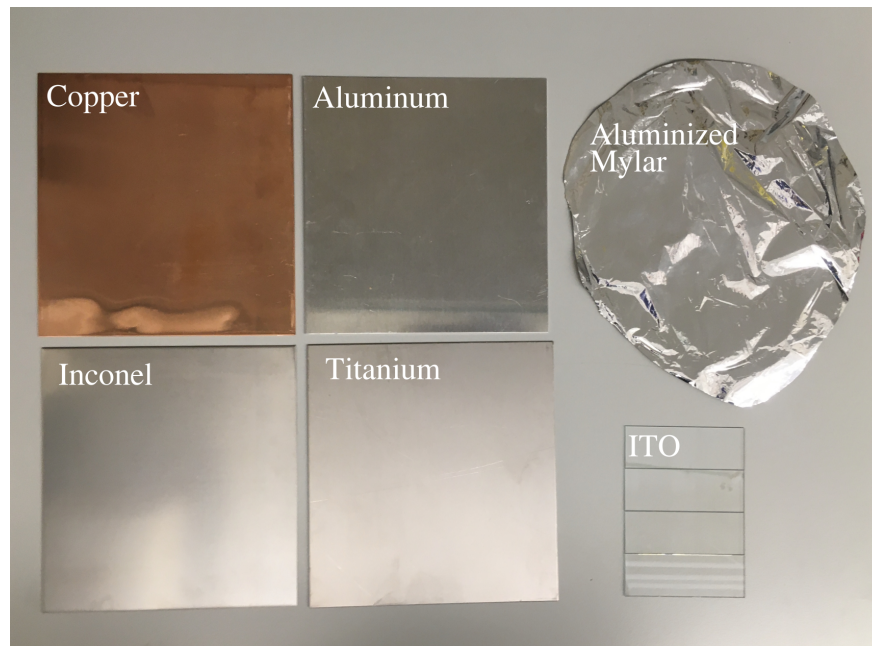
Figure 4.1: Test samples used for touchless sensing experiments.

4.2   Experiment Setup

To achieve these goals, experiments were conducted in which a flat target plate was held at a fixed, known, potential in a vacuum chamber. The plate was then irradiated with an electron beam to simulate active sensing. The resultant secondary electrons were measured using the electron energy analyzer, which was mounted on a rotating arm to sweep around the target plate. Experiments were conducted under vacuum pressures between 10^{-5} and 10^{-6} Torr. A variety of commonly-used spacecraft materials were selected as targets: aluminum, copper, and titanium are often used as base materials for spacecraft frames and thermal control systems; indium tin oxide (ITO) is a conductive coverglass applied to solar panels; aluminized Kapton is a common outer layer in spacecraft thermal blankets, and Inconel (a nickel-chromium superalloy) is a common material in rocket nozzles and components. Figure 4.1 shows each of the samples tested. The metal samples are 6×6 inch squares. The ITO samples consist of an ITO film deposited on a glass backing. The samples were cleaned with isopropyl alcohol prior to being installed in the experiment apparatus. Figures 4.2 shows a schematic of the experimental setup. Figure 4.3 shows a picture of the setup
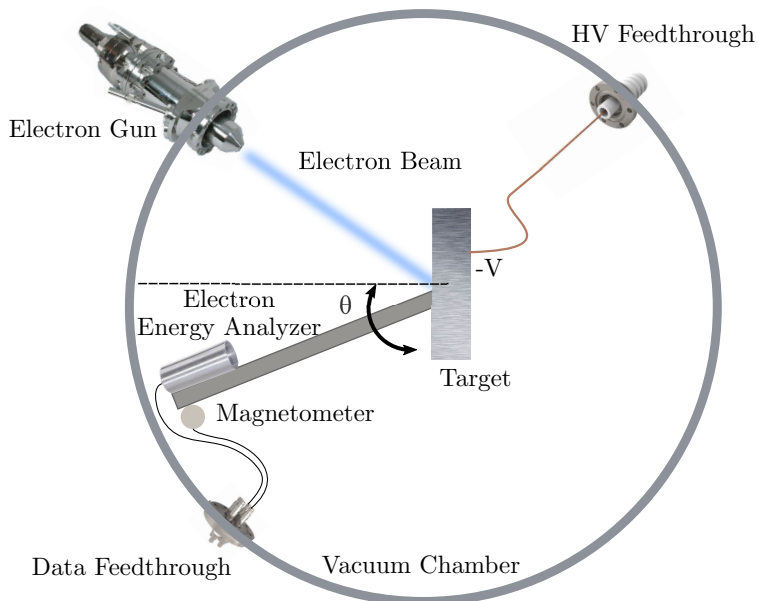
Figure 4.2: Schematic of the experiment setup inside the vacuum chamber.

with the target plate at center, above the rotational stage. The RPA is at left, mounted on the end of the rotating arm with the magnetometer. The electron gun is not pictured as it is mounted to the chamber lid. Note that the chamber walls, instrument body, electron gun chassis, and rotating arm are all grounded (i.e. everything is grounded except for the target plate, which is held at a fixed potential).

4.3   Experiment Results & Discussion

Over 580 spectra were collected in the experimental campaign for plate voltages ranging from -15 V to -6000 V [13]. At each voltage, the electron energy analyzer was swept around the plate from -30° to +90°, where the angle θ is defined so that the plate normal is at 0° as shown in Figure 4.2. The angle is defined positive in the counterclockwise direction. The electron beam had an angle of incidence on the plate of 35°. When the instrument is closest to the electron beam, θ = -30°. When the instrument is farthest from the electron beam, θ = +90°. Electron beam currents ranged from 10-110 µA and electron beam energies ranged from 1.5-10 keV. Several representative results are shown and discussed below.
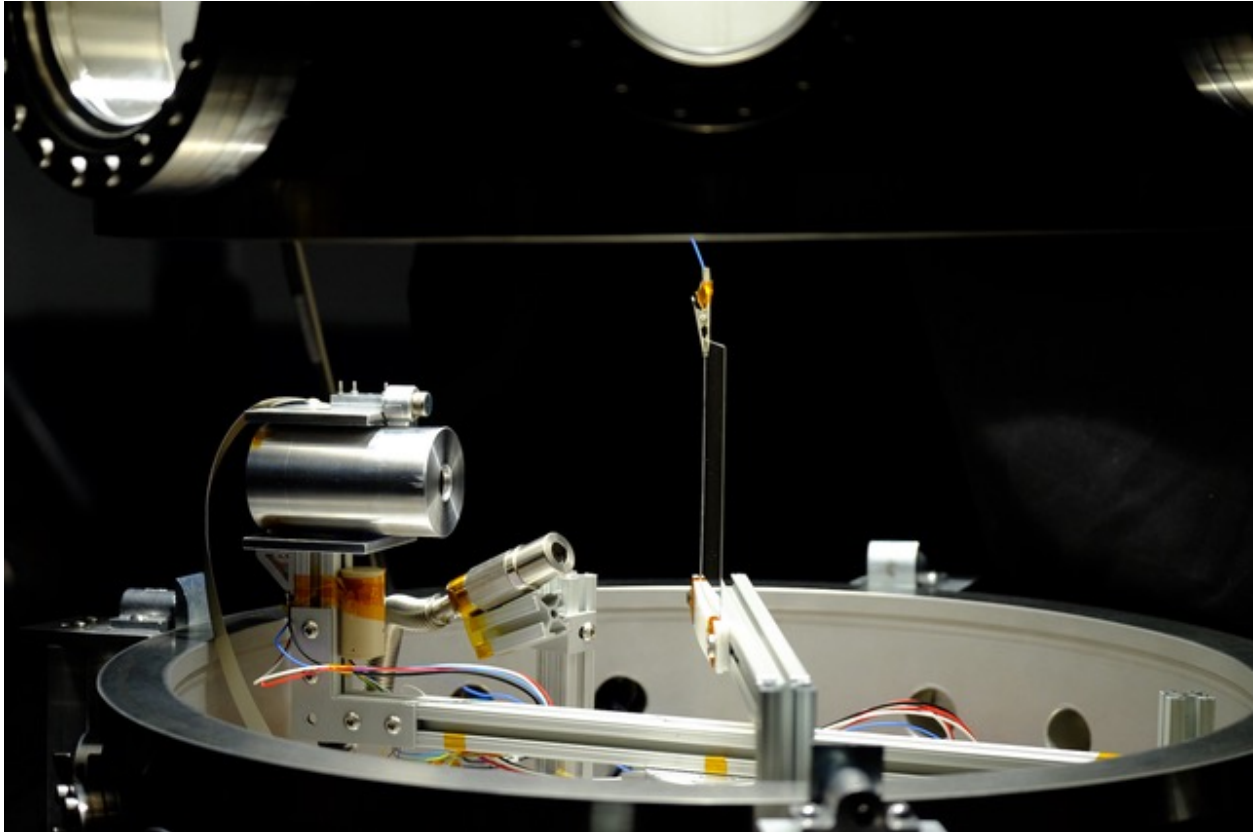
Figure 4.3: Experimental setup in the vacuum chamber. The target plate is visible in the center. The RPA and magnetometer are mounted on the rotating arm and are visible at left.

Figure 4.4 shows results for a test in which an aluminum target plate charged to -1000 V was irradiated by an electron beam current of 10.4 µA at an energy of 8.0 keV. The RPA was located at an angle of $\theta = 10°$. The left panel of the figure shows the electron current as the voltage on the discriminating grid is varied. As the grid voltage surpasses the energy of a given electron, that electron is repelled from the device and thus no longer measured. Thus, as the grid voltage exceeds the voltage on the target plate (which corresponds to the energy of the secondary electron population), the current drops to zero. The right panel in the figure shows a first-order, backward-difference numerical derivative of the data and a Gaussian fit (indicated by the solid line). The actual plate potential is given by the vertical dashed line (in both panels of the figure) and the estimated plate potential is taken to be the peak of the Gaussian (indicated by the vertical dotted line in the left panel). As shown, the estimated plate potential corresponds to the actual
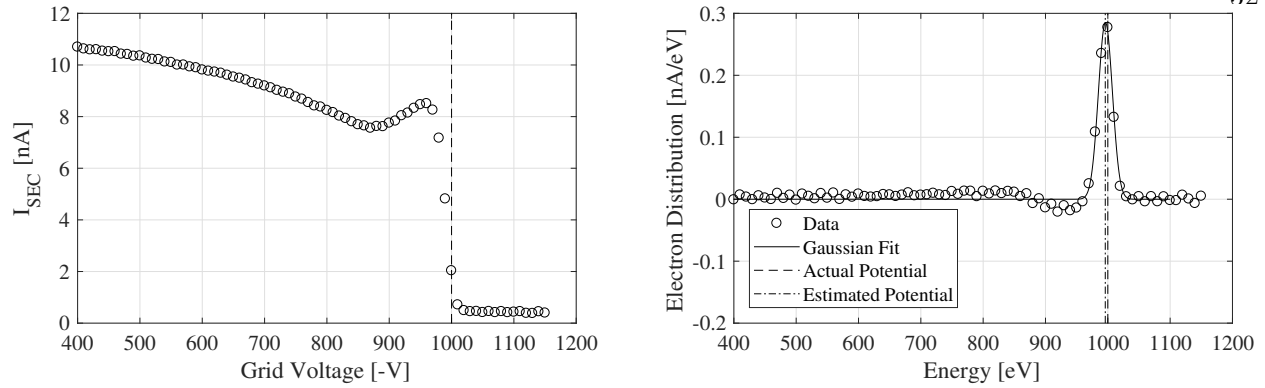
Figure 4.4: Electron spectrum for an aluminum sample charged to -1000 V and irradiated by an electron beam.

plate potential to within the voltage step of 10 V, indicating the feasibility and accuracy of the electron sensing method for potentials in the kV range. A background population of electrons is present, as indicated by the approximately -0.006 nA eV^{-1} slope between 400 V and 800 V. This population is likely generated when electrons from the target impact the walls or other surfaces in the vacuum chamber, thus generating other electrons. Additionally, the dip in current at 880 V is interesting. This dip was present in some but not all spectra. This is an artifact of backscattered electrons in the detector [103]. A backscattered electron is an electron which strikes a surface, then reflects off the surface with an energy up to its incident energy. Some of the secondary electrons from the target plate enter the detector, pass through the discriminating grid, then scatter off the detector surface and exit the detector. As the grid voltage approaches the energy of the secondary electrons from the target plate, the electrons which backscatter in the detector no longer have sufficient energy to pass through the grids on the way back out. Therefore, the backscatter current is reduced and the total detected current increases as the grid voltage approaches the plate voltage. This dip is not present in all spectra because it depends on a particular alignment between the electrons being measured and the detector. Particles which strike the side of the detector at a glancing angle scatter further into the detector, not back out.

Figure 4.5 shows an example in which an Inconel target was charged to -6000 V with the RPA located at +30°. The Gaussian fit has a maximum value of 5865 eV, whereas the actual
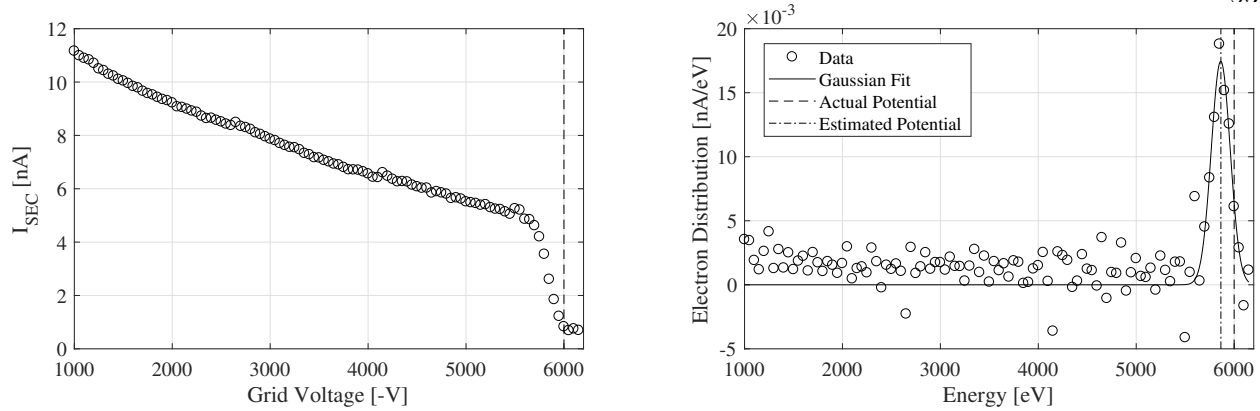
Figure 4.5: Electron spectrum for an Inconel sample charged to -6000 V and irradiated by an electron beam.

plate voltage was -6000 V. Thus, the potential of the plate is accurately sensed to within 2.26%. This error is most likely a result of the RPA being slightly misaligned to the flow of electrons from the target. The discriminating electric field in the RPA only acts upon the electron velocity component in the along-axis direction, so any angle between the incident electron and instrument results in a downward shift of the measured particle energy. This effect is discussed in more detail in Section 4.3.2.

Another representative result in shown in Figure 4.6 which illustrates the electron sensing method at low charging levels. In this case, a sample of aluminized Kapton is held at a potential of -15 V and irradiated with an electron beam current of 44.7 µA at an energy of 1.5 keV. The electron energy analyzer was located directly in front of the plate (at an angle of $\theta = 0°$). The electron distribution raw data is noisy, but the secondary electron population at 15 keV is identified by the Gaussian fitting routine and the plate potential is estimated to within 1 eV, which gives a 6.67% error.

Figure 4.7 shows an example in which an ITO sample is charged to -25 V and illuminated with an electron beam. The ITO slides were mounted on a copper backing which was held at ground. These results show that touchless sensing can be used at very small potentials in addition to large ones. The potential of the ITO target is measured to within less than a volt. In theory, the accuracy of the technique is limited by the initial energy distribution of the electrons. Further,

local surface variations or coatings can further widen the initial energy distribution. Therefore, at voltages near zero, the method produces larger percent uncertainties. However, small voltages are less of a concern because it is large voltages that lead to arcing or produce significant Coulomb forces and torques. Though a target in space irradiated with an active electron beam would likely charge to larger (magnitude) potentials, the low voltage results are included here to demonstrate the sensing technique over a range of potentials.

The typical magnetic field in the chamber during experiments is on the order of 40 µT, pointing primarily in the -Z direction (down). Figure 4.8 shows the gyroradius of an electron in a 40 µT. A 15 eV particle has a gyroradius of approximately 32 cm, whereas the separation distance
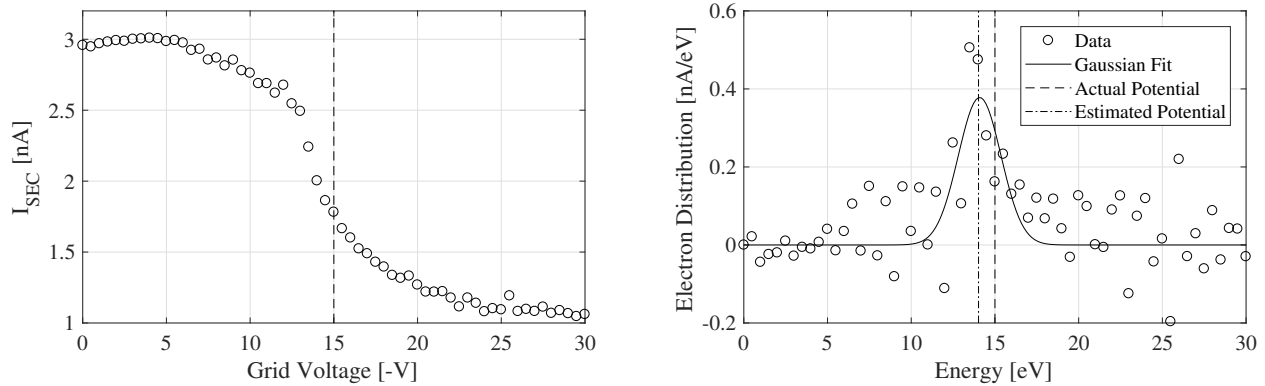
Figure 4.6: Electron spectrum for an aluminized polyimide sample charged to -15 V and irradiated by an electron beam.
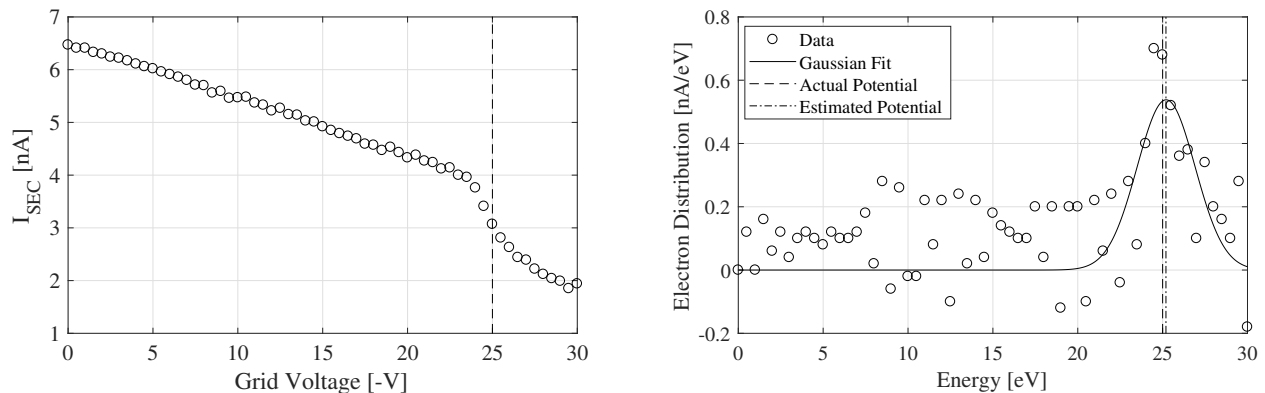
Figure 4.7: Electron spectrum for an ITO sample charged to -25 V and irradiated by an electron beam.

between the target plate and sensor was 25 cm. Thus, the electrons emitted from the aluminized polyimide at -15 V are deflected by the magnetic field, but are still able to be detected by the RPA, as shown in Figure 4.6. For higher energy populations, such as those in the 100s to 1000s of eV range, the deflection due to the gyromotion is minimal.
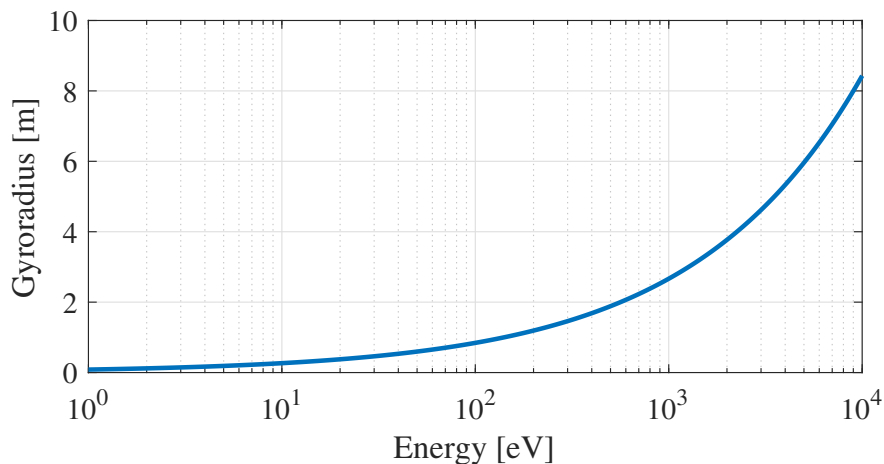
Figure 4.8: Gyroradius of an electron in a 40 μT magnetic field.

4.3.1   Data Processing Technique

RPAs and other electrostatic analyzers are used extensively in space and laboratory experiments, so a number of data processing techniques exist to determine a particle distribution from the raw current-voltage data [60, 86]. Touchless sensing is unique in that the objective is to measure an electron population at a specific energy, rather than to analyze particle fluxes across a wide-range of energies or even for multiple species. Therefore, the current-voltage curve is expected to be a downward step-function in an ideal case with the step occurring at the energy of the electron population coming off the plate. One data processing option is to fit the raw current versus voltage data with a hyperbolic tangent function, which is an analytical approximation of a step-function. The negative derivative of the hyperbolic tangent function gives the electron energy distribution, and the plate potential estimate is found by taking the maximum of the electron energy distribution. This option works reasonably well except that in many cases there is a small background distribution

of electrons which likely consists of secondary or backscattered electrons generated from other surfaces inside the chamber. Similarly, a detector in space observes the secondary electron population from the target superimposed on the environmental electron flux. As a result, the current-voltage curve has a background slope which negatively affects the fit of the hyperbolic tangent function. To account for the slope, it is possible to use a fitting function which is a hyperbolic tangent plus a linear fit. This approach models some cases quite well, but breaks down when the background is flat or when the signal is very small. Additionally, the iterative least-squares fitting routine is quite sensitive to the initial guess, which is undesirable.

Another approach is to directly compute the numerical derivative, which gives the electron energy distribution. For cases in which the electron current is much larger than the noise floor of the detection system, a clear peak is visible in the electron energy distribution (as is seen in Figure 4.4, right) which can be used as the plate potential estimate. However, the electron peak is lost for cases where the signal is on the same order as the system noise. In the right panel of Figure 4.6, for example, the peak of the numerical derivative is only slightly higher than the noise. Rather than simply taking the maximum of the electron energy distribution, a Gaussian curve is fit to the electron energy distribution. The peak of the Gaussian fit is then taken as the estimate of the target potential. Other data smoothing options, such as the Savitzky-Golay filter, could be used to improve the stability of the numerical derivative if needed [99].

The width of the fitted Gaussian also provides a metric for quantifying uncertainty. If a signal is only slightly above the noise floor, the fitted Gaussian has a large standard deviation, so the measurement should not be taken with high confidence. Alternatively, if a peak is very large, which indicates there are many electrons within a narrow energy range, the fitted Gaussian has a small standard deviation, and confidence in the measurement is high. For example, the Gaussian fit shown in the right panel of Figure 4.4 has a standard deviation of 15.89 eV which is only 1.59% of the peak location of 1000 eV. A poor quality spectrum, on the other hand, may have a standard deviation on the order of several hundred eV. This approach is useful when data from the electron method for touchless sensing may be combined with charge information about the

target from other sources, such as bremmstrahlung x-ray measurements or charge predictions based on the space environment. Measurements and uncertainties from each of these sources can then be combined in a filtering algorithm to obtain an optimal estimate of the target potential [116]. The data processing technique of taking a numerical derivative of the current-voltage curve, then fitting a Gaussian to the electron energy distribution allow for accurate potential estimation which is robust even for small signals or cases in which a background distribution is present.

4.3.2   Aggregate Results

Each of the 583 tests consists of an current-voltage curve collected at a given angle, θ, and a given plate voltage and material. The peak of the Gaussian fit to the electron energy distribution for each test is found and taken as the plate voltage estimate. This estimate is then compared to the actual plate voltage and a percent error is computed:

$$\% \text{ Error} = \frac{V_{\text{measured}} - V_{\text{actual}}}{V_{\text{actual}}} \times 100. \tag{4.1}$$

Figure 4.9 shows the percent error as a function of the angle θ for all 583 tests. The plot indicates the mean percent error and standard deviation of the distribution of all tests at a given angle. The means are very close to zero percent error for angles ranging from -20 to 60°. The standard deviations are smallest for angles between 0 and 60°. These results indicate that the electron sensing method is accurate to within a few percent error over a range of angles. At large angles, the method becomes less reliable, but the means of the percent errors across all runs are still within 16%. Several factors contribute to this result.

Interestingly, the maximum current for the electron gun experiments is not observed at an angle of zero, but rather when the detector is between 30 and 50° off the plate normal. Figure 4.10 shows the current as a function of angle for several tests. The current at each angle is averaged over grid voltages less than the plate voltage and then normalized. As the plate voltage is increased for a given beam energy, the angle of maximum current shifts to higher angles. Note that even though the secondary electrons have an initial cosine angular distribution (as discussed in Chapter 2),
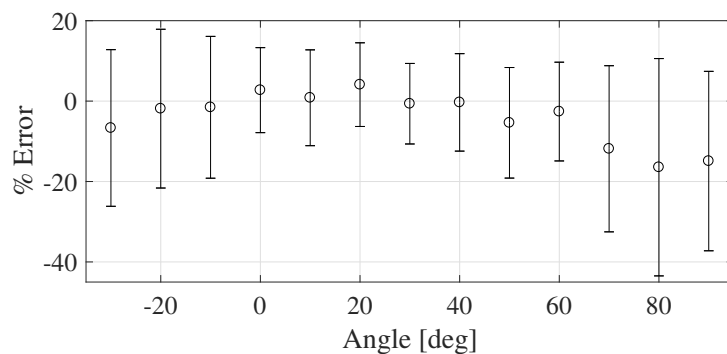
Figure 4.9: Percent error of the measured potential compared to the known potential as a function of angle for over 580 different spectra.
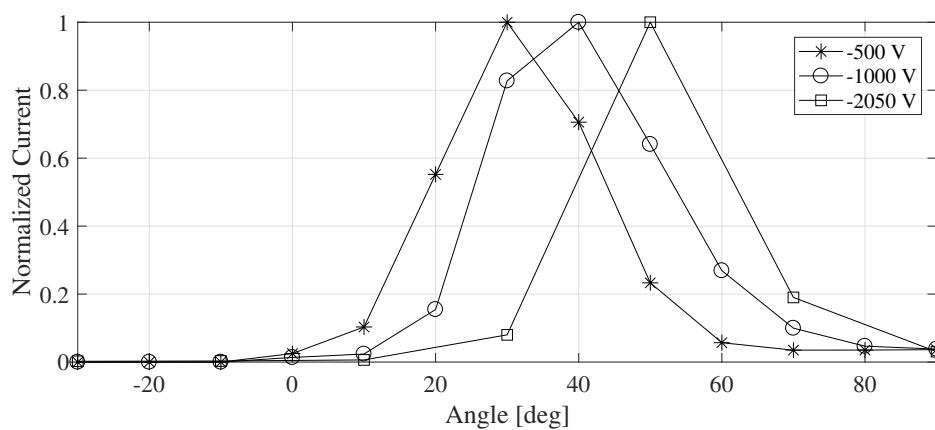
Figure 4.10: Normalized mean current as a function of angle and plate potential.
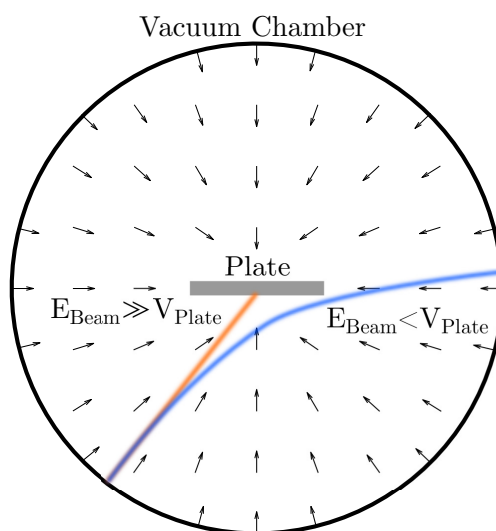
Figure 4.11: Schematic of the electron beam interacting with the plate.

the distribution observed here is caused by the initial distribution being focused by the electric field around the plate. Figure 4.11 shows a qualitative illustration of how the beam interacts with the target plate. If the beam energy is much greater than the voltage on the plate, then the beam electrons are unaffected by the plate until they impact it. In the extreme case in which the plate voltage is greater than the beam energy, the beam is deflected because the electrons cannot climb the potential hill to reach the plate. For cases in which the plate voltage is a fraction of the beam energy, the beam is deflected a small amount and impacts the plate closer to the edge. Due to the electric field geometry, indicated by the black arrows in the figure, secondary electrons generated closer to the edge of the plate fly away at an angle. Therefore, as the plate voltage is increased (in the negative sense), the beam is deflected further toward the edge of the plate, the resultant secondary electrons fly off the plate at an angle, and the maximum current is measured at increasingly large angles. This phenomenon is confirmed by observation of radiation darkened spots which developed on the target plates after extended electron beam exposure. The spots were not located at the center of the plates, but instead were offset toward the edge.

This geometry has important implications for future touchless sensing missions. For any physical object that is charged to a negative potential (negative relative to the servicing spacecraft which aims to capture the emitted electrons), there always exists a point on the surface for which the electric field maps to the servicing spacecraft. The electron beam can be expanded to illuminate the entire target which ensures that some number of secondary electrons are always detected, regardless of the relative geometry of the spacecraft. Alternatively, if electrons are only generated on a small area of the target surface, potential measurements are possible when the relative geometries between the target and servicer are appropriate to guide the electrons to the sensor). In many cases, the target may be tumbling at a high rate whereas the target potential evolves slowly in time. Therefore, measurements can still be obtained at a useful rate. These results are especially important considering that most defunct spacecraft have complex shapes with multiple solar panels, antennas, and appendages, and are generally tumbling. Chapter 6 investigates the effect of target geometry on the sensing process in more detail.
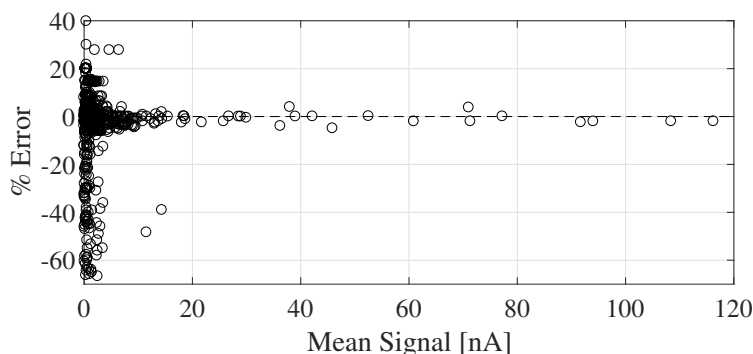
Figure 4.12: Percent error as a function of signal magnitude.

Returning to the discussion of the error distributions in Figure 4.9, it is clear in light of Figure 4.10 that the signal magnitudes decrease significantly at angles beyond 60°. As the magnitude of the peak in the electron distribution approaches the noise floor of the detection system, it becomes impossible to accurately estimate the target potential. Figure 4.12 shows the errors plotted as a function of signal magnitude. All of the tests which resulted in large percent errors had an average signal of less than 20 nA and the vast majority of these cases had an average signal of less than 5 nA. Several control tests were conducted with the electron beam off, so there was no source of electrons in the vacuum chamber and the noise floor of the measurement system could be quantified. The measured noise current has a mean of 0.0124 nA and a standard deviation of 0.0339 nA. Therefore, it becomes difficult to differentiate the peak in the electron distribution from the noise as the signal magnitude approaches single nanoamps. However, for signal magnitudes on the order of tens of nA, the electron sensing method produces an estimate of the target voltage accurate to within 4%.

Several sources contribute to the differences between the estimated and actual plate potentials, even when the signal magnitude is large. First, it is assumed that the discriminating grid inside the retarding potential analyzer produces a uniform, equipotential region of potential. Ideally, for a grid potential of V, only particles with energies $E > qV$ can penetrate the potential barrier. However, the wires which comprise the discriminating grid have finite dimensions and the regions between the wires have potentials slightly lower than the potentials on the actual wires [37].

This results in a broadening of the electron peak given by the following expression:

$$\left(\frac{\Delta E}{E}\right)_{\text{width}} = 1 - \frac{2\pi\left(\frac{d}{a}\right) - \ln 4}{2\pi\left(\frac{d}{a}\right) - 2\ln\left[2\sin\left(\frac{\pi r}{a}\right)\right]},\tag{4.2}$$

where E is the energy of the electron population, ΔE is the amount of broadening in the peak, r is the wire radius, a is the distance between the wires in the grid, and d is the distance between grids. For the retarding potential analyzer used in the experiments, the wire radius is on the order of 0.01 mm, the distance between wires is 0.3 mm, and the spacing between the grounded grid and discriminating grid is 10 mm. This gives a $\frac{\Delta E}{E}$ of 2.1%. Given a plate voltage of 1000 V, the expected broadening of the peak would then be 21 eV. The electron energy distribution given in the right panel of Figure 4.4 has a FWHM peak width of approximately 28 eV, which is consistent with this source of error. The secondary electron population is also not mono-energetic, which further contributes to the peak widening. Secondary electrons depart from a surface with a distribution of kinetic energies of a few eV. The peak of this distribution occurs at an energy equal to $\frac{1}{3}$ the work function of the emitting surface [26]. For most metal surfaces which have a work function on the order of 4 eV, the secondary electron energy distribution has a peak around 1 eV.

Another consideration for planar-type retarding potential analyzers is that the energy filter only acts upon particles in the direction along the axis of the instrument (i.e. normal to the grids). The velocity of the particle in the transverse direction is unchanged. Therefore, a shift in the measured energy can occur if particles are not traveling through the device on a trajectory parallel to the instrument axis [37]. This shift is equal to:

$$\left(\frac{\Delta E}{E}\right)_{\text{shift}} = \sin^2 \alpha,\tag{4.3}$$

where α is the angle of incidence. Electrons do not necessarily travel in a straight line between the target and sensor, depending on the electric field geometry. Two additional effects which could cause the particles to enter the detector at an angle include (1) gyrorotation about the magnetic field, and (2) misalignment of the instrument relative to the plate. The instrument is designed such that the maximum angle, α, which a particle could have and still pass through the detector is approximately 25°. This gives a $\frac{\Delta E}{E}$ shift of 18%.

In light of these sources of error, the results show that the electron method is capable of measuring the potential on a target to within 4% error when the detector measures an electron signal on the order of nA or above. At certain relative angles between the target and sensor, there is not a significant enough signal to be measured, so the method is not able to accurately measure the potential. This limitation, however, is not inherent to the sensing method, but is a result of the instrument design. More sophisticated instruments (such as those with a micro-channel plate detector) may be able to detect smaller signals and therefore accurately measure the potential across all angles.

There were no significant differences observed between the different materials tested, though most of the materials were metals with similar emission properties. Future research should consider electron emission from more complex materials, such as spacecraft thermal control paint which may comprise a large portion of a spacecraft exterior surface.

4.3.3   Voltage Sweep Considerations

One interesting consideration is selection of an appropriate size voltage step. In these experiments, the voltage of the target plate was known, so an appropriate range and step size was selected for the voltage sweep. For example, a voltage step of 0.5 V was used for the low voltage cases whereas a step of 50 V was used for the 6000 kV level tests. In space, the voltage of the target is not known a priori, so a trade-off exists between sweep time and sweep resolution. These parameters should be carefully considered when developing the mission requirements. For comparison, the electron spectrometer instruments on the MMS space physics mission can measure electron spectra from 10 eV to 30 keV in 30 ms with an energy resolution of 20% [91]. Though the time to collect a spectra from this instrument is impressive, touchless sensing missions may require better resolution. One possible solution is to collect a coarse spectra across a wide energy range, identify the energy range of the electrons emitted from the target, then conduct a finer scan over that smaller energy range. Rendezvous or tugging operations generally take place over time scales of minutes to hours, and spacecraft charge levels also evolve slowly over time (passage into or out

of eclipse being an exception). Therefore, touchless sensing missions will likely prioritize energy resolution over time resolution.

4.4   Active Sensing of Natural Potential

Throughout this work, a distinction is made between active sensing, in which an electron beam is used to transfer charge and stimulate secondary emission, and passive sensing, in which photoelectrons or secondaries generated by environmental particle fluxes are used for sensing. A critical difference between these two cases is whether or not the potential of the target is intentionally changed. For applications such as the electrostatic tractor, it is desirable to force the target to a large potential to generate large forces for tugging. Thus, an electron beam is already in use to transfer charge, so a large secondary electron population is created. Alternatively, passive sensing methods are useful when the natural potential of the target is to be measured. This, however, raises an interesting question: is it possible to use an active electron beam to sense the natural potential of the target? In other words, can an electron beam be used to stimulate secondary emission without changing the potential of the target?

Two possibilities exist in theory to achieve active sensing of a target's natural potential. The first is to use an electron beam such that it lands at the crossover point of the target's SEE yield curve (see Figure 1.8). At this landing energy, one secondary electron is produced for each incident electron, and the current balance equation is unaffected. However, this requires detailed knowledge of the target's material properties, which may be tenuous at best considering the dependence of secondary emission on temperature and surface condition, as well as the numerous different materials present on satellite exteriors. Further, the landing energy of the beam must match the SEE crossover points, but the target potential must be known to select the initial beam energy which gives the desired landing energy. Thus, this approach is clearly not practical.

A second approach is to use a very small beam current. First, consider an object charging naturally to an equilibrium potential. The orbit-limited Langmuir equation describes the current

balance of a conducting sphere at GEO [75, 73]:

$$I_e(0) \exp\left(-\frac{q_e\phi}{kT_e}\right) - I_{\text{see}}(\phi) - I_{\text{bs}}(\phi) - I_i(0)\left(1 - \frac{q_i\phi}{kT_i}\right) = 0, \tag{4.4}$$

where I_e and I_i are the environmental currents, I_{see} is the secondary electron current, and I_{bs} is the backscatter current. The spacecraft potential is denoted by ϕ. Note that the spacecraft is assumed to be in eclipse, so there is no photocurrent. The electron plasma temperature is assumed to be greater than the critical temperature required for charging onset (the number of incident electrons exceeds the number of outgoing electrons), so the spacecraft charges to a negative potential. As a result, the ions are attracted to the spacecraft and the electrons are repelled, as shown in the equation. The secondary and backscatter currents are proportional to the incident electron current, so the equation can be rewritten as follows:

$$I_e(0)(1 - \langle\delta + \eta\rangle) \exp\left(-\frac{q_e\phi}{kT_e}\right) - I_i(0)\left(1 - \frac{q_i\phi}{kT_i}\right) = 0, \tag{4.5}$$

where $\langle\delta + \eta\rangle$ represents the average secondary and backscatter coefficient across the full spectrum of incident electrons [30, 75]. Though there are a wide variety of plasma conditions encountered in GEO, some representative conditions are assumed here to allow for an order of magnitude consideration of the charging dynamics and currents. Assuming a natural plasma environment modeled by a single-Maxwellian distribution with electron and ion densities and temperatures: $n_e = n_i = 10^6$ m^{-3}, $T_e = T_i = 5$ keV, a 1.38 m radius, aluminum sphere charges naturally to $\phi = -7454$ V. Material properties are taken from the Nascap-2K spacecraft charging simulation code [30].

Introducing a beam current perturbs the potential from equilibrium:

$$I_e(0)(1 - \langle\delta + \eta\rangle) \exp\left(-\frac{q_e\phi}{kT_e}\right) - I_i(0)\left(1 - \frac{q_i\phi}{kT_i}\right) + (1 - \delta - \eta)I_{\text{beam}} = \frac{\mathrm{d}Q}{\mathrm{d}t}, \tag{4.6}$$

where Q is the charge on the spacecraft, I_{beam} is the beam current and δ and η are the secondary and backscatter coefficients at the beam landing energy, respectively. For a spherical spacecraft with radius R, the time rate of change of potential can be determined from the time rate of change
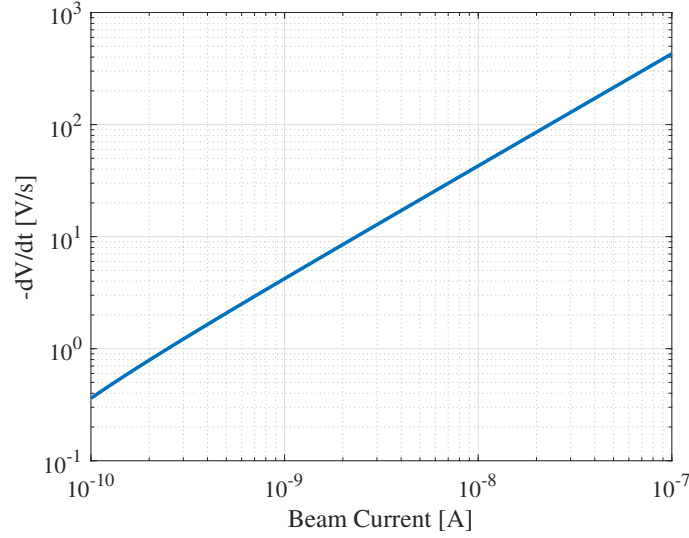
Figure 4.13: Time rate of change of potential from equilibrium for a naturally charged object hit with an active electron beam.

of charge via the capacitance:

$$\frac{\mathrm{d}V}{\mathrm{d}t} = \frac{\mathrm{d}Q}{\mathrm{d}t}\frac{1}{4\pi\epsilon_0 R}. \tag{4.7}$$

Figure 4.13 shows the initial time rate of change of potential from the natural value of -7454 V for beam currents ranging from 10^{-10} to 10^{-6} µA with an initial energy of 10 keV. Note that the potential time rate of change is the initial value. As the object's potential begins to change, the other currents adjust until the object reaches a new equilibrium. Assuming the sensing craft emits a beam in a short pulse, this plot quantifies how much the target is perturbed from its natural equilibrium. For beam currents up to about 2.5 nA, the object potential changes less than 10 $\mathrm{V\,s^{-1}}$. In theory, a sensing craft could use a quick pulse of a nA level beam to measure the object potential without significantly changing it. However, for larger beam currents, the potential varies significantly, so it would be unclear what potential is actually being measured.

Figure 4.14 shows the secondary current produced by the incident beam using a secondary emission model given in Reference [96]. At the beam landing energy of $E_{\mathrm{beam}} - \phi = 2546$ eV, $\delta = 0.1847$. For incident currents in the range of 1 nA, the secondary electron current produced by the beam is on the order of 0.1 nA. In contrast, the secondary electron current produced by
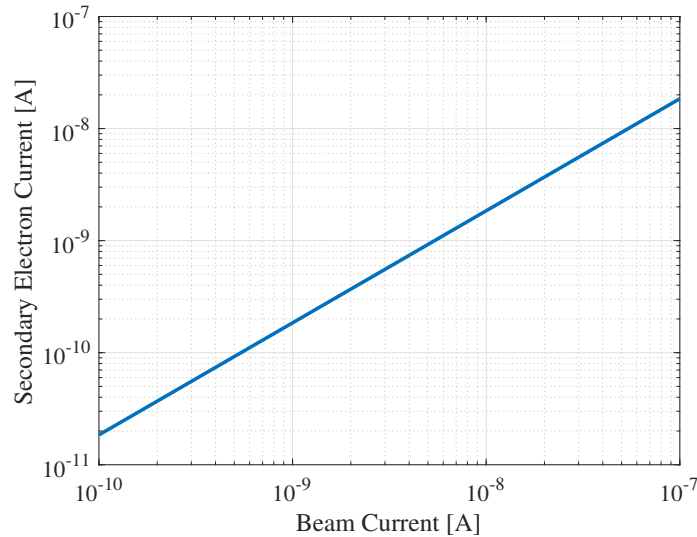
Figure 4.14: Secondary current produced by a beam incident on a naturally charged object in equilibrium.

the ambient electron fluxes is on the order of 100 nA, more than three orders of magnitude larger. This result makes sense given the nature of the current balance equation. To generate a secondary current which is larger than the natural secondary current, the incident beam current must be larger than or at least on the same order as the natural incident electron current. Thus, any incident beam which is large enough to stimulate a significant secondary electron population is also large enough to perturb the target from its natural potential.

However, the naturally-produced secondary electron current is emitted from all sides of a spacecraft, whereas the beam-induced secondary current is only emitted from the area on which the beam is incident. Thus, depending on the geometry of the target, the separation distance, and the detector on the sensing craft, the beam-induced secondary current could be on the same order as the environment-induced secondary current in some scenarios. At this point, the question of whether or not it is possible to use active sensing to measure the natural potential is mission specific. If the goal of a mission is to measure the natural potential of the target with high accuracy, it would likely be best to use only the natural currents to obtain a measurement. In other cases, it may be possible to use a short pulse of a low-current electron beam to stimulate a larger secondary

electron signal. Due to uncertainties about the target (material properties, whether or not it is continuously conducting, etc.), it will not be known exactly how much the active beam perturbs the target, even in a short time. Thus, passive methods are better for sensing the natural potential of a target. This approach is discussed further in the following chapter.

4.5   Results & Summary of Research Goal 3

Active touchless potential sensing of a target has been demonstrated through extensive laboratory experiments. An algorithm has been developed which automatically processes current-voltage data to determine an estimate and uncertainty for the target potential. The experimental results demonstrate the accuracy of the active potential sensing technique for a range of target materials, voltages, and angles. It has been shown that the method is accurate to within 4% error when the signal magnitude is on the order of 10 nA or above. Sources of error have been considered and the primary sources involve the instrument and experimental design, rather than the touchless sensing method itself. The materials tested were primarily metals, and no significant differences in sensing potentials on the different metals was found. Future work should consider conducting similar experiments with non-metallic samples, such as thermal control paints which may cover a large part of a spacecraft exterior. Another key result is that the relative geometry between the target surface normal and the detector has a large impact on the signal magnitude because the electric field near the target determines the trajectory of the electrons. The effect of target geometry on the sensing process is analyzed in detail in Chapter 6.

Chapter 5

Passive Sensing

5.1   Motivation

This chapter considers sensing of the target potential using electrons stimulated through interactions with the local space environment. Passive sensing differs from active sensing in that there is no electron beam to be directed from the sensing craft to the target. Therefore, the natural potential of the target is measured. Passive sensing is useful for a wide variety of applications, such as checking potentials prior to docking with another spacecraft, on-orbit missions to study spacecraft charging, or any other mission where the natural potential of another object is of interest.

Either photoelectrons or secondary electrons can be used for passive sensing. Photoelectrons are generated when a surface is exposed to light with energy sufficiently large to excite an electron beyond the surface's work function. Secondary electrons are generated passively when electron and ion currents from the environment impact a spacecraft surface. In general, the photoelectric current dominates the other environmental currents, so spacecraft in sunlight tend to only charge a few volts positive (at which point the low energy photoelectrons can no longer escape from the surface and a current balance is achieved). One of the case studies presented in Chapter 2 shows how touchless sensing can still be achieved in this case. A sensing craft which is at a larger positive potential than the target can attract enough electrons out of the target photoelectron sheath to obtain a measurement.

It is also possible, however, for a satellite to charge negatively in sunlight. The SCATHA spacecraft, for example, was measured to charge several hundred volts negative even in the sun-

light [87]. This can occur if the photoelectric current is significantly reduced through self-shadowing or reduced photoyield. Consider a long, thin cylinder with one of the cylinder ends pointing in the sun direction. The photoelectric current is only emitted from the small, illuminated area, whereas the remainder of the object is exposed to the electron plasma current, which causes it to charge negative (the electron current in GEO generally being larger than the ion current). Alternatively, a highly-reflective surface can charge negatively because a large fraction of incident photons are reflected rather than absorbed into the surface, so the photocurrent is reduced. These are interesting cases for touchless sensing because the object is in sunlight, but large potentials can still develop which leads to risk of arcing or parasitic forces and torques when in close proximity.

NASA's Lunar Gateway mission is a highly relevant example for which passive sensing of potential would be beneficial. Docking maneuvers are being planned between the Orion spacecraft and the Gateway in which Orion is completely shadowed by the Gateway, leading to potential differences on the order of kilovolts [50]. To prevent the risk of electrostatic discharge, initial contact is to be made via a resistor. Computer models are being used to determine the appropriate resistor size for safe discharging of the potentials. However, the ability to passively sense the potential difference between the Orion and Gateway during final approach would be invaluable to ensure the potential difference is within a safe range for a given resistor.

5.2 Passive Sensing Using Photoelectrons

To investigate the use of photoelectrons for sensing, the experimental setup described in Chapter 4 was used again, except the VUV light source was used in place of the electron gun. Figure 5.1 shows results for an Inconel sample charged to -500 V and irradiated by the VUV light. The RPA was located at an angle of -10° relative to the surface normal. In this case, the photoelectron spectra is remarkably clean and the peak at 500 eV is easily determined using the Gaussian fitting technique described in the previous chapter giving a percent error of 0.19%. Figure 5.2 shows data for a titanium plate charged to -20 V and irradiated with the VUV light when the RPA was directly in front of the plate. Even though the signal is much lower than in the
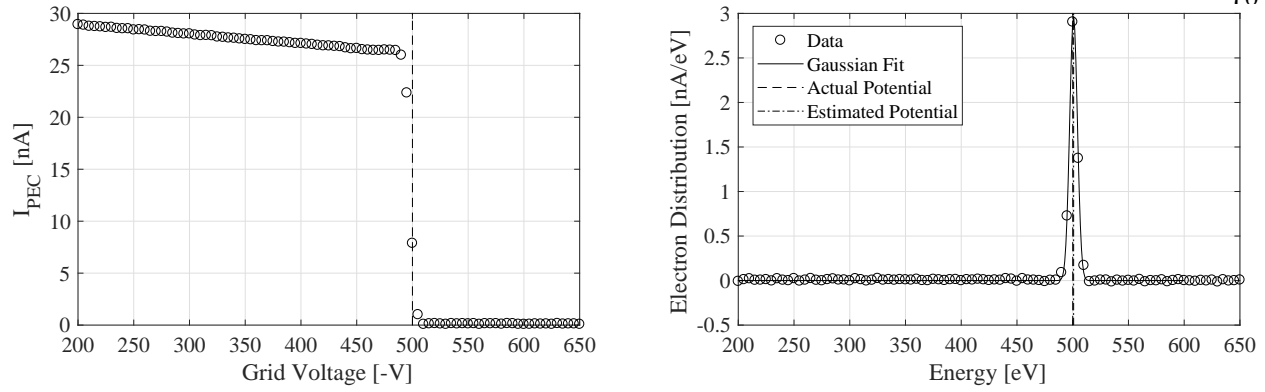
Figure 5.1: Electron spectrum for an Inconel sample charged to -500 V and irradiated with VUV light.
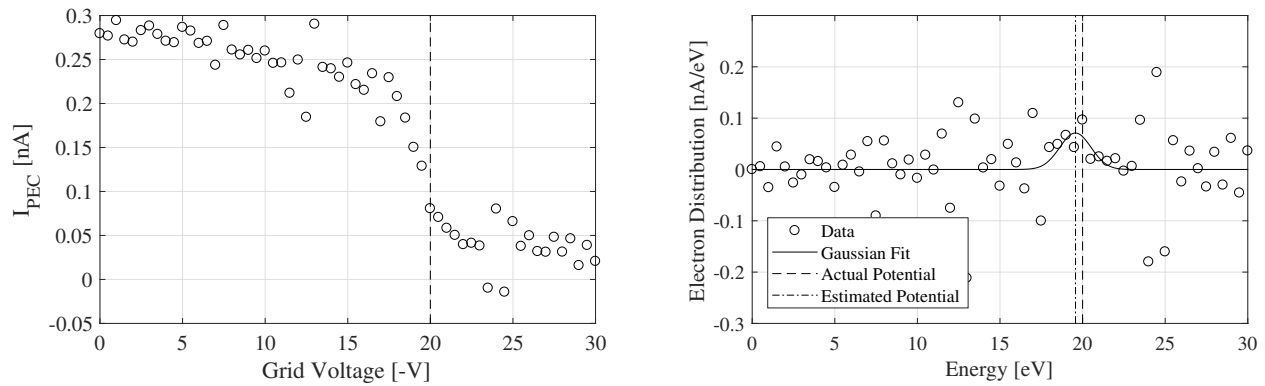
Figure 5.2: Electron spectrum for a titanium sample charged to -20 V and irradiated with VUV light.

previous spectrum, the potential on the plate is accurately sensed using photoelectrons to within 0.5 V.

As discussed in Chapter 4, the incident electron beam can be deflected by the target plate which affects the angles at which secondary electron currents are measured. This effect is not present in the data collected using the VUV light because the incident photons are unaffected by the electric fields around the target plate. Figure 5.3 shows the same results as in Figure 4.10 with results from the photoelectron tests now included. Whereas the shift to higher angles is visible in the tests conducted with an electron beam (solid lines), the peaks for the VUV light tests (dashed lines) are centered closer to zero and are not significantly affected by the voltage on the plate.

One interesting aspect of sensing with photoelectrons is that for cases in which the target
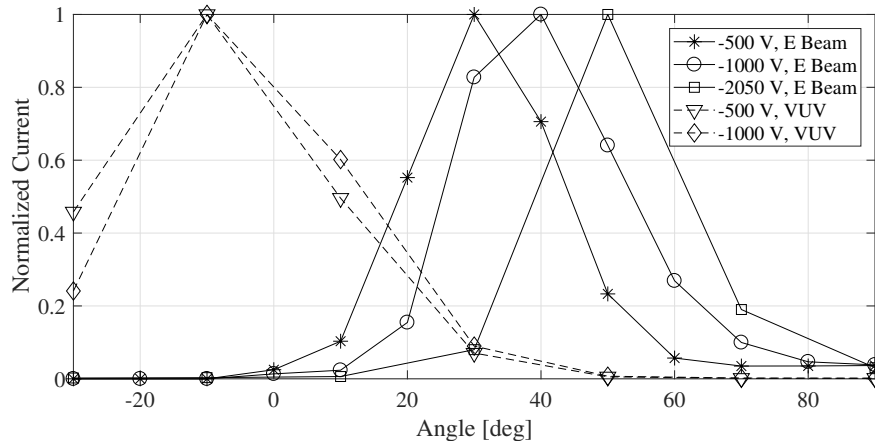
Figure 5.3: Normalized electron current as a function of angle for both VUV light and electron beam tests.

charges negatively, the sensing craft must observe the sunlit side of the target. If the target is charged only a few volts positive, the sensing craft can extract electrons from the photoelectron sheath around the target by charging to a larger positive voltage. However, if the target is charged negative, the photoelectrons are ejected into space away from the surface on which they were generated. It is unlikely that a sensing craft on the shadowed side of a target would be able to detect any of the photoelectrons. This means that the ability to sense the photoelectric current is coupled to the spacecraft relative motion and orbital dynamics. It would be advantageous to be able to passively sense potential at all times during an orbit (including in eclipse). To this end, Section 5.4 discusses passive sensing using secondary electrons generated by interactions with environmental currents. The following section considers the effect of biasing the sensing craft largely positive to attract more of the photoelectron current.

5.3   Experiment with RPA Biased Positive

All experiments thus far have involved a target being charged negative and the RPA kept at zero potential. However, in space, the sensing craft is able to adjust its own potential to attract electrons emitted from the target. Therefore, an experiment was conducted in which the RPA itself was biased to positive potentials to attract larger currents.
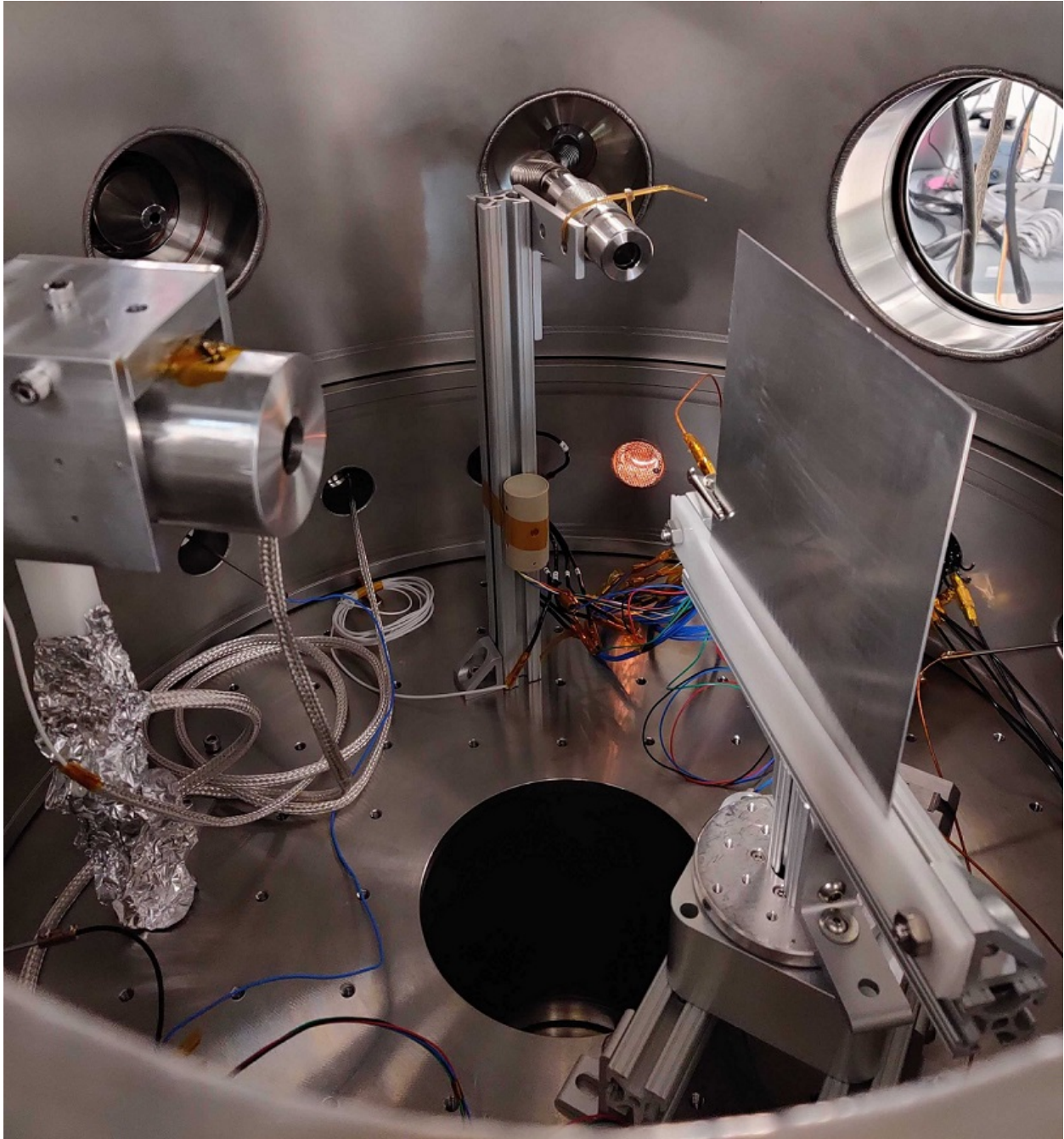
Figure 5.4: Setup for experiment in which the RPA was biased positively. The target plate is at right, mounted on the rotating plate. The RPA is at left, mounted on the insulating rod for electrical isolation. The VUV lamp (visible in the center), is directed at the target plate to stimulate photoemission.

Figure 5.4 shows a picture of the experiment setup. The RPA was mounted on an insulating

Delrin plastic rod which was bolted to the chamber floor, as seen in the left side of the figure. This
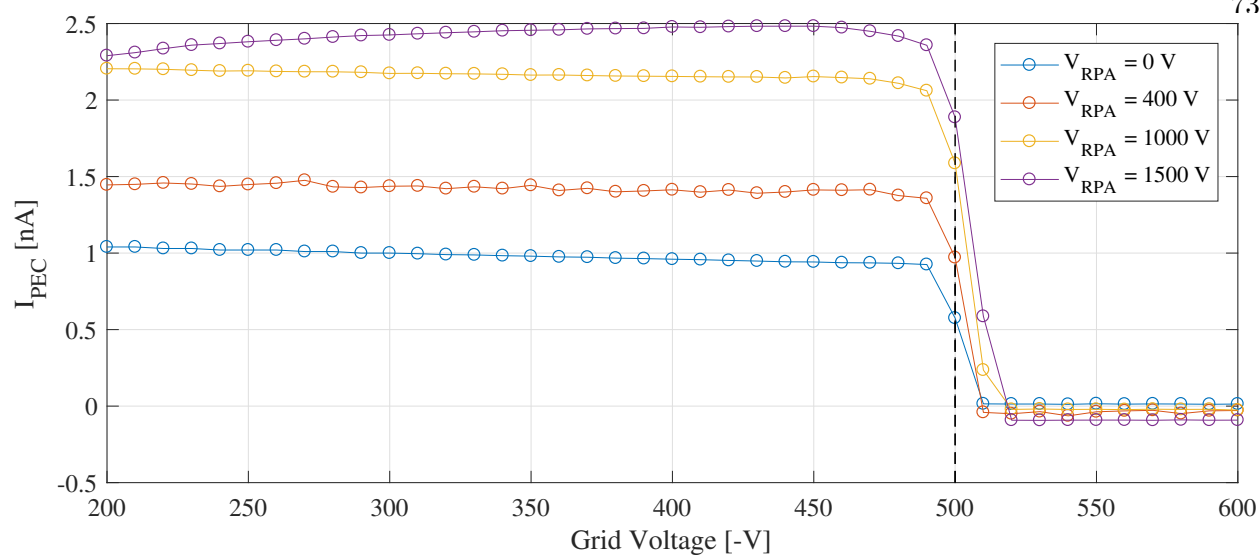
Figure 5.5: Spectra for an aluminum target charged to -500 V and various voltages applied to the RPA.

ensured the RPA was electrically isolated from the rest of the chamber so that it could be held at positive potentials. Aluminum foil was wrapped around the Delrin support to prevent buildup of charge in the insulation while still keeping the RPA chassis isolated. An aluminum plate was used as a target, which is shown on the right of Figure 5.4. The VUV source is visible in the center of the figure. The plate is shown in a rotated position. During data collection it was rotated to face toward the RPA.

Figure 5.5 shows example results for the aluminum target charged to -500 V and voltages of $V_{RPA} = 0$, +400, +1000, and +1500 V applied to the RPA. There is a clear increase in the collected current with increasing voltage on the RPA which is consistent with the expectation that a positively biased sensor attracts more electrons. Note that the population of electrons from the target plate is detected at an energy of 500 eV. This occurs because the potential on the discriminating grid in the RPA was defined relative to chamber ground, rather than to the floating RPA chassis. The front "grounded" grid in the RPA was floating at the same potential as the RPA chassis. Therefore, the potential of the sensor has in effect already been subtracted out of these spectra.
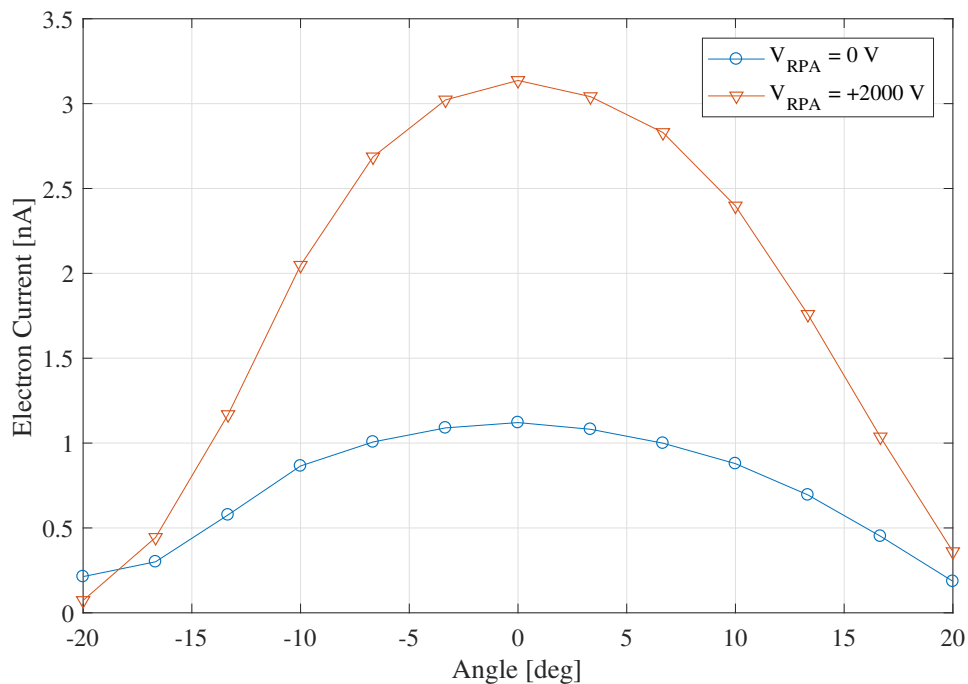
Figure 5.6: Measured current as a function of plate angle for $V_{\mathrm{RPA}} = 0$ and $+2000$ V.

An additional experiment was conducted in which the aluminum plate charged to -475 V was rotated while the RPA was kept in place. This is representative of an on-orbit scenario in which the target object is tumbling while the sensing craft is maintaining a constant position with respect to the sun and to the target. Figure 5.6 shows the current as a function of the plate angle. A plate angle of zero indicates that the plate is facing the RPA. At the peak, the current collected by the RPA when biased $V_{\mathrm{RPA}} = +2000$ V is 2.8 times greater than the current collected by the grounded RPA. Interestingly, the peak for the biased RPA is taller but not wider than the peak for the unbiased case. This indicates that the biased RPA is able to attract electrons which were already traveling in the vicinity of the RPA, but it does not capture electrons which left the plate traveling in a different direction.

5.4   Passive Sensing Using Environmental Plasma

5.4.1   Analysis

The photoelectron current typically dominates the environmental currents and limits surface charging to small positive voltages. Objects in eclipse are therefore more likely to charge to large negative potentials. For many cases in which it would be desirable to monitor a target's potential (i.e., significant negative charging), the photoelectron current will not be present. Therefore, it is desirable to passively sense potential by a means other than the photocurrent. Secondary electrons generated when environmental electron and ion currents interact with the target can be used for this purpose. This technique is also advantageous because secondaries are generated on all surfaces of the target spacecraft, so the sensing craft is not required to fly on the sunlit side to observe a signal.

To investigate the feasibility of passive sensing with natural secondaries, the Nascap-2K charging simulation software is used to quantify an order of magnitude for the secondary electron current in a variety of plasma conditions [30]. Though there are numerous different factors which affect spacecraft charging in GEO (empirical versus Maxwellian plasma distributions, secondary emission and backscatter models, etc.), the purpose of this research is to obtain an order of magnitude estimate for the total secondary current, so several assumptions are made here. The target object is assumed to be an aluminum cube 1 m on each side. The photoelectron current is turned off because the object is assumed to be in eclipse (or the photoelectron current is assumed to be small enough to allow for negative charging). A Maxwellian plasma distribution is used with a range of plasma densities and temperatures which are representative of GEO conditions. The conditions were selected to cover the range of minor charging (Case 1, -40 V) to worst-case conditions (Case 4, -24.8 kV). Table 5.1 shows the electron and ion densities and temperatures for each case, along with resulting spacecraft potential, secondary electron current induced by incident electrons ($I_{\mathrm{SEE,e}}$), secondary electron current induced by incident ions ($I_{\mathrm{SEE,i}}$), and total secondary electron current ($I_{\mathrm{SEE,total}}$). The secondary current produced by incident ions is often neglected in basic

spacecraft charging models, but the Nascap results show it can be on the same order of magnitude as that produced by incident electrons, so it should be included. As seen in the last row of the table, the total secondary electron current emitted from the target is the range of tens to hundreds of nA.

The total secondary current is emitted from all spacecraft surfaces (assuming no surfaces are blocked), unlike the photocurrent or beam-induced secondary currents which are only emitted from irradiated surfaces. Assuming the total secondary current is emitted isotropically into space, the measured signal depends on the solid angle subtended by the sensing craft. In reality, the electrons will fly away from the target with some directionality which depends on the target geometry. This effect is discussed in Chapter 6, but it is sufficient here to make the isotropic assumption to obtain an order of magnitude estimate for the signal. The secondary electron flux is determined by:

$$F_{\text{SEE}} = \frac{I_{\text{SEE}}}{4\pi d^2}, \tag{5.1}$$

where d is the distance away from the target object. Assuming the sensing craft can capture electrons within a circle of radius r (determined by its own size and how strongly it is biased positive), the current measured by the sensing craft is:

$$I_{\text{SEC}} = F_{\text{SEE}}\pi r^2 \tag{5.2}$$

$$I_{\text{SEC}} = \frac{I_{\text{SEE}}}{4\pi d^2}\pi r^2, \tag{5.3}$$

Table 5.1: Plasma conditions used to model charging in Nascap-2K and resultant secondary electron currents

	Case 1	Case 2	Case 3	Case 4
n_e, cm^{-3}	0.1	0.1	1	1.12
T_e, keV	2.5	3	5	12
n_i, cm^{-3}	0.1	0.1	1	0.236
T_i, keV	2	3	5	29.5
Spacecraft Potential, eV	-40	-1255	-4324	-24810
$I_{\text{SEE,e}}$, nA	76.03	49.93	297.8	84.96
$I_{\text{SEE,i}}$, nA	2.063	4.952	123.5	137.8
$I_{\text{SEE,total}}$, nA	78.093	54.882	421.30	222.76
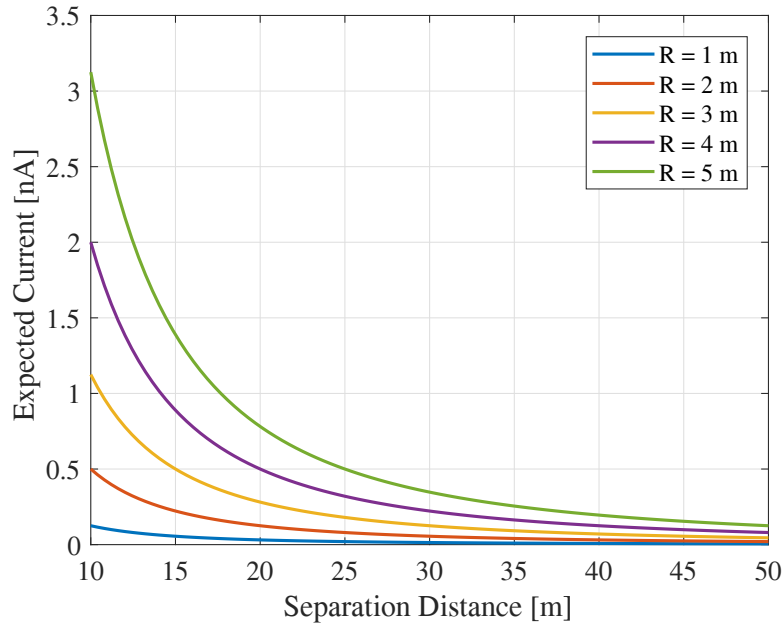
Figure 5.7: Expected secondary electron current as a function of separation distance for various sensing craft sizes.

where I_{SEC} indicates the captured secondary electron current and I_{SEE} is the emitted secondary current. Figure 5.7 shows the measured secondary current as a function of sensing craft distance and size assuming the target emits a secondary current of 50 nA. The measured current is on the order of a few nA, which is sufficiently large to be measured. For example, Figure 5.2 shows the potential of a target can be sensed for currents less than a nA. The secondary current from the target is at a very limited energy range, so it should be observable even when measured in a background plasma. Of course, the range of measurable currents is specific to a given instrument design. The operating distance, plasma conditions, and overall objectives must be considered when designing a sensing craft and instrument for a specific mission. However, it is reasonable to conclude a sensing craft with an appropriately designed instrument could measure the secondary electron current emitted from a target over realistic sensing distances. Therefore, passive potential sensing using only environmentally-generated secondaries is determined to be feasible.
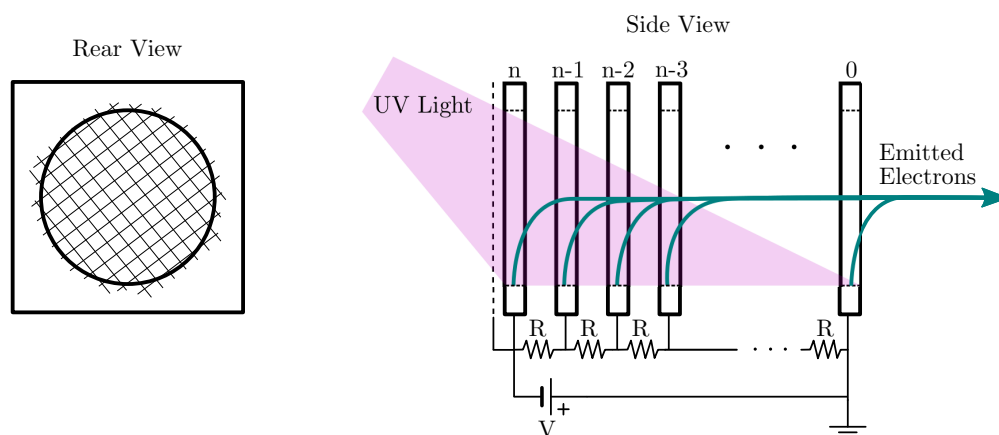
Figure 5.8: Schematic of the broad-spectrum electron gun design and operation.

5.4.2   Design of a Broad-Spectrum Electron Gun

During the investigation of using ambient electrons for passive potential sensing, a review of the literature made it apparent that there is a not a straightforward and experimentally-tractable means of producing electrons with a spectrum of energies for laboratory experiments, as conventional electron guns are monoenergetic only. A novel concept for a broad-spectrum electron gun was conceived and developed to enable laboratory testing using environment-representative particle fluxes. The design and development of this device is discussed below. The device was used to demonstrate passive sensing using broad-spectrum fluxes in the laboratory. Results from this experiment are shown in Section 5.4.4.

Figure 5.8 shows a schematic of the electron gun operation. Ultraviolet light is used to stimulate photoelectron emission inside a hollow tube, which consists of a series of n individual stages aligned along the tube axis. The stages are each held at different potentials using a voltage divider circuit. They are stacked together with thin Delrin insulators in between each stage for electrical isolation. The circular shape of each ring acts like an Einzel lens to focus the electrons toward the center of the device and into a beam. Each stage being held at a different potential sets up an electric field along the length of the device that accelerates the electrons toward the aperture. The forward most stage is at zero potential, which contains the electric fields within the device. The
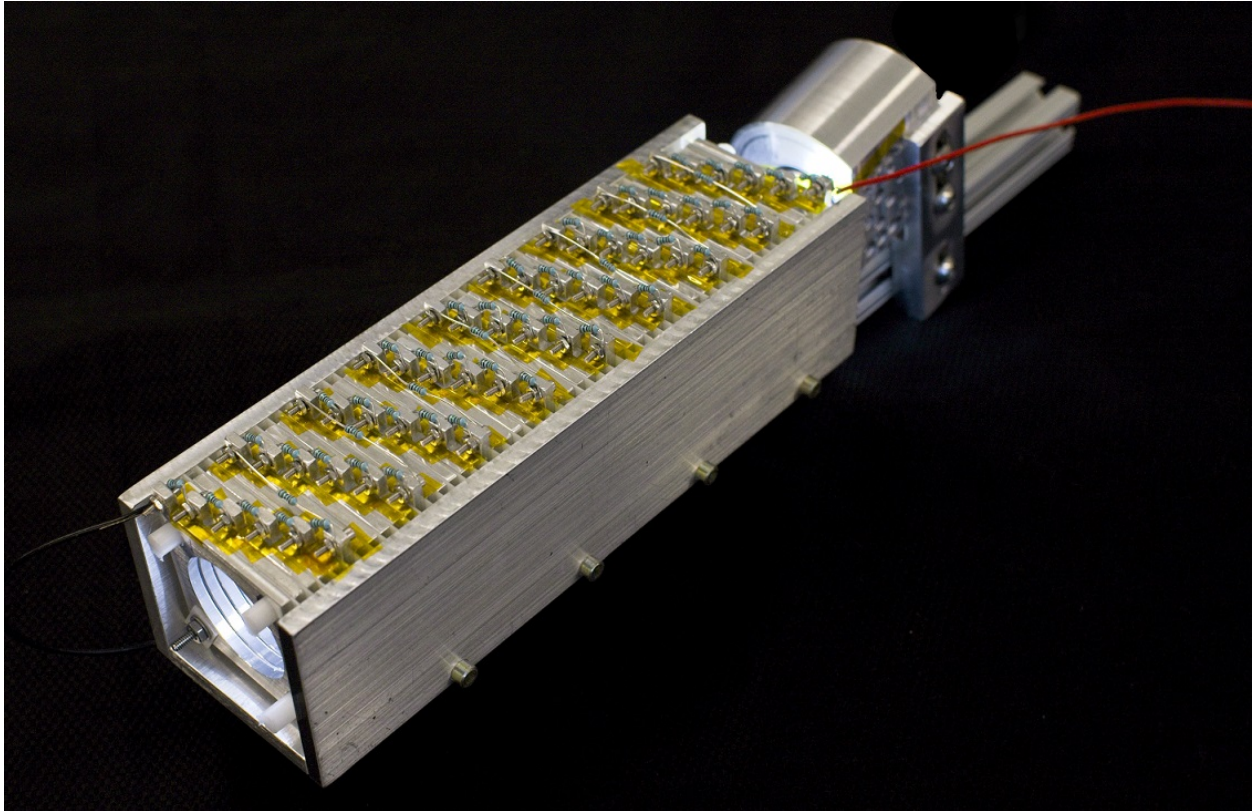
Figure 5.9: Picture of the broad-spectrum electron gun.

rearward most stage has a grid placed over the aperture which allows the UV light to shine in but also contains the electric fields. Each electron is generated on a plate at a given negative voltage, then accelerated toward the front of the device which is grounded. Therefore, the final energy of each electron is equal to the (negative) voltage of the plate on which it was generated. This design enables the device to emit an electron beam with a total number of energies equal to the number of stages. In the current design, 54 stages are used which yields a near-continuous approximation of a spectrum. Figure 5.9 shows a picture of the current design of the broad-spectrum electron. The aperture is at the lower left of the image and the mount for the VUV light is located at top right.

Figure 5.10 shows several example spectra from the broad-spectrum electron gun compared to data from the Los Alamos National Lab geosynchronous satellites recorded over more than a full solar cycle [110]. The solid lines on the plot indicate different output settings for the broad-spectrum electron gun (the maximum output energy is easily adjustable) creating spectra with
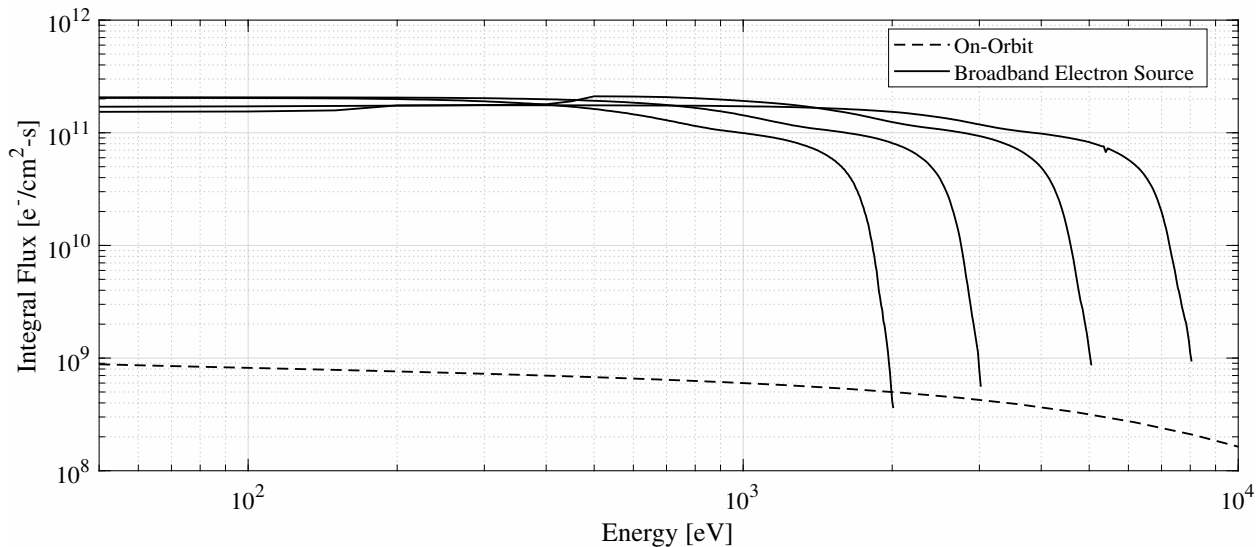
Figure 5.10: Example output spectra for maximum energies of 2, 3, 5 and 8 keV compared to on-orbit data from the LANL-MPA detectors at GEO.

maximum energies of 2, 3, 5, and 8 keV. The existing design is limited to a maximum energy of around 9 keV because the wires and resistors experience arcing at this voltage. The output fluxes are about two orders of magnitude higher than those experience in space. Work is ongoing to allow for tunability of the output fluxes to match a desired spectrum, either through decreasing the intensity of the VUV light or applying a coating to the aluminum stages to reduce photoemission.

5.4.3 Broad-Spectrum Electron Gun Beam Map

One shortcoming of the current design which only uses a single light source is that there is an uneven distribution of VUV light falling on the interior of the device. This causes more or fewer electrons to be generated at a given energy depending on the amount of light which falls on a given stage. Figure 5.11 shows an example differential flux spectrum for when the maximum voltage applied to the gun is 950 V. Due to the alignment between the VUV light source and the gun, most of the light falls on the rear stages, which is why there is a peak at 900 eV. The fluxes are lower in the 300-600 eV range, then there is a peak again at approximately 100 eV. This peak is caused by higher energy electrons from the rear stages impacting the front stages generating
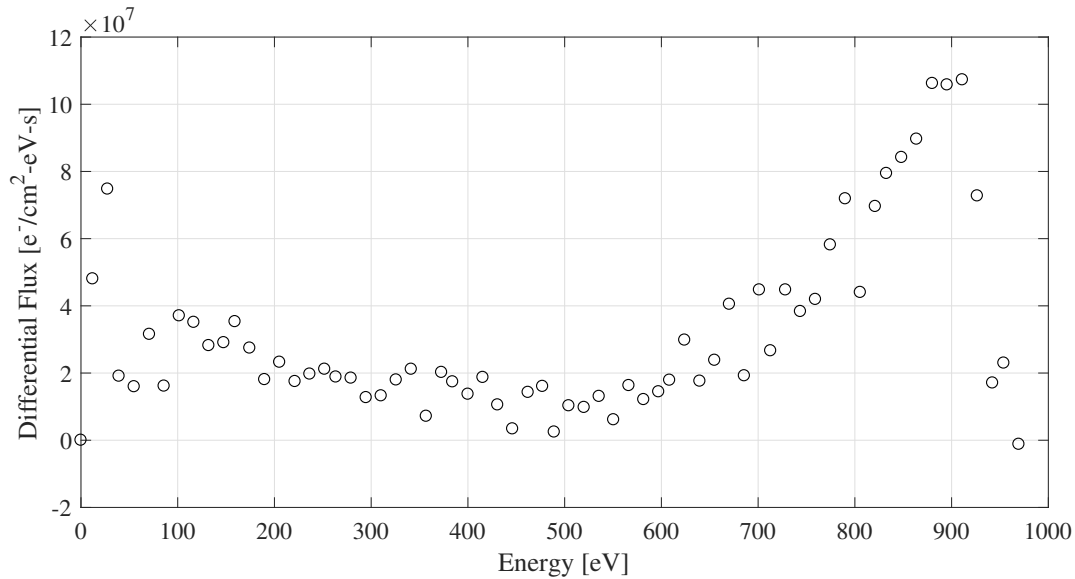
Figure 5.11: Beam map spectrum for a maximum energy of 950 eV and the RPA located directly beneath the gun.

secondary electrons from these stages.

A beam map was collected to determine the spatial flux and current distribution output from the gun. The RPA was mounted vertically on the motion system and the broad-spectrum gun was mounted above it. The RPA was swept across the beam and a spectrum like that shown in Figure 5.11 was collected at each position. Figure 5.12 shows a 1D beam map taken when the electron gun was set to output a maximum energy of 500 eV. Figure 5.13 shows a beam map for a maximum output energy of 950 eV. Overall, both plots show a beam spot size on the order of 2-3 cm though there is some energy-dependent focusing and spreading. Several interesting features are visible in the data. First, hot spots are present in both plots at approximately 90% of the maximum energy. The peak in the 500 eV spectrum is larger than that in the 950 eV. Medium energy electrons are deflected by 1-2 cm and so distributions are not centered about the zero position. Again, this is a consequence of only using a single light source which is directed at one side of the electron gun. This causes electrons to be emitted from the gun at an angle which depends on the electron energy.
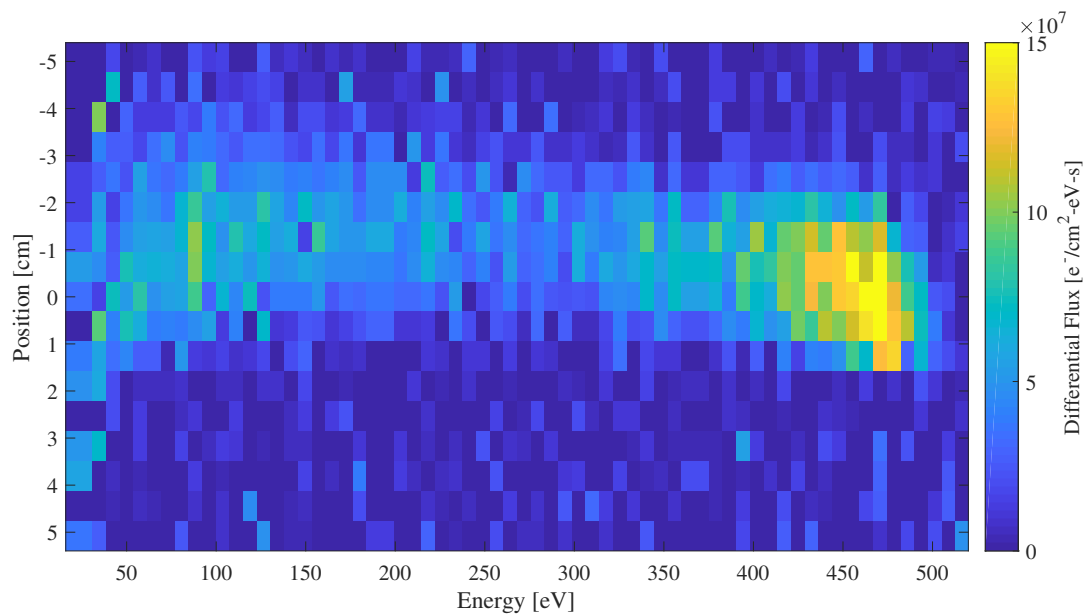
Figure 5.12: 1D beam map of the broad-spectrum electron gun when a maximum energy of 500 eV is output.
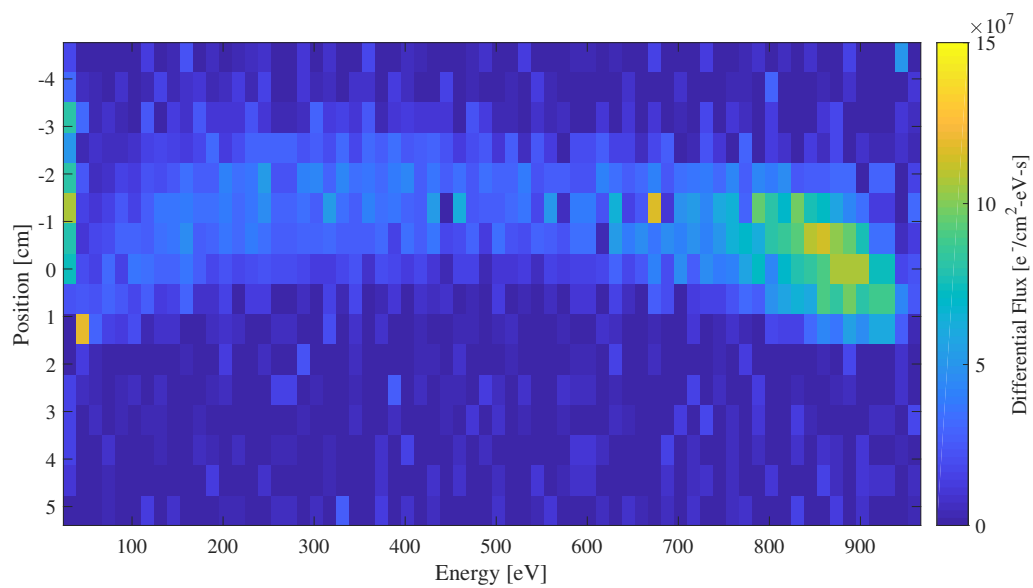
Figure 5.13: 1D beam map of the broad-spectrum electron gun when a maximum energy of 950 eV is output.

5.4.4   Experiments Using the Broad-Spectrum Electron Gun

To demonstrate the use of broad-spectrum electron fluxes for passive sensing, an experiment was conducted in which an aluminum plate was irradiated with the broad-spectrum electron gun. Figure 5.14 shows a picture of the experiment setup. The broad-spectrum source is located at left, the target plate is in the center, and the RPA is visible in the lower right. The experiment was configured such a way that the monoenergetic beam could also be turned on to irradiate the plate. A phosphor screen was mounted on the linear translation stage so that the locations and spot sizes of the electron beams could be checked. During data collection itself, the phosphor screen was translated out of the way. First, only the broad-spectrum gun was used to irradiate the plate and a spectrum was collected with the RPA. The plate was charged to -500 V and the broad-spectrum source was set to output a maximum energy of -1000 eV. Next, both the monoenergetic gun and the broad-spectrum source were used, with the monoenergetic gun set to emit a 3 keV beam at 10 µA. For comparison, the broad-spectrum source was turned off and only the monoenergetic source was used. Spectra for all three cases are shown in Figure 5.15.

Several interesting features are visible in the data. First, the plate potential is sensed accurately even when only the broad-spectrum gun is used. This clearly demonstrates how environmental plasma currents stimulate secondary electrons which can be used for sensing. Due to the large size of the broad-spectrum source and the limited diameter of the chamber, the broad-spectrum gun had to be placed very close to the plate (separated by approximately 2 cm). The electrons emitted from the broad-spectrum source were therefore only incident on the far left side of the plate. Because the RPA was located toward the right side of the chamber (as viewed in Figure 5.14), fewer secondaries generated from the broad-spectrum source make it to the RPA. Therefore, the current measured by the RPA when only the broad-spectrum source was operating is on the order of 0.5 nA. The potential of the plate is accurately measured, however, despite the relatively small signal. In contrast, the RPA measured a larger secondary electron current when only the monoenergetic beam was used. This is because the monoenergetic gun output a larger beam current than the

broad-spectrum beam, and the monoenergetic beam impacted the plate nearer the center where the secondaries were more likely to make it to the RPA. These results are specific to the experimental setup and gun settings. The signal from the broad-spectrum source would be substantially larger if the configuration allowed for the primary electrons to hit closer to the center of the plate. In all three cases, the sensed plate potential is slightly less than the actual plate potential, which is most likely a result of the electrons entering the RPA at an angle relative to the instrument axis. The results shown here demonstrate that broad-spectrum fluxes can be used to passively sense the potential of a target. Additionally, it shows that sensing with an electron beam in an environment

Figure 5.14: Setup for passive sensing experiment with the broad-spectrum electron gun. The broad-spectrum source is on the left, the target plate is at center, and the RPA is visible in the lower right.

with thermal plasma actually increases the secondary electron current which can be measured.

Environmental currents impact the sensing process in two ways. First, they interact with the target object and generate secondary electrons which can be used for sensing, as shown in Figure 5.15. Second, they add a background signal to the electron spectrum collected by the sensing craft. To demonstrate the target potential can be sensed even in the presence of background currents, the magnitudes of a background current and the signal current are compared in Figure 5.16. The red points in the figure are a spectrum taken when the broad-spectrum source was pointed directly at the RPA. As seen, there is a continuous spectrum of electrons from 0 to 1500 eV. The yellow points are from a test when an Inconel plate charged to -1000 V was irradiated with the VUV source and the subsequent photoelectrons were measured with the RPA. The blue points in the left panel show the photoelectron signal (yellow points) superimposed on the environmental background current (red points). This curve is differentiated to determine the electron energy distribution, which is shown in the right panel of the figure. The electron energy distribution is fitted with a two-term Gaussian, the peak of which clearly identifies the target plate potential. In this case, fitting with a single Gaussian does not accurately capture the electron population at -1000
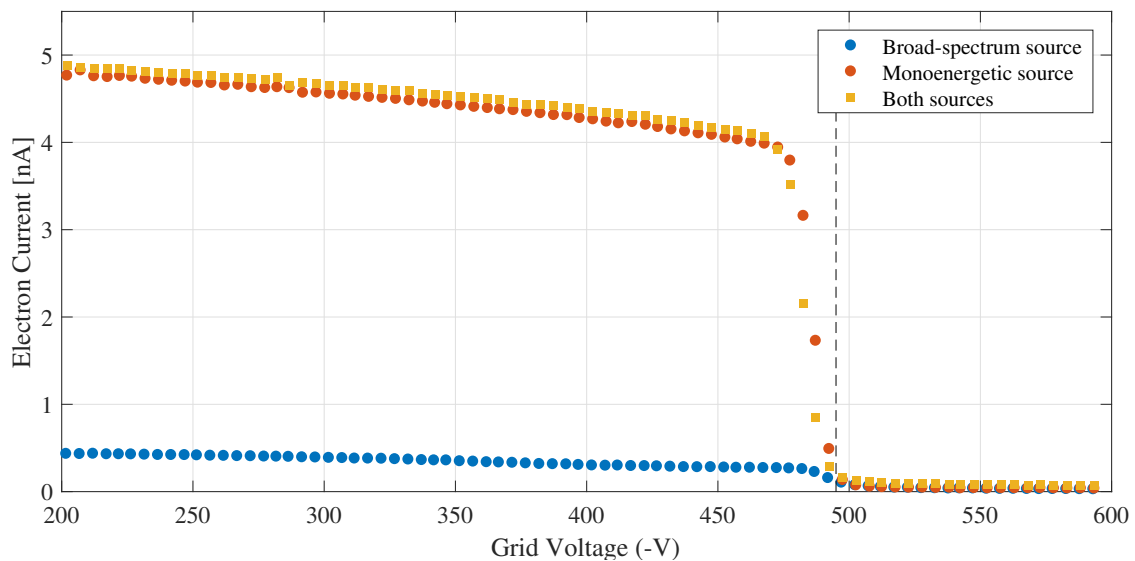
Figure 5.15: Comparison of spectra collected with the broad-spectrum electron source only, the monoenergetic source only, and both sources simultaneously.
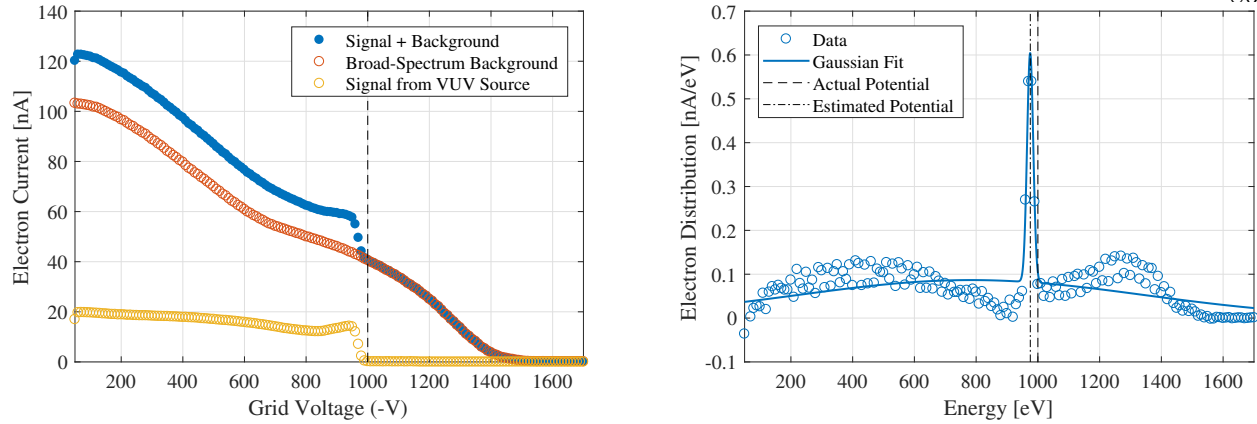
Figure 5.16: Example of target potential sensing in a broad-spectrum background. (Left) Comparison of photoelectron signal from an Inconel plate charged to -1000 V, broad-spectrum background, and photoelectron signal superimposed on the broad-spectrum background, and (right) electron energy distribution for the photoelectron signal superimposed on the broad-spectrum background.

eV, whereas the two-term Gaussian fit enables the target potential to be estimated accurately, despite the presence of the background fluxes. Even in the presence of ambient plasma currents, the potential of the target plate is accurately determined to within 2.6% error. This fact is further underscored by the fact that the output fluxes from the broad-spectrum source are significantly larger than the fluxes observed on-orbit, as previously discussed.

5.4.5   Other Applications for a Broad-Spectrum Electron Gun

This broad-spectrum electron experimental capability is not only important for demonstrating passive potential sensing, but also for a wide range of modern space environment topics including material degradation, spacecraft surface charging, and instrument calibration. In light of the expected broader impact of the broad-spectrum source, several key applications for the device are briefly discussed below.

Materials on the exterior of spacecraft are directly exposed to the space radiation environment. Long-term exposure to the energetic electrons in the space environment can cause degradation in the optical, structural, and electrical properties of surface materials. It is critically important that we understand the interactions between the environment and spacecraft to ensure the safe,

long-term operation of assets on-orbit. To this end, laboratory tests are frequently conducted in which materials are exposed to energetic electron beams to study on-orbit degradation. However, most charging and material degradation experiments conducted to date have either utilized a single, monoenergetic electron beam or a series of monoenergetic electron beams to simulate the full electron energy spectrum of space (e.g. [111, 39, 52, 108]). This approach requires simplifying assumptions about the electron radiation dose which are not representative of the actual space environment. Numerous studies show that the material degradation and charging/discharging characteristics depend on the energy of the incident electrons [78, 113, 45]. Furthermore, it has been established that exposing a material to a combination of two or three beams with different energies produces different charging/discharging behavior than exposing it to a single, monoenergetic beam [7, 120]. Another study shows that materials exposed to low energy (< 1 keV) electrons, which are commonly neglected in orbital flux and energy deposition models, exhibit changes that are a significant fraction of changes induced by orbital or higher energy exposures [28]. Currently, the best practice for recreating on-orbit damage in the laboratory is to expose test samples to a sequence of monoenergetic electron beams which approximate the dose-depth curve on-orbit [27, 67]. However, this process requires tests at numerous energies to approximate the on-orbit environment, which is expensive both in terms of time and cost. Another method to create a spectral electron environment involves passing energetic electrons through scattering foils of different thicknesses [2]. This method, which requires high-power accelerators, is experimentally complex and is not widely used [33]. Instead, monoenergetic beams or a sequence of monoenergetic beams are generally used. Therefore, it is questionable how well many laboratory tests represent what actually occurs on on-orbit, and it is highly desirable to be able to expose spacecraft materials and components to a broad-spectrum of electron energies in the laboratory. Clearly, the ability to produce orbital representative spectral electron environments in the laboratory is a critical need, not only for demonstrating the touchless sensing concept, but also for a wide range of experiments on spacecraft-plasma interactions. The broad-spectrum electron gun presented herein is a cost-effective and experimentally-tractable solution to meet this need.

5.4.6   Possible Improvements to the Broad-Spectrum Electron Gun

Work is ongoing to extend the maximum output energy of the device to the 30 keV and eventually to the 100 keV range, allowing for simulation of the space electron environment over five orders of magnitude in energy. Several other improvements are possible for future iterations of the broad-spectrum electron gun. First, the current version uses only a single ultraviolet light to stimulate photoemission on each stage within the device. This design produces a spectrum with a fixed shape (determined by how much light falls on each stage). By implementing numerous, smaller, dimmable ultraviolet sources along the length of the tube, future iterations will allow for arbitrary adjustment of the amount of light on each stage, which in turn allows for arbitrary adjustment of the output spectral shape. Figure 5.17 shows a schematic of this design. Additionally, the fixed resistors in between each stage could be replaced with digital potentiometers to allow users to adjust the width of each energy bin in the spectrum. Full feedback control of the spectrum could be achieved by using an energy analyzer at the output and then adjusting the intensity of each light or the potential gradient along the device to output a desired spectrum. Additionally, the acetal plastic insulators currently being used in between each stage will be replaced with ruby or sapphire spheres to prevent buildup of charge in the insulator stages. Finally, the design can be miniaturized and welded to a flange so it can be mounted on the exterior of a vacuum chamber.

An ideal broad-spectrum source would not have any energy-dependent spreading or focusing, which is present in the current design, as shown in Figures 5.12 and 5.13. Future work should consider optimizing the radius to length ratio to minimize energy-dependent structure in the beam spot. Stacking several broad-spectrum guns into an array may allow for a large beam spot size to be created and may help minimize the effects of energy-dependent spreading.

5.5   Results & Summary of Research Goal 4

Passive sensing of the unforced potential of a target has been considered. Passive sensing can be conducted using either photoelectrons emitted from a target in sunlight or secondary electrons
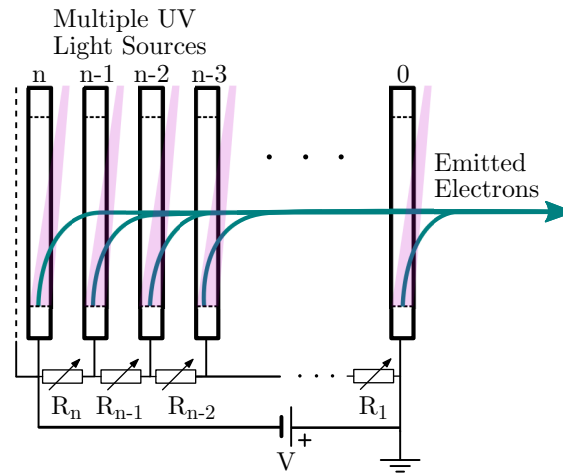
Figure 5.17: Future broad-spectrum electron gun design with multiple VUV light sources for full spectrum tunability.

generated by plasma currents interacting with a target. In sunlight, the photoelectron current typically dominates the other currents, so spacecraft most often charge slightly positive. Passive sensing is still possible in this case, though the sensing craft must be biased largely positive to extract some electrons from the potential well around the target. The photocurrent is reduced for targets which are highly reflective or are significantly self-shadowed which allows for negative charging. In these cases, photoelectrons are accelerated away from the target and can be measured by the sensing craft. Experiments have been conducted to demonstrate touchless sensing using photoelectrons. Additional experiments show that biasing the sensor craft positively increases the photoelectron current captured by the sensor.

Next, Nascap simulations are used to show that the natural secondary electron current emitted from a target is sufficient for sensing. This method is advantageous as it allows target potentials to be monitored in eclipse or when solar illumination angles are not favorable.

Particle fluxes in space are distributed across a wide range of energies, but most experiments use monoenergetic beams due to the lack of a tractable method for generating broad-spectrum fluxes in the laboratory. Both for the present research and numerous other topics in the field of spacecraft charging, there is a clear need for a broad-spectrum electron source. A novel technique

has been devised for generating a broad-spectrum electron beam and an advanced prototype has been built and characterized. This source has been used to demonstrate passive sensing using secondaries from ambient particle fluxes. In addition, the source is used to show that the electron population from a target can be identified even in the presence of background electron fluxes.

The results presented in this chapter show that the electron method can be used to passively sense the potential of a target. This means that touchless sensing can be used in a wide range of applications for which the natural potential of a target is to be measured. Additionally, the broad-spectrum electron gun is a major contribution to the field of spacecraft charging which will produce important results beyond this dissertation.

Chapter 6

Sensing of Spacecraft Shape Primitives and Differential Charging

6.1 Motivation & Background

Thus far, only target objects that are flat plates or spherical objects have been considered, as these simplified models have allowed for useful insight into the problem to be obtained. However, electrons emitted from a spacecraft are guided by the electric field, which is determined by the geometry and charge distribution of that spacecraft. Therefore, the shape and charge distribution of the target object plays an important role in the sensing process. The objective of this research goal is to extend the electron-based touchless potential sensing results to increasingly complex scenarios, specifically spacecraft with non-trivial shapes and heterogeneous potentials.

To understand the electric field near a charged object, consider the fields both at the surface and very far away from the surface. At the interface between a charged conductor at equilibrium (i.e., a conducting spacecraft surface) and free space, Faraday's Law and Gauss's Law can be used to determine the electric field. Figure 6.1 shows a boundary between a conductor and free space with example geometry relevant to application of these laws. For a system in equilibrium (with a static magnetic field), Faraday's Law states:

$$\oint_C \boldsymbol{E} \cdot \mathrm{d}\boldsymbol{l} = 0, \tag{6.1}$$

where $\boldsymbol{E}$ is the electric field and $\mathrm{d}\boldsymbol{l}$ is a differential line element of a closed circuit. Applying Equation 6.1 to the loop $abcda$ shown in Figure 6.1:

$$\oint_{abcda} \boldsymbol{E} \cdot \mathrm{d}\boldsymbol{l} = 0. \tag{6.2}$$
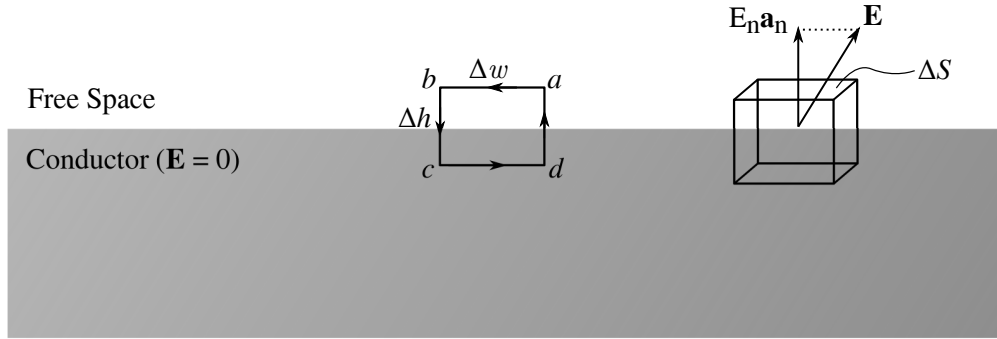
Figure 6.1: Boundary between a conductor and free space. Adapted from Reference [24].

Letting Δh go to zero, and noting that the electric field inside a conductor is always zero, the following is obtained:

$$E_t \Delta w = 0. \tag{6.3}$$

Thus, the component, E_t, of the electric field tangential to the surface of a conductor in equilibrium is always zero. Similarly, applying Gauss's Law to the Gaussian pillbox illustrated in Figure 6.1 gives:

$$\oint_S \boldsymbol{E} \cdot \mathrm{d}\boldsymbol{s} = \frac{Q}{\epsilon_0} = E_n \Delta S = \frac{\rho_S \Delta S}{\epsilon_0}, \tag{6.4}$$

where S is any closed surface, Q is the enclosed charge, ρ_S is the surface charge density on the conductor, and ϵ_0 is the permittivity of free space. Therefore, the boundary conditions on the surface of a conductor are:

$$E_t = 0 \tag{6.5}$$

$$E_n = \frac{\rho_S}{\epsilon_0}. \tag{6.6}$$

In other words, the electric field at the surface of a conductor in equilibrium must be entirely normal to the surface.

Simultaneously, it is known that the electric field from any given object tends toward that of a point charge at a sufficiently large distance. Thus, the electric field very close to the target spacecraft is everywhere normal to the spacecraft surfaces while the field at very far distances can be approximated by that of a point charge. At medium distances, the electric field is not

easily determined. Analytical expressions exist for fields around some objects, such as rings, disks, or planes; however, these expressions require assumptions that prevent them from being widely applicable. Complex shapes such as spacecraft require the use of numerical methods to determine the electric field at medium distances. The development and implementation of a numerical program for this purpose is discussed in the following section.

6.2   Extension of Simulation Framework for Arbitrary Geometries

The simulation framework introduced in Chapter 2 has been limited thus far to modeling electron trajectories around spheres. Here, the framework is extended so trajectories around any arbitrarily-shaped object can be modeled.

First, the geometry of the model object is either imported as an `.stl` file or defined in the MATLAB program. Delaunay triangulation is used to discretize the object into triangular elements [90]. Next, the Method of Moments (MoM) is used to compute the elastance matrix for the system, $\mathbf{S}$ [62]. MoM is based on the following equation for voltage:

$$V(\boldsymbol{r}) = \int \frac{\mathrm{d}q'}{4\pi\epsilon_0 |\boldsymbol{r} - \boldsymbol{r}'|}, \tag{6.7}$$

where $\mathrm{d}q'$ is a differential charge element located at point $\boldsymbol{r}'$ and V is the voltage due to that element observed at point $\boldsymbol{r}$. For a charged object discretized into N finite areas, the voltage is found by summing the integral over each area A_i that has a surface charge density σ_i:

$$V(\boldsymbol{r}) = \frac{1}{4\pi\epsilon_0} \sum_{i=1}^{N} \int_{A_i} \frac{\mathrm{d}A'}{|\boldsymbol{r} - \boldsymbol{r}'_i|} \sigma_i. \tag{6.8}$$

The voltage at the center of each discrete element is found by arranging Equation 6.8 into matrix form:

$$\begin{bmatrix} V_1 \\ V_2 \\ \vdots \\ V_N \end{bmatrix} = \frac{1}{4\pi\epsilon_0} \begin{bmatrix} \int_{A_1} \frac{\mathrm{d}A'}{A_1 |r_1 - r'|} & \cdots & \int_{A_N} \frac{\mathrm{d}A'}{A_N |r_1 - r'|} \\ \int_{A_1} \frac{\mathrm{d}A'}{A_1 |r_2 - r'|} & \cdots & \int_{A_N} \frac{\mathrm{d}A'}{A_N |r_2 - r'|} \\ \vdots & \ddots & \vdots \\ \int_{A_1} \frac{\mathrm{d}A'}{A_1 |r_N - r'|} & \cdots & \int_{A_N} \frac{\mathrm{d}A'}{A_N |r_N - r'|} \end{bmatrix} \begin{bmatrix} Q_1 \\ Q_2 \\ \vdots \\ Q_N \end{bmatrix}. \tag{6.9}$$

The $N \times N$ matrix is the elastance matrix, $\boldsymbol{S}$, which has units of F^{-1}. Given the Delaunay triangulation of the model, the elastance matrix is computed in the triangular basis using a routine developed by *Hughes and Schaub* [66]. Once the elastance matrix has been computed, voltages are assigned for each triangle element. In most cases, the entire object is assumed to be conducting, so all elements have the same voltage. For the case of differential charging, the triangle elements representing one spacecraft component (for example, a panel) all have the same voltage and all the elements representing a different component (for example, the spacecraft bus) have a different voltage (assuming the spacecraft is made of conducting elements). Given the elastance matrix and the voltages, the charge on each triangle element can then be computed:

$$\boldsymbol{Q} = \boldsymbol{S}^{-1}\boldsymbol{V}, \tag{6.10}$$

where $\boldsymbol{Q}$ is an $N \times 1$ vector which contains the total charge on each triangle element in C and $\boldsymbol{V}$ is the $N \times 1$ vector describing the voltage on each element in V.

Now, given the location and charge of each triangle, the electric field can be determined by summing the contribution of the integral over each triangle:

$$\boldsymbol{E}(\boldsymbol{r}) = \frac{1}{4\pi\epsilon_0} \sum_{i=1}^{N} \int_{A_i} \frac{\sigma_i(\boldsymbol{r} - \boldsymbol{r}'_i)}{|\boldsymbol{r} - \boldsymbol{r}'_i|^3} \, \mathrm{d}A'. \tag{6.11}$$

This step is also computed numerically using an algorithm from Reference [66]. Note that this approach requires integrating over each triangular element, then summing all of the integrals together to find the electric field at a given point.

The MoM formulation provides a high-fidelity model but is relatively slow because it requires a computationally expensive integral for each triangular element. However, at a sufficiently large distance away, the difference between the electric field from the triangle and the electric field from a representative point charge in the same place is negligible. The electric field of a point charge has a simple analytical form, so the expensive numerical integrals can be avoided. Therefore, a hybrid method is developed in which the full MoM integral is used for the contribution from nearby elements, whereas the point charge approximation is used to determine the contribution

from far away elements. The next section addresses the question: how far is sufficiently far for the point charge approximation to be applied? Note that the point charge approximation is based on the Multi-Sphere Method (MSM), in which a spacecraft is modeled as a collection of finite-radius spheres [104, 105]. The primary difference between MSM and the point-charge approximation is that MSM uses spheres with non-zero radius, so it can accurately model the capacitance of a spacecraft. In the present case, there is no need to consider capacitance, thus the point-charge model is sufficient. The point-charge approach is faster than heterogeneous MSM approaches [66] because it does not require additional calculations to determine the appropriate size of each sphere.

Figure 6.2 shows a model spacecraft represented as MoM triangular elements, a collection of point-charges, and as a hybrid of triangles and points. For the hybrid example, the point (X,Y,Z) = (0.5, 0, 0.5) m is taken as an example measurement point. The elements in the immediate vicinity of the measurement point are modeled as triangles, whereas elements beyond a threshold distance are modeled as point charges.

The distance from a given triangle where the point charge approximation is sufficiently accurate depends on the charge and size of the triangle. To determine this distance, a single triangular element is considered. The triangle voltage is varied from -100 V to -15 kV and the size of the triangle is varied from 0.005 to 0.5 m. The electric field at 10000 points near the triangle is computed at every voltage and size using both the full MoM and the point charge. Then, the distance is found such that each component of the MoM electric field and point charge field match to $< 0.1 \mathrm{~V\,m^{-1}}$. Percent difference is not well defined because both fields are converging to zero as a function of increasing distance, so absolute difference is used instead. A threshold error of $0.1 \mathrm{~V\,m^{-1}}$ is selected because, in most cases of interest, the target object is charged to several hundred volts. Assume, for example, there is a potential difference of 500 V between two craft with a separation distance of 10 m. This gives an electric field between the objects of $50 \mathrm{~V\,m^{-1}}$. Thus, a difference in electric field of $0.1 \mathrm{~V\,m^{-1}}$ represents an error of 0.2%. For larger voltages or smaller separation distances, the error decreases.

Figure 6.3 shows an example of the differences between the MoM and point charge at 10000
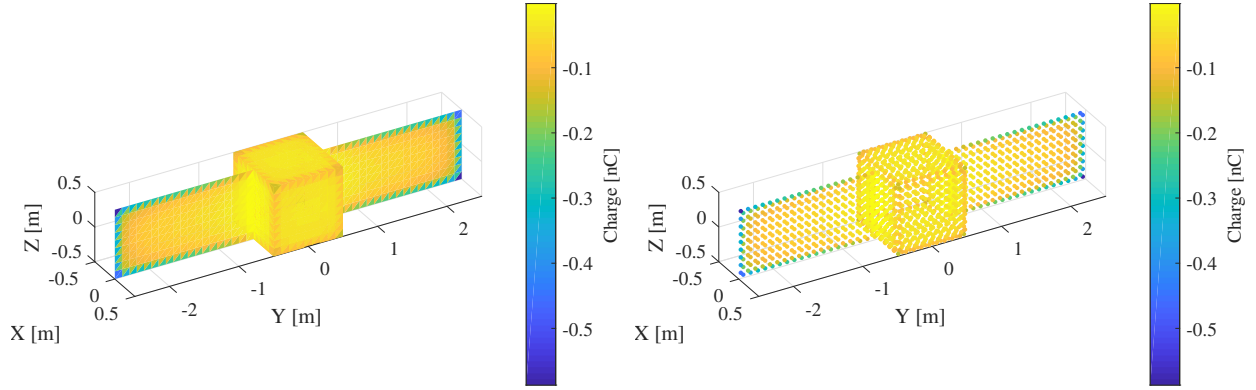
(a) Method of Moments model.

(b) Point charge model.
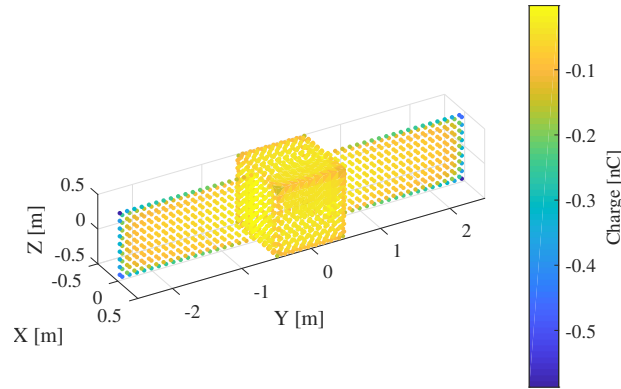
(c) Hybrid MoM-point charge model.

Figure 6.2: Various electrostatic models of a spacecraft.

points around a 1 cm triangular element at -1000 V. The electric field of the triangle and the representative point charge match to within $0.1 \mathrm{~V\,m}^{-1}$ at a distance of 0.1363 m away (denoted by the black lines). This same process is repeated for the other triangle sizes and charge densities to determine the error threshold distance as a function of both the triangle element size and charge.

A 2-dimensional polynomial with the following form is fit to these data points:

$$d = p_{00} + p_{01}L + p_{10}Q + p_{20}L^2 + p_{11}LQ + p_{02}Q^2, \tag{6.12}$$

where d is the error threshold distance, Q is the charge on the triangle, L is the length of one
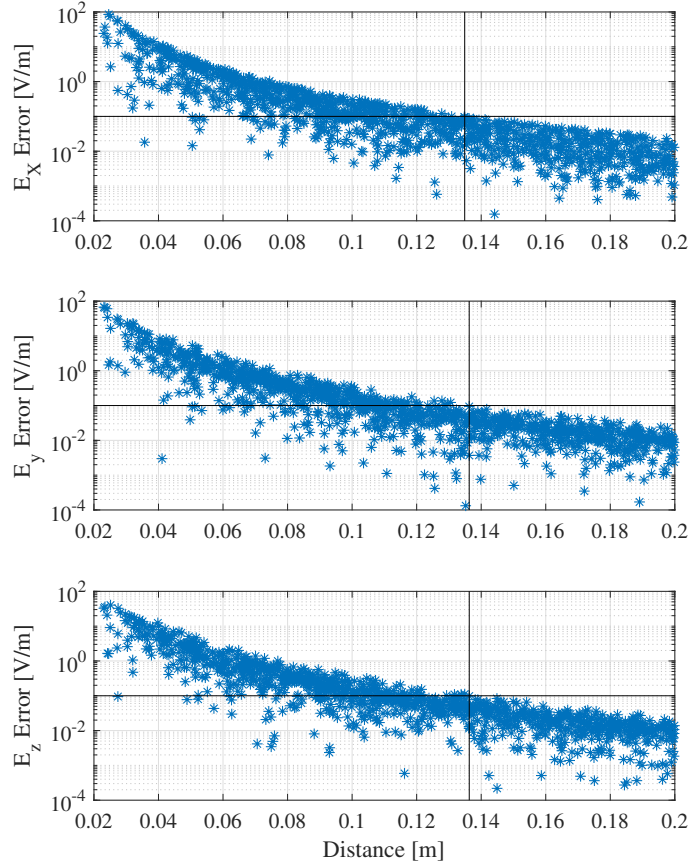
Figure 6.3: Difference between MoM and point charge electric fields for 10000 points around a triangular element.

side of the triangle, and p_{xx} are fitting parameters. Figure 6.4 shows the data points and the fit function, which has an R-squared value of 0.9941. In all simulations presented in this work, MoM is used to find the contribution to the total electric field from triangles less than a distance d away, and all triangles more than a distance d away are approximated as point charges. This hybrid MoM-point charge method provides a computationally-efficient simulation framework with the near-surface accuracy of MOM and sufficient speed to simulate large numbers of electrons.

Table 6.1: Fitting Parameters for Equation 6.12

p_{00}	p_{01}	p_{10}	p_{20}	p_{11}	p_{02}
0.08025	6.049	-43.58	-4.2	-20.66	-336.8
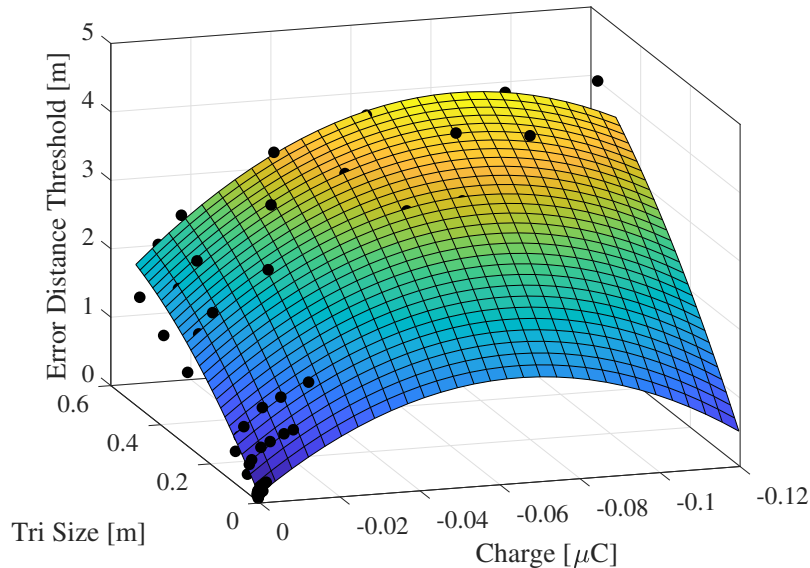
Figure 6.4: Threshold distance at which the point charge approximation of a triangular element matches the MOM electric field from that element to within 0.1 V m^{-1}.

6.3 Spacecraft Shape Primitives

6.3.1 Experiment and Simulation Comparison

Experiments are conducted to measure currents around non-trivially shaped objects, and the experimental results are directly compared to numerical results, which serves to validate the simulations. Once agreement has been demonstrated between experiments and simulations, the simulations can then be used to investigate target objects which are not possible to test in the vacuum chamber (for example, larger spacecraft models at higher voltages).

A corner bracket is selected as a test shape because it contains several features which are relevant to spacecraft shapes. It has an exterior corner, which is similar to a box-shaped spacecraft bus. It contains an interior corner similar to a joint between a solar panel and a bus. Finally, edge effects, similar to looking at a solar panel edge-on, are also captured. An aluminum $90°$ corner bracket 30.48 cm tall with sides 7.62 cm long was used as a target. As received, the bracket was very shiny and the aluminum had ink printed on it in several places. Photoemission is small for highly reflective surfaces and also depends strongly on the presence of contaminants on the surface.
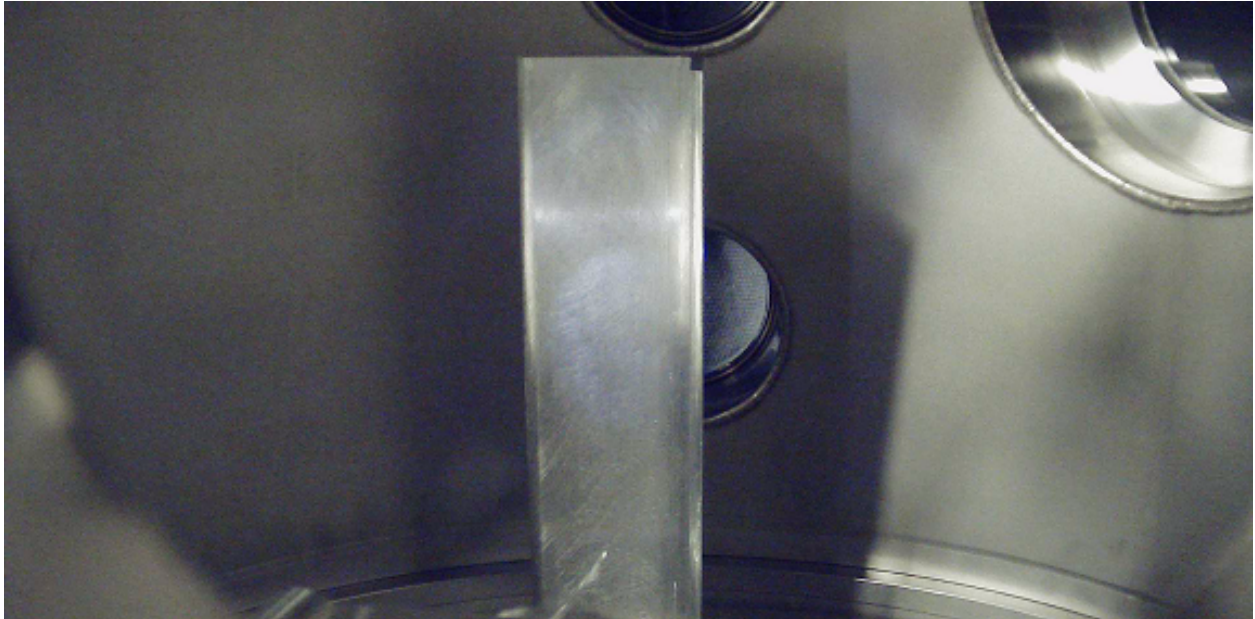
Figure 6.5: Aluminum bracket in the vacuum chamber illuminated by the VUV light. The circular outline of the VUV light is faintly visible on the bracket.

Therefore, the bracket was manually sanded with sandpaper then cleaned with isopropyl alcohol prior to being installed in the chamber. The bracket was mounted on the rotary stage in the vacuum chamber, but electrically isolated from the stage. The bracket was held at -500 V and was exposed to VUV light to stimulate photoemission. Figure 6.5 shows the bracket in the vacuum chamber. The circle of VUV light is visible on the center of the bracket. The RPA, located 30 cm from the target, was used to measure the electron current as the bracket was rotated. Vacuum chamber pressures during the experiment were on the order of 1 μTorr.

Figure 6.6 shows the MoM model of the bracket which contains 864 triangular elements. The location of the RPA relative to the bracket is denoted by the black box. The charge on the bracket distributes such that the greatest charge is along the edges and at sharp corners. To simulate the emission of electrons from the bracket, particles are given initial conditions along the sides of the bracket in the $Z = 0$ plane. 800 total particles are simulated, with 200 along each of the four sides. Figure 6.7 shows the particle trajectories in the $Z = 0$ plane. The particles are generated with equal spacing along each edge, so the relative density of the particle trajectories (black lines) is
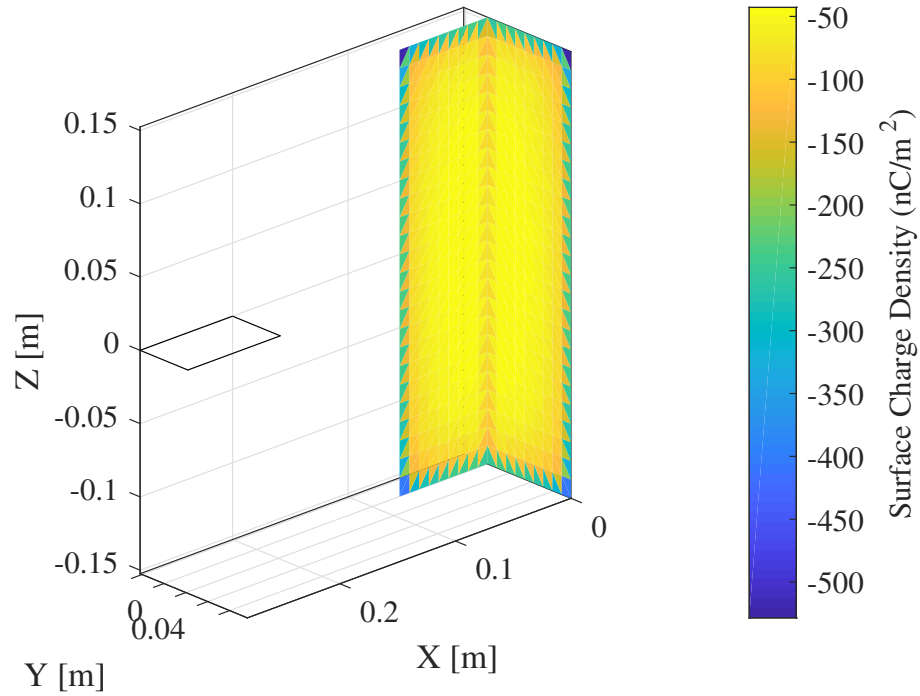
Figure 6.6: MoM model of corner bracket. The black outline indicates the size and relative position of the RPA in the experiment.

representative of what current would be measured by a sensor in a given location. A simulated sensor with the same dimensions as the RPA is swept around the bracket and the number of particles which enter the detector are counted at each angle step. In the experiment, the current is directly measured in nA, however, the simulated signal is in number of particles captured. To allow for direct comparison between simulated and experimentally measured signal, the simulated signal is scaled using a least-squares approach so both signals can be compared in nA. Comparison between the simulated and experimentally measured signal is shown in Figure 6.8. The zero angle is defined by the dashed line and arrow in Figure 6.7 .

It is clear that no particles are emitted in the edge-on directions (at angles of 0 and 90°). The electric field very close to the bracket surface is everywhere normal to the bracket, so the electric field near the edges changes very quickly from one side of the bracket to the other. Thus, a very small region in initial location maps to large differences in final location which causes the spreading
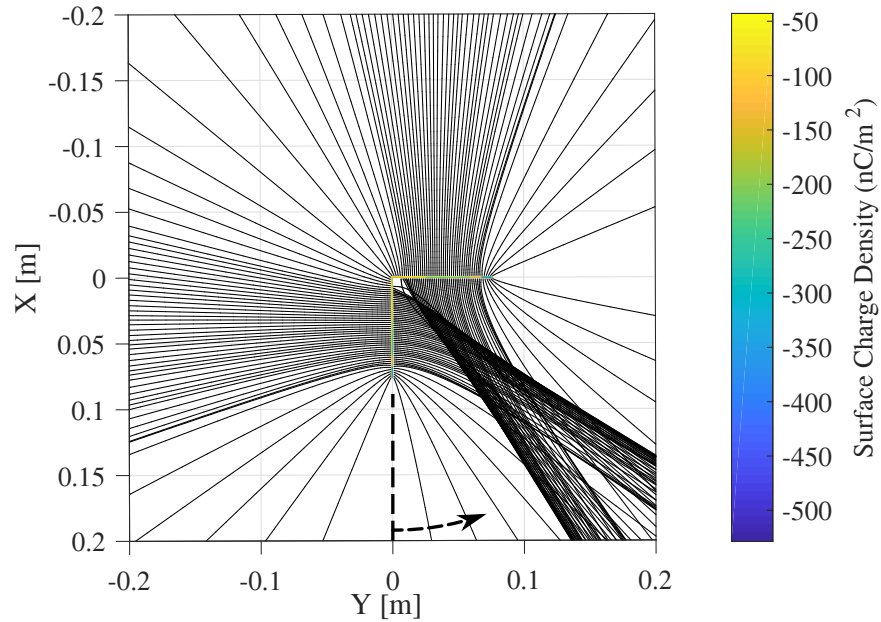
Figure 6.7: Simulation of electrons emitted from bracket. The dashed line and arrow at the bottom of the figure define the angle referred to in Figure 6.8.
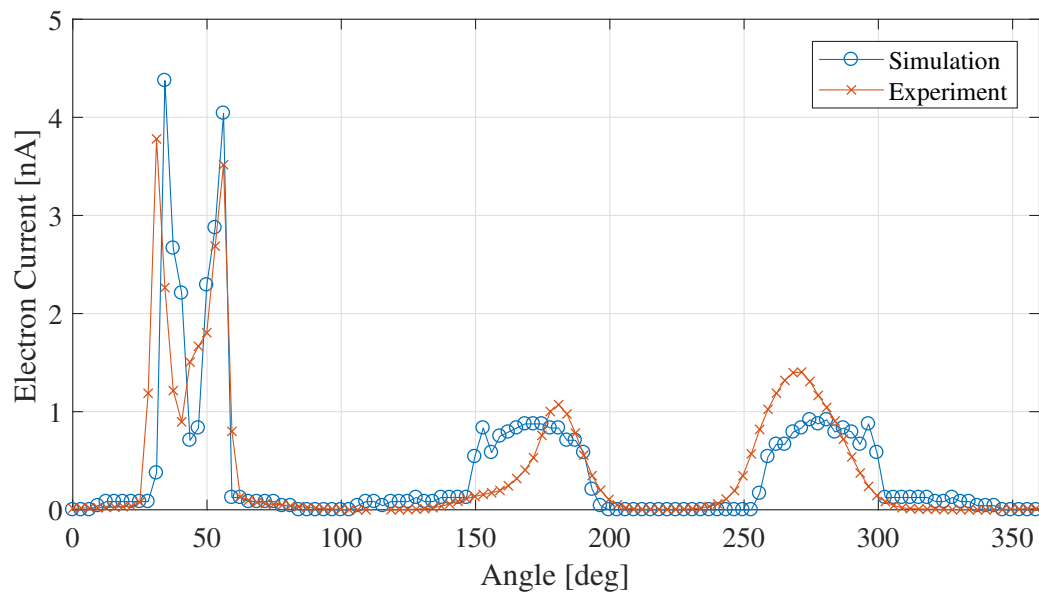
Figure 6.8: Comparison of experimentally-measured and simulated signal emitted from rotating bracket.

and decrease in signal. The interior corner acts as a lens which focuses the particles generated on

those faces into two beams directed at an angle near 45°. There is a double-peak structure present as the trajectories of particles from the interior faces cross and diverge. The double peak structure is captured well by both the simulation and experiment results. At 180 and 270°, there is a signal increase due to particles emitted from the flat, exterior sides of the bracket. There is a difference of approximately 26% in signal magnitude between the experimentally-measured peaks at these locations. Ideally, both sides of the bracket are identical, so the peaks should also be identical. The VUV light has an output stability better than 1%, so any significant changes in the source can be ruled out. One likely explanation for the discrepancy is differences in the surface condition of each side. The bracket was sanded manually, and it is known that variations in surface roughness or the presence of contaminants cause variations in the photoelectron yield [43]. Repetition of the experiment using more precise surface preparation and characterization methods may result in improved agreement between the simulation and experiment in the regions around 180 and 270°. The objective of this experiment, however, is to demonstrate that the numerical models capture the physics of electron emission from charged, spacecraft-representative shapes. The simulation and experiment agree sufficiently well for the simulations to be considered validated.

6.3.2   Spacecraft Models

The numerical simulations are now used to consider electron emission from a variety of representative spacecraft models. Only the planar case is considered here, so all electrons are generated in the $Z = 0$ plane. This assumption allows for analytical understanding of the effect of spacecraft geometry to be obtained, which can then be extended to 3D. Similarly, initial energy and angle distributions of secondaries and photoelectrons are neglected here (particles are generated on the surfaces with zero initial energy), as this allows the effects of the spacecraft geometry to be investigated more clearly. First, a spacecraft consisting of a box with two identical solar panels is modeled. The entire spacecraft is assumed to be electrically conducting, in accordance with satellite design recommendations [92, 48]. Figure 6.9 shows an MoM model of the box-and-panel spacecraft along with electron trajectories emitted from every surface. Again, particles are generated with

(a) Spacecraft model.

(b) Trajectories of electrons emitted from spacecraft.
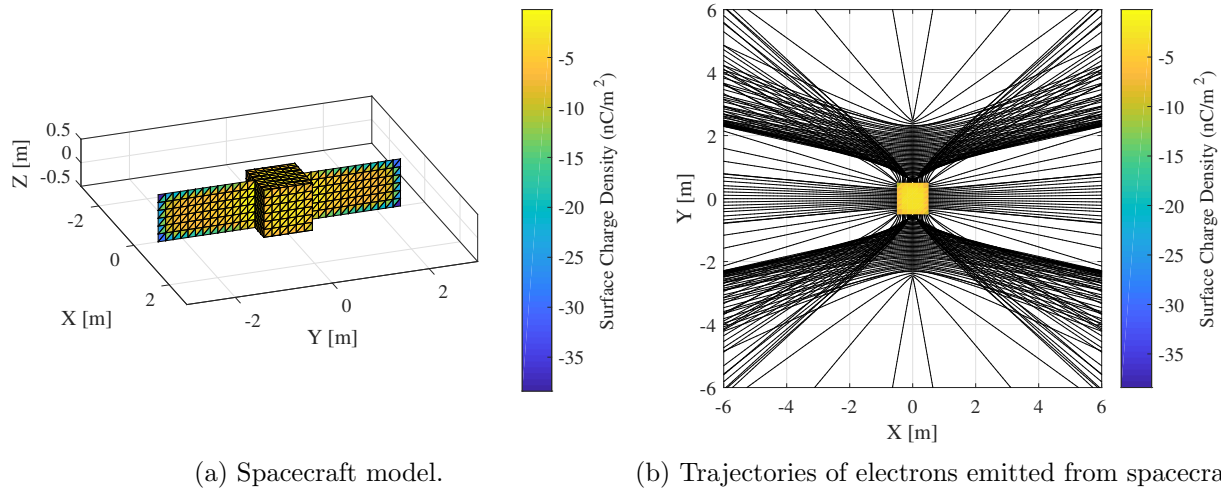
Figure 6.9: Box spacecraft with two solar panels.

equal spacing, so the density of trajectories in a given area is representative of signal strength.

Several key trends are visible in Figure 6.9b. Flat surfaces, such as the sides of the box or the solar panels, produce electron signals which should be sufficiently large to measure. Interior corners serve to focus the electron signal, whereas zero signal is observed when viewing a panel edge on. In this case, the spreading effect which is expected at the corners of the box is dominated by the focusing effect from the box-panel joint. Figure 6.10 shows the trajectories for particles emitted by a cylindrical spacecraft with two solar panels. The resulting pattern is very similar to the box, except that there is a spreading effect around the Y = 0 axis. The curved surface of the cylinder causes the particles to diverge more in this region compared to the flat surface of the box. Next, a parabolic dish is modeled, as shown in Figure 6.11. The geometry of the dish focuses the particles generated on the concave side into a beam, whereas those on the convex side are spread out over a wide area. Depending on the absolute signal magnitude (the lines in Figure 6.11b only indicate regions relative signal increase), as well as the capabilities of a given sensing craft, either of these cases may be advantageous. If a sensor is capable of measuring the signal emitted from the convex side of the dish, the signal is available for a much larger region. Thus, the potential of the dish could be measured for a longer period of time if the dish was tumbling in space. On

(a) Spacecraft model.

(b) Trajectories of electrons emitted from spacecraft.
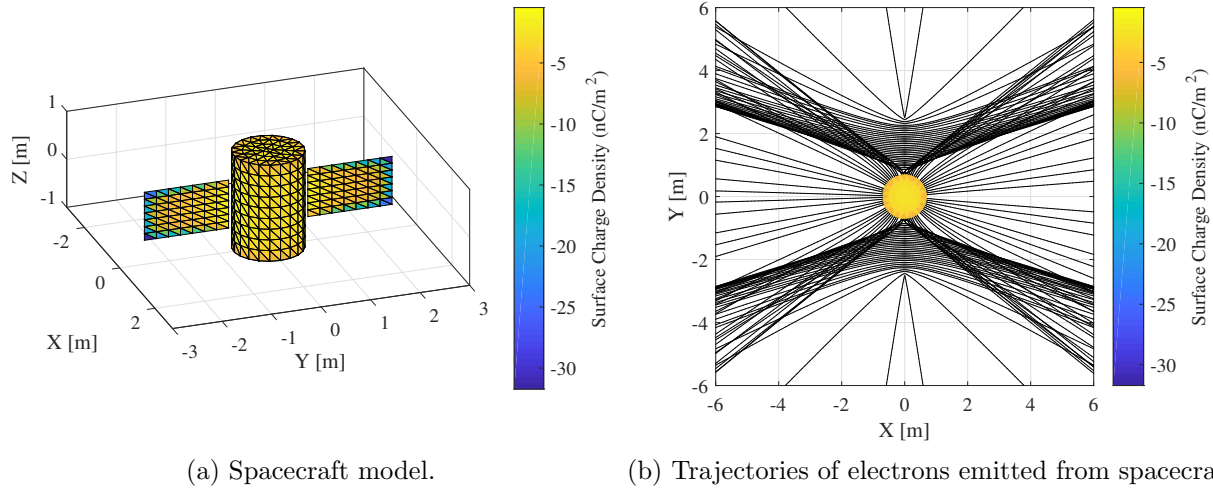
Figure 6.10: Cylindrical spacecraft with two solar panels.

(a) Parabolic dish model.

(b) Trajectories of electrons emitted from parabolic dish.
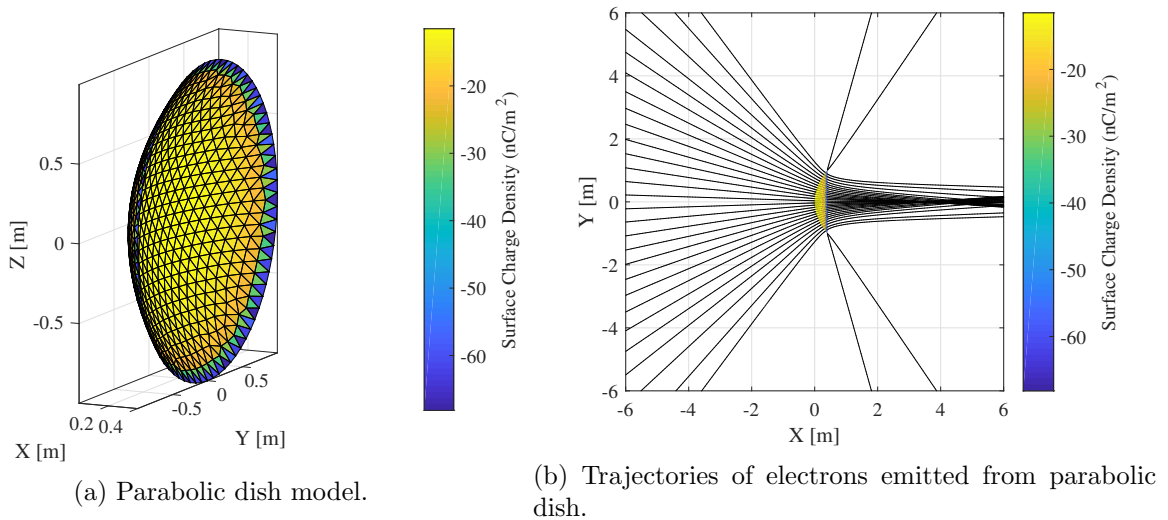
Figure 6.11: Parabolic dish antenna.

the other hand, the signal emitted from the concave side is larger, which would produce a larger signal-to-noise ratio and perhaps a higher confidence measurement of the potential. However, this signal would only be available during limited windows of time in a situation with relative motion between the sensor and target.

Finally, a box spacecraft with an antenna dish is modeled, as shown in Figure 6.12. The

(a) Spacecraft model.

(b) Trajectories of electrons emitted from spacecraft.
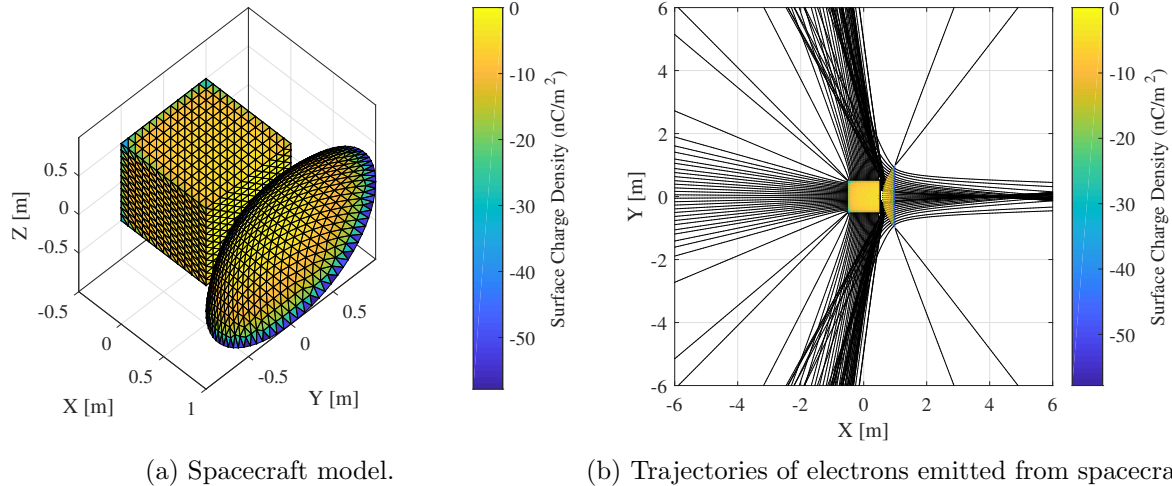
Figure 6.12: Box spacecraft with a parabolic dish antenna.

highest signal regions come from the interior corners where the box and dish are joined, as well as the concave surface of the dish. The lowest signal magnitudes are emitted from the corners of the box and from the edges of the dish.

The following insights are obtained:

(1) There always exists some point on the target spacecraft for which electrons map back to the servicing spacecraft. However, this area may be very small and the resultant signal may be very difficult to measure. A trade-off exists between the capability of a detector and the regions over which measurement of target potential is possible.

(2) Regions of low signal include convex surfaces such as exterior corners and edges. The sharper the corner or edge, the greater the spreading effect of the electron signal emitted from that location. For example, a very small signal is obtained by looking at a panel edge on. The signal from a curved surface (such as a cylinder) is greater than that from a hard corner (such as that of a box).

(3) Concave surfaces such as interior corners focus particles from different surfaces into the same direction in space. This produces large signals, but over limited spatial regions.

6.4   Differential Charging

Spacecraft design best practices recommend all exterior surface be connected to a common ground to prevent differential charging which can result in hazardous arcing [48, 92]. Despite this recommendation, numerous spacecraft are known to become differentially charged and experience arcing (e.g. [40]). This presents an interesting case for touchless sensing because there is not just one target potential to be measured, and the electric fields from differentially-charged spacecraft components may guide the electrons in unexpected directions. To investigate touchless sensing of differentially-charged spacecraft, two side-by-side plates at different potentials are considered.

Figure 6.13 shows results from a simulation for particles emitted from two differentially charged plates. The plate on the left is charged to -1000 V and the plate on the right is charged to -500 V. Particles emitted from the left plate (thus having energies of 1000 eV) are plotted in blue, and those from the right plate (with energies of 500 eV) are plotted in red. Several interesting features are visible in the simulation results. First, the charge density on the inner side of the right-hand plate is positive, even though the plate is held at a negative potential. The close proximity to the -1000 V plate forces the negative charges to the outside edge, creating a positive charge distribution on the inside edge. The charge distribution of the -1000 V plate is not significantly affected by the presence of the -500 V plate on the right. Similarly, the higher energy population of electrons emitted from the left plate (blue lines) is not affected by the electric field from the right plate. Conversely, the electrons emitted from the right plate (red lines) are steered significantly in the +Y direction. In fact, particles generated very close to the inner edge of the -500 V plate are unable to overcome the potential barrier imposed by the -1000 V plate and do not escape at all. For a sensor located at a -Y coordinate, only the potential of the left plate would be sensed because no electrons from the right plate travel in the -Y direction. For a sensor located at a +Y coordinate, both the 1000 eV and 500 eV populations could be observed, so the potentials of both plates can be sensed. A sensor sweeping around these two targets would be able to determine which potential is on which plate.   To confirm this hypothesis, an experiment was conducted in which two aluminum
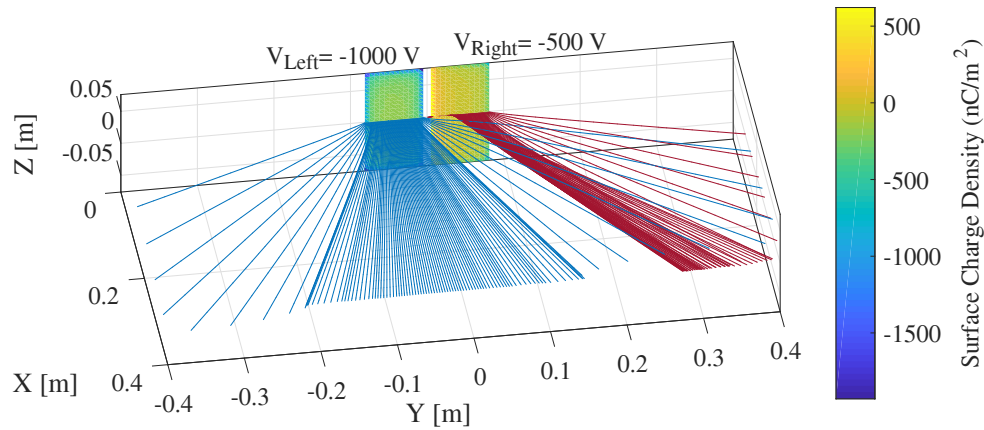
Figure 6.13: Simulation of electrons emitted from differentially-charged plates. Blue lines indicate particles originating from the left plate, whereas red lines indicate particles originating from the right plate.
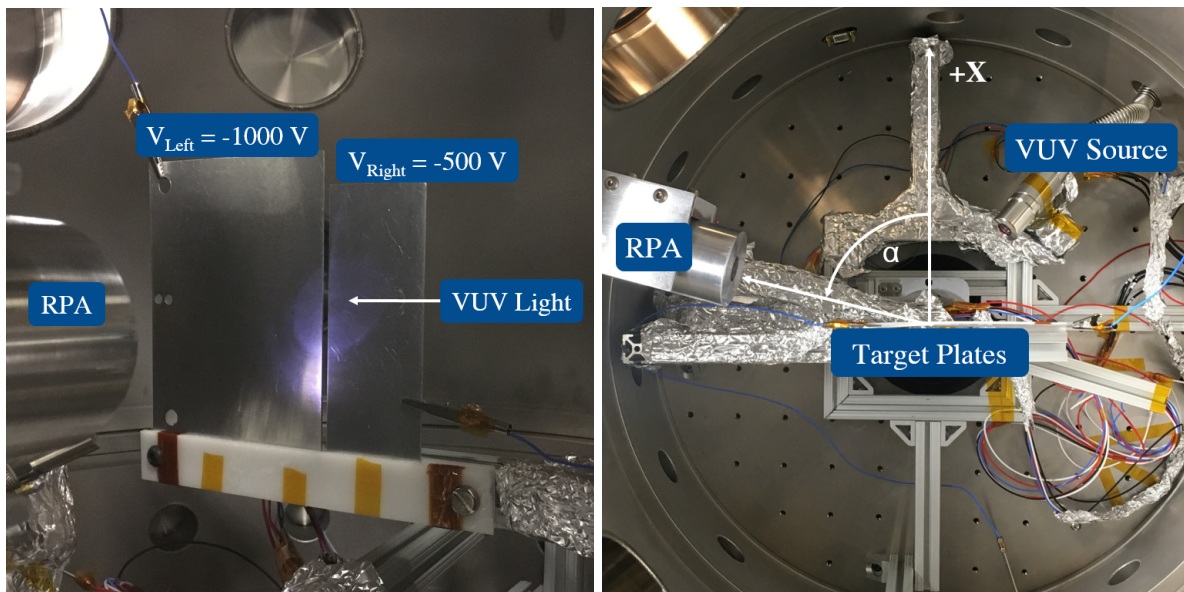
(a) View of target plates.

(b) Top view of experimental setup.

Figure 6.14: Experiment apparatus to test sensing of differentially-charged targets

plates were placed side-by-side in the vacuum chamber and charged to different potentials. The plates were then illuminated with the VUV light to stimulate photoemission. The plates were kept in place with the RPA mounted on a rotating arm and swept around the target. Figure 6.14 shows a picture of the experimental setup. The RPA angle α is defined relative to the +X axis as given
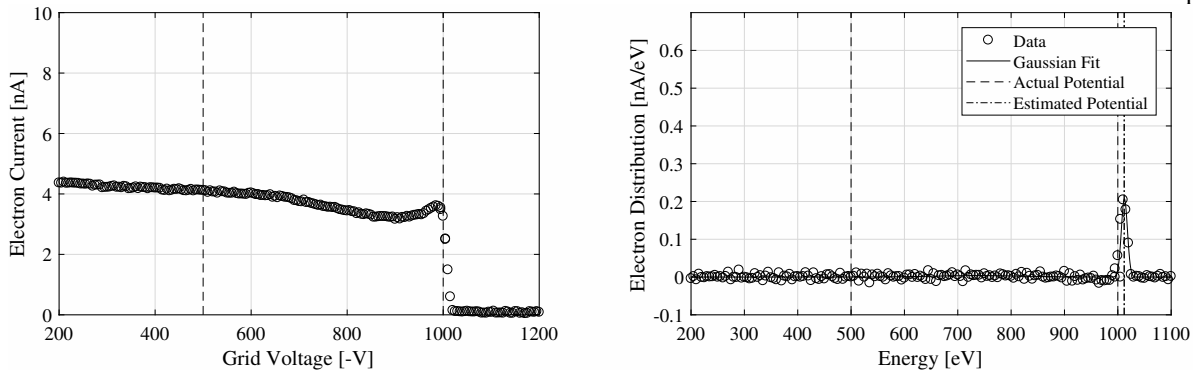
Figure 6.15: Spectra of electrons emitted from differentially charged plates taken with the RPA located at an angle of 30°.
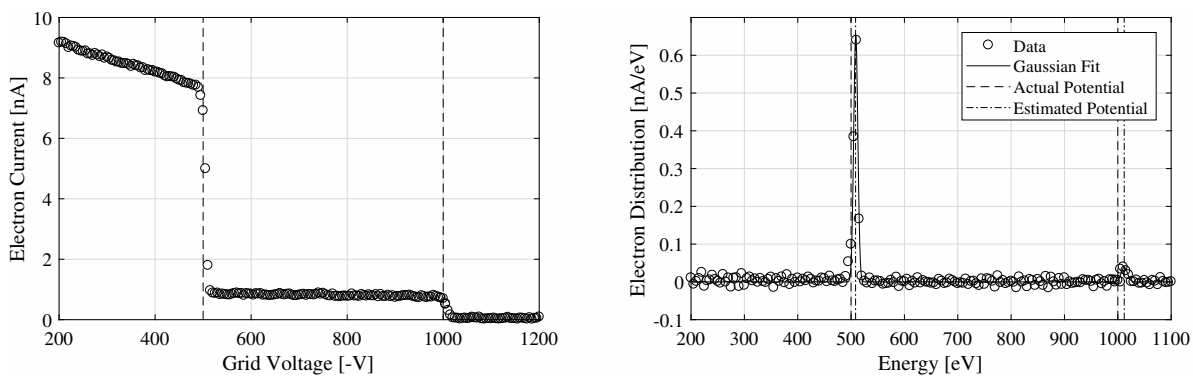
Figure 6.16: Spectra of electrons emitted from differentially charged plates taken with the RPA located at an angle of 50°.

in Figure 6.14b. Figure 6.15 shows a spectra taken by the RPA when it was located at an angle of 30°. At this angle, only the 1000 eV population is observed. This is consistent with the simulation results shown in Figure 6.13 which shows the particles from the -500 V plate being steered in the +Y direction. Figure 6.16 shows a spectra taken with the RPA at an angle of 50°. At this location, both the 500 and 1000 eV populations are observed, indicating that a single spectra can be used to determine multiple potentials on a target object. At this angle, the 500 eV peak is significantly larger than the 1000 eV, which is also consistent with the simulations.

The agreement between experimental and numerical results demonstrate that touchless sensing is feasible for differentially-charged target objects. However, the complex electric fields near such targets affect the spatial locations at which one or both potentials can be measured. Several

factors should be considered when extending these results to the spacecraft-scale. It is apparent that the magnitude of voltage difference between two components plays an important role. For example, the sensing effects of two components charged 50 V different are much less than those of two components charged 5 kV different. The relative sizes of the differentially-charged components being sensed are also important. For example, if an entire solar panel is floating at a different potential from a spacecraft bus, the sensing process is substantially affected. Conversely, if a single cell on the solar panel is floating at a different potential from the rest of the panel, the effects on the sensing process may be small.

To illustrate this effect, a simulation is conducted for a differentially-charged box-and-panel spacecraft model, in which the box is charged to -1000 V and the panel is charged to -600 V. The MoM model for the differentially-charged craft is shown in Figure 6.17a, and the trajectories of electrons emitted from the craft are shown in Figure 6.17b. For comparison, the electrostatic model and trajectories for a spacecraft of the same shape but homogeneously-charged to -1000 V are shown in Figure 6.18. To aid in understanding the trajectories, particles originating on the box are plotted in red, whereas those originating on the panel are plotted in blue. In the homogeneous case, the electrons emitted from the right side of the box are significantly deflected away from the panel. Similarly, those emitted from the panel are also deflected away from the box. In the differential-charging case, however, the electrons emitted from right side of the more negatively-charged box are only slightly perturbed by the presence of the panel. As a result, the population of electrons emitted from the box is visible in a larger spatial region, specifically near the panel edge, than compared the homogeneous-charging case. Those emitted from the panel however, are strongly steered away in the positive Y direction due to the electric field of the box. The electrostatic models show that when the panel is differentially-charged relative to the box, a positive charge resides on the leftward side of the panel. As a result, electrons originating on the left side of the panel are unable to escape from the surface. Once again, the relative location of the sensing craft determines which electron population is measurable. In the differential-charging case, the 600 eV population from the panel is present only in narrower spatial region than the

(a) Charge distribution on a differentially-charged spacecraft.

(b) Trajectories of electrons emitted from differentially-charged spacecraft.
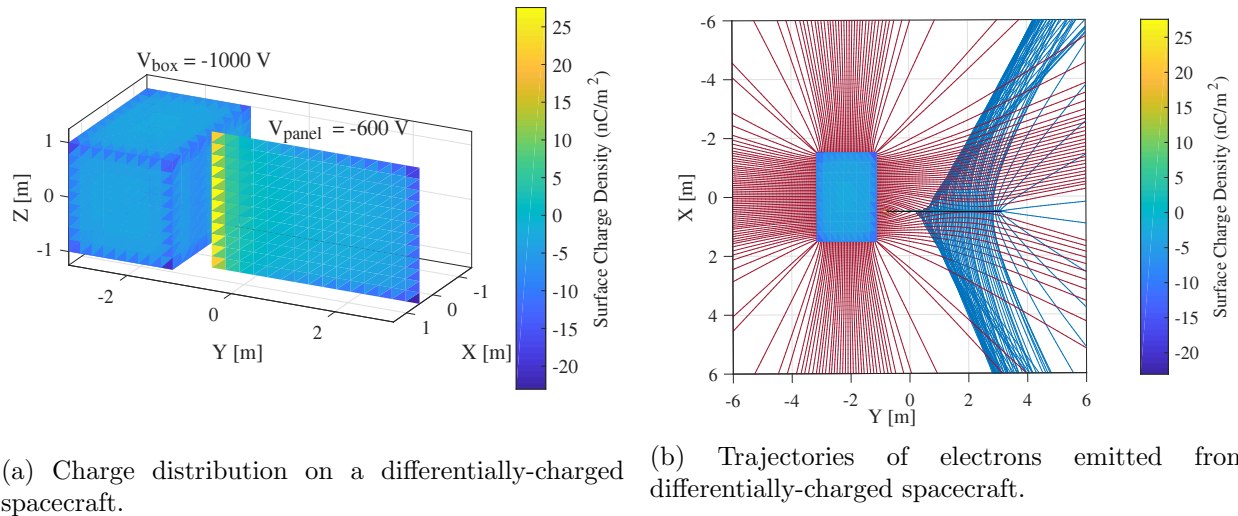
Figure 6.17: Differentially-charged spacecraft in which the box is charged to -1000 V and the panel is charged to -600 V.

(a) Charge distribution on a homogeneously-charged spacecraft.

(b) Trajectories of electrons emitted from homogeneously-charged spacecraft.
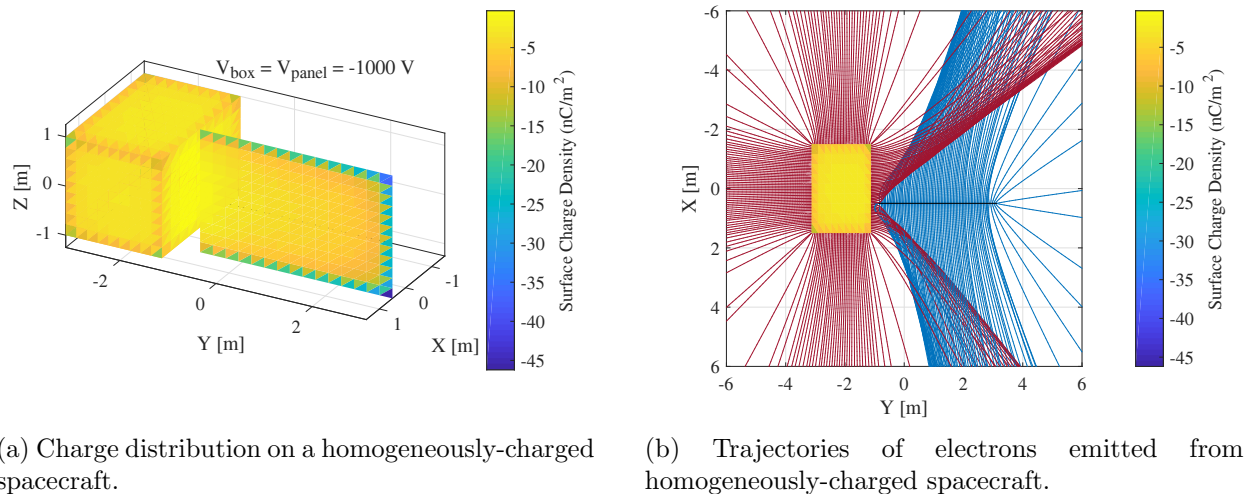
Figure 6.18: Homogeneously-charged spacecraft in which the box and panel are both charged to -1000 V.

homogeneous case. Both electron populations would be measurable in some specific areas.

When an electron beam is used for active sensing, only those surfaces which are hit with the beam generate electrons, so only the potential on those surfaces are sensed. It would be possible to sense the potential of one surface at a time by deflecting and focusing the electron beam to hit a

specific surface. For the passive sensing case, in which sunlight is used to stimulate photoemission, numerous spacecraft surfaces emit photoelectrons simultaneously, so multiple populations may be present in the electron spectra.

6.5   Results & Summary of Research Goal 5

A hybrid MoM-point charge method has been developed for efficient and accurate modeling of electric fields. This approach combines the accuracy of MoM very close to a charged surface with the speed of MSM at larger distances. The numerical program has been used to model various spacecraft-representative shapes. Experiments have been conducted in which a bracket at a large voltage was illuminated with VUV light. The current emitted from the bracket was measured as a function of rotation angle, and agreement is achieved between experiment and simulation. Electron emission from model spacecraft has been simulated for various combinations of boxes, panels, cylinders, and dishes. It is found that concave surfaces and inside corners focus electrons into a localized spatial region, thus creating a large current. Exterior corners and convex surfaces spread electrons out over a large spatial region. This results in a smaller signal, but over a larger area. Either of these cases may be desirable depending on the overall signal magnitude and capabilities of the detector. Finally, experiments and simulations have been conducted to study sensing of differentially-charged targets. Simultaneous touchless sensing of two surfaces at different potentials has been demonstrated.

Chapter 7

Conclusions & Summary

7.1   Research Overview & Contributions

Touchless potential sensing is a technology which is necessary as humankind looks to conduct increasingly complex missions in GEO, cis-lunar space, and beyond. Numerous missions have already been proposed which involve multiple spacecraft flying in close proximity or physically interfacing with each other in harsh charging environments. One of the most advantageous methods for addressing the debris problem at GEO requires knowledge of the potential of a nearby object for closed-loop feedback control during electrostatic actuation. Further, upcoming crewed missions to the Moon must reduce the risk of electrostatic discharge by monitoring and controlling the potentials of spacecraft and other objects in close proximity. This dissertation examines a promising method for touchless sensing which works by measuring the energy of an electron population emitted from the target, and thus, the potential difference between the target and sensor. The work presented herein provides a solid foundation for understanding the electron sensing method and is one of the first studies to consider sensing of potential from a nearby spacecraft. Therefore, this dissertation represents a significant contribution to the fields of spacecraft charging and charged astrodynamics.

First, the prospects and challenges of the electron method have been considered. Numerical simulations have been used to obtain analytical insight into the nature of the problem, and the concept has been shown to be feasible for a wide range of realistic parameters. This resulted in a publication in IEEE Transaction on Plasma Science in 2018 [11].

A space environment simulation chamber has been developed, which has allowed for touchless

sensing experiments to be conducted, and which will be used for future charging and astrodynamics experiments . Further, the invention and development of a broad-spectrum electron gun is a notable contribution to the field of experimental spacecraft-environment interactions research. Numerous studies have been limited by the lack of a tractable and affordable means to generate a spectral electron flux environment, and have thus relied on monoenergetic beams which require simplifying assumptions. This invention has resulted in a patent and generated interest from the spacecraft charging community. Future work will aim to improve the broad-spectrum electron gun and make it widely available to the spacecraft charging and materials communities.

Experiments have been conducted to demonstrate touchless sensing in the laboratory over a wide range of voltages and materials. The experiments have successfully demonstrated the electron method can be used to accurately sense the potential on a target given existing sensor capabilities. Options for sensing both the forced and natural potentials using secondaries from an incident electron beam, photoelectrons from sunlight, and secondaries from the ambient plasma currents have all been considered. This aspect of the work resulted in a paper published in Space Weather in 2019 [14].

Finally, the effects of target geometry have been studied. This involved developing the hybrid Method-of-Moments/point-charge technique for fast and accurate modeling of electric fields and particle trajectories around spacecraft. This led to interesting insight into how the target geometry determines the signal observed by the sensing craft as they move relative to each other. Additionally, it as been shown that the electron method is capable of simultaneously sensing multiple potentials on a differentially-charged target. A publication presenting this aspect of the project is forthcoming.

These results represent considerable progress in advancing the electron method for touchless sensing from a mere concept: strong analytical understanding has been developed and touchless sensing has been demonstrated for realistic scenarios in simulations and experiments.

7.2   Recommendations for Future Work

Several avenues are identified for future work. First, on the simulation side, future studies should continue conducting simulations for additional complex-shaped and differentially-charged targets. Additionally, an important result of Chapter 4 is that the geometry of the target can deflect the incident beam in active sensing cases. Future simulations should incorporate the incident beam expansion and deflection to fully simulate the touchless sensing physics. This would provide valuable insight into the advantages of using a focused beam to sense the potential on one surface at a time versus expanding the incident beam to stimulate emission from all surfaces simultaneously.

On the experimental side, continued laboratory demonstration with representative spacecraft materials would be beneficial. For example, experiments with an actual solar panel coupon or engineering model of a cubesat would help advance the touchless sensing concept to a higher technological readiness level. The ECLIPS vacuum chamber is limited in size, so laboratory demonstrations to date have been constrained to have separation distances on the order of 20 cm. Access to a larger chamber would allow for data to be collected as a function of separation distance. It is possible an experiment could be conducted in parallel during environmental testing for an actual spacecraft or engineering model. An electron sensor could be installed in the chamber to measure photoelectrons or secondary electrons emitted from the spacecraft model when exposed to VUV or electron radiation during day-in-the-life testing. Such experimental results would help raise the electron method for touchless potential sensing to a high technological readiness level. Recent work has proposed testing electrostatic actuation in LEO plasma wakes, as this is a more affordable and accessible environment for flight experiments than GEO, but still provides the necessary plasma conditions for Coulomb forces to exist [80]. Future work should also consider the possibility of testing touchless potential sensing in LEO plasma wakes as an on-orbit technology demonstration which would pave the way to a flight experiment in GEO.

Bibliography

[1] Vacuum diagnosis with an RGA. Application note, Stanford Research Systems, Sunnyvale, CA.

[2] RC Adamo and JE Nanevicz. Development of a continuous broad-energy-spectrum electron source. 1983.

[3] Paul V Anderson and Hanspeter Schaub. Local debris congestion in the geosynchronous environment with population augmentation. Acta Astronautica, 94(2):619–628, 2014.

[4] Neil W Ashcroft, N David Mermin, et al. Solid state physics, 1976.

[5] Vladimir Aslanov and Hanspeter Schaub. Detumbling attitude control analysis considering an electrostatic pusher configuration. Journal of Guidance, Control, and Dynamics, 42(4):900–909, 2019.

[6] V Baglin, J Bojko, C Scheuerlein, Oswald Gröbner, M Taborelli, Bernard Henrist, and Noël Hilleret. The secondary electron yield of technical materials and its variation with surface treatments. Technical report, 2000.

[7] KG Balmain and W Hirt. Dielectric surface discharges: Effects of combined low-energy and high-energy incident electrons. IEEE Transactions on Electrical Insulation, (5):498–503, 1983.

[8] Wolfgang Baumjohann and Rudolf A Treumann. Basic space plasma physics. World Scientific, 1997.

[9] M Bengtson, K Wilson, J Hughes, and H Schaub. Survey of the electrostatic tractor research for reorbiting passive geo space objects. Astrodynamics, 2(4):291–305, 2018.

[10] Miles Bengtson, Joseph Hughes, and Hanspeter Schaub. Remote sensing of spacecraft electrostatic potential using secondary electrons. In The 15th Spacecraft Charging and Technology Conference, 2018.

[11] Miles Bengtson, Joseph Hughes, and Hanspeter Schaub. Prospects and challenges for touchless sensing of spacecraft electrostatic potential using electrons. IEEE Transactions on Plasma Science, 2019.

[12] Miles Bengtson and Hanspeter Schaub. Remote sensing of spacecraft potential at geosynchronous orbit using secondary and photo electrons. In AIAA Scitech 2019 Forum, page 0311, 2019.

[13] Miles Bengtson, Kieran Wilson, and Hanspeter Schaub. Dataset for remote spacecraft charge sensing experiments, 2019.

[14] Miles Bengtson, Kieran Wilson, and Hanspeter Schaub. Experimental results of electron method for remote spacecraft charge sensing. Space Weather, February 2020.

[15] Trevor Bennett and Hanspeter Schaub. Touchless electrostatic three-dimensional detumbling of large axi-symmetric debris. The Journal of the Astronautical Sciences, 62(3):233–253, 2015.

[16] Trevor Bennett, Daan Stevenson, Erik Hogan, and Hanspeter Schaub. Prospects and challenges of touchless electrostatic detumbling of small bodies. Advances in Space Research, 56(3):557–568, 2015.

[17] Trevor John Bennett. On-orbit 3-dimensional electrostatic detumble for generic spacecraft geometries. 2017.

[18] Jay P Boris. Relativistic plasma simulation-optimization of a hybrid code. In Proc. Fourth Conf. Num. Sim. Plasmas, pages 3–67, 1970.

[19] Hajo Bruining. Physics and applications of secondary electron emission. 1954.

[20] CW Carlson, JP McFadden, P Turin, DW Curtis, and A Magoncelli. The electron and ion plasma experiment for fast. In The FAST mission, pages 33–66. Springer, 2001.

[21] M Carruth, Jr, Todd Schneider, Matt McCollum, Miria Finckenor, Rob Suggs, Dale Ferguson, Ira Katz, Ron Mikatarian, John Alred, and Courtney Pankop. Iss and space environment interactions without operating plasma contactor. In 39th Aerospace Sciences Meeting and Exhibit, page 401, 2001.

[22] Anthony W Case, Justin C Kasper, Michael L Stevens, Kelly E Korreck, Kristoff Paulson, Peter Daigneau, Dave Caldwell, Mark Freeman, Thayne Henry, Brianna Klingensmith, et al. The solar probe cup on the parker solar probe. The Astrophysical Journal Supplement Series, 246(2):43, 2020.

[23] W Chang, J Dennison, Jason Kite, and R Davies. Effects of evolving surface contamination on spacecraft charging. In 38th Aerospace Sciences Meeting and Exhibit, page 868, 2000.

[24] David Keun Cheng et al. Field and wave electromagnetics. Pearson Education India, 1989.

[25] Kevin Chou, Andrew Wang, Wiliam Yu, and Joseph Wang. Laboratory experiments on dusty spacesuit charging and arcing in plasma. IEEE Transactions on Plasma Science, 2019.

[26] MS Chung and TE Everhart. Simple calculation of energy distribution of low-energy secondary electrons emitted from metals under electron bombardment. Journal of Applied Physics, 45(2):707–709, 1974.

[27] Martin Ciofalo, Michael Meshishnek, and Amber Hennesy. Space environmental effects exposure testing of space materials. In Applied Space Environments Conference, 2019.

[28] Martin R Ciofalo, Mary E Brady, Christopher J Panetta, and Michael J Meshishnek. Low-energy electron exposure of space materials. Journal of Spacecraft and Rockets, 48(6):931–941, 2011.

[29] Robert Edward Davies. Measurement of angle-resolved secondary electron spectra. PhDT, page 5574, 1999.

[30] VA Davis, BM Gardner, and MJ Mandell. Nascap-2k version 4.3 users manual. Technical report, LEIDOS, San Diego, CA, 2016.

[31] JR Dennison. Dynamic interplay between spacecraft charging, space environment interactions, and evolving materials. IEEE Transactions on Plasma Science, 43(9):2933–2940, 2015.

[32] JR Dennison, Justin Christensen, Justin Dekany, Clint Thomson, Neal Nickles, Robert E Davies, Mohamed Belhai, Kazuhiro Toyoda, Arifur R Khan, Kazutaka Kawasaki, et al. Absolute electron emission calibration: Round robin tests of au and polyimide. In 14th Spacecraft Charging Technology Conference, 2016.

[33] B Dirassen, L Levy, R Reulet, and D Payan. The sirene facility-an improved method for simulating the charge of dielectrics in a charging electron environment. In Materials in a Space Environment, volume 540, pages 351–358, 2003.

[34] BT Draine and EE Salpeter. On the physics of dust grains in hot gas. The Astrophysical Journal, 231:77–94, 1979.

[35] Alex Ellery, Joerg Kreisel, and Bernd Sommer. The case for robotic on-orbit servicing of spacecraft: Spacecraft reliability is a myth. Acta Astronautica, 63(5-6):632–648, 2008.

[36] Heiko JA Engwerda, Joseph Hughes, and Hanspeter Schaub. Remote sensing for planar electrostatic characterization using the multi-sphere method. In Stardust Final Conference, pages 145–161. Springer, 2018.

[37] CL Enloe. High-resolution retarding potential analyzer. Review of scientific instruments, 65(2):507–508, 1994.

[38] B Farr, X Wang, J Goree, I Hahn, U Israelsson, and M Horányi. Dust mitigation technology for lunar exploration utilizing an electron beam. Acta Astronautica, 2020.

[39] Weiquan Feng, Yigang Ding, Dekui Yan, Xuechao Liu, Wei Wang, and Dongmei Li. Combined low-energy environment stimulation test of geosynchronous satellite thermal control coatings. Journal of spacecraft and rockets, 46(1):11–14, 2009.

[40] Dale Ferguson, Stephen White, Richard Rast, and Ernest Holeman. The case for global positioning system arcing and high satellite arc rates. IEEE Transactions on Plasma Science, 47(8):3834–3841, 2019.

[41] Dale C Ferguson. New frontiers in spacecraft charging. IEEE Transactions on Plasma Science, 40(2):139–143, 2011.

[42] Dale C Ferguson, Jeremy Murray-Krezan, David A Barton, JR Dennison, and Stephen A Gregory. Feasibility of detecting spacecraft charging and arcing by remote sensing. Journal of Spacecraft and Rockets, 51(6):1907–1913, 2014.

[43] B Feuerbacher and B Fitton. Experimental investigation of photoemission from satellite surface materials. Journal of Applied Physics, 43(4):1563–1572, 1972.

[44] Angel Flores-Abad, Ou Ma, Khanh Pham, and Steve Ulrich. A review of space robotics technologies for on-orbit servicing. Progress in Aerospace Sciences, 68:1–26, 2014.

[45] Lawrence B Fogdall, Sheridan S Cannaday, and Richard R Brown. Electron energy dependence for in-vacuum degradation and recovery in thermal control surfaces. In Thermophysics: applications to thermal design of spacecraft, pages 219–248. Elsevier, 1970.

[46] HO Funsten, RM Skoug, AA Guthrie, EA MacDonald, JR Baldonado, RW Harper, KC Henderson, KH Kihara, JE Lake, BA Larsen, et al. Helium, oxygen, proton, and electron (hope) mass spectrometer for the radiation belt storm probes mission. In The Van Allen Probes Mission, pages 423–484. Springer, 2013.

[47] James R Gaier. The effects of lunar dust on eva systems during the apollo missions. 2007.

[48] Henry B Garrett and Albert C Whittlesey. Guide to mitigating spacecraft charging effects, volume 3. John Wiley & Sons, 2012.

[49] Luke Goembel. Plasma analyzer for measuring spacecraft floating potential in leo and geo. IEEE Transactions on Plasma Science, 40(2):155–166, 2011.

[50] Michael Goodman, Aurelio Paez, Emily Willis, and Anthony DeStefano. An analytic model for estimating the first contact resistance needed to avoid damaging esd during spacecraft docking in geo. In Applied Space Environments Conference, 2019.

[51] Réjean JL Grard. Properties of the satellite photoelectron sheath derived from photoemission laboratory measurements. Journal of geophysical research, 78(16):2885–2906, 1973.

[52] E Grossman and I Gouzman. Space environment effects on polymers in low earth orbit. Nuclear Instruments and Methods in Physics Research Section B: Beam Interactions with Materials and Atoms, 208:48–57, 2003.

[53] Mike Gruss. Air force seeks info on space weather sensor, June 2015.

[54] MS Gussenhoven and EG Mullen. Geosynchronous environment for severe spacecraft charging. Journal of Spacecraft and Rockets, 20(1):26–34, 1983.

[55] JS Halekas, GT Delory, DA Brain, RP Lin, MO Fillingim, CO Lee, RA Mewaldt, TJ Stubbs, WM Farrell, and MK Hudson. Extreme lunar surface charging during solar energetic particle events. Geophysical research letters, 34(2), 2007.

[56] JS Halekas, GT Delory, RP Lin, TJ Stubbs, and WM Farrell. Lunar prospector observations of the electrostatic potential of the lunar surface and its response to incident currents. Journal of Geophysical Research: Space Physics, 113(A9), 2008.

[57] JS Halekas, GT Delory, RP Lin, TJ Stubbs, and WM Farrell. Lunar prospector measurements of secondary electron emission from lunar regolith. Planetary and Space Science, 57(1):78–82, 2009.

[58] JS Halekas, RP Lin, and DL Mitchell. Large negative lunar surface potentials in sunlight and shadow. Geophysical research letters, 32(9), 2005.

[59] JS Halekas, DL Mitchell, RP Lin, LL Hood, MH Acuña, and AB Binder. Evidence for negative charging of the lunar surface in shadow. Geophysical research letters, 29(10):77–1, 2002.

[60] WB Hanson, S Sanatani, D Zuccaro, and TW Flowerday. Plasma measurements with the retarding potential analyzer on ogo 6. Journal of Geophysical Research, 75(28):5483–5501, 1970.

[61] WB Hanson, DR Zuccaro, CR Lippincott, and S Sanatani. The retarding-potential analyzer on atmosphere explorer. Radio Science, 8(4):333–339, 1973.

[62] Roger F Harrington. Field computation by moment methods. Wiley-IEEE Press, 1993.

[63] Daniel Hastings and Henry Garrett. Spacecraft-environment interactions. Cambridge university press, 2004.

[64] Erik A Hogan and Hanspeter Schaub. Space weather influence on relative motion control using the touchless electrostatic tractor. The Journal of the Astronautical Sciences, 63(3):237–262, 2016.

[65] Joseph Hughes and Hanspeter Schaub. Space weather influence on electromagnetic geosynchronous debris perturbations using statistical fluxes. Space Weather, 16(4):391–405, 2018.

[66] Joseph A Hughes and Hanspeter Schaub. Heterogeneous surface multisphere models using method of moments foundations. Journal of Spacecraft and Rockets, pages 1–8, 2019.

[67] Space Systems – Space Environment – Simulation guidelines for radiation exposure of non-metallic materials. Standard, International Organization for Standardization, Geneva, CH, 8 2010.

[68] JB Jeanneret. Photoemission in lhc-a simple model. CERN SL/Note, pages 97–48, 1997.

[69] S Kasahara, K Asamura, Y Saito, T Takashima, M Hirahara, and T Mukai. Cusp type electrostatic analyzer for measurements of medium energy charged particles. Review of scientific instruments, 77(12):123303, 2006.

[70] Lyon B King, Gordon G Parker, Satwik Deshmukh, and Jer-Hong Chong. Spacecraft formation-flying using inter-vehicle coulomb forces. NIAC Phase I Final Report, 2002.

[71] Jason T Kite. Secondary electron production and transport mechanisms by measurement of angle-energy resolved cross sections of secondary and backscattered electron emission from gold. 2006.

[72] William C Knudsen, Karl Spenner, Jack Bakke, and Vit Novak. Pioneer venus orbiter planar retarding potential analyzer plasma experiment. IEEE Transactions on Geoscience and Remote Sensing, (1):54–59, 1980.

[73] Shu T Lai. An improved langmuir probe formula for modeling satellite interactions with near-geostationary environment. Journal of Geophysical Research: Space Physics, 99(A1):459–467, 1994.

[74] Shu T Lai. Importance of surface conditions for spacecraft charging. Journal of Spacecraft and Rockets, 47(4):634–638, 2010.

[75] Shu T Lai. Fundamentals of spacecraft charging: spacecraft interactions with space plasmas. Princeton University Press, 2011.

[76] Shu T Lai and Maurice Tautz. High-level spacecraft charging in eclipse at geosynchronous altitudes: A statistical study. Journal of Geophysical Research: Space Physics, 111(A9), 2006.

[77] Shu T Lai and Maurice F Tautz. Aspects of spacecraft charging in sunlight. IEEE transactions on plasma science, 34(5):2053–2061, 2006.

[78] Chundong Li, Dezhuang Yang, Shiyu He, and MM Mikhailov. Effect of electron exposure on optical properties of aluminized polyimide film. Journal of materials research, 17(9):2442–2446, 2002.

[79] Chadwick D Lindstrom, James Aarestad, John O Ballenthin, David A Barton, Joseph M Coombs, John Ignazio, W Robert Johnston, Scott Kratochvil, Jeff Love, David McIntire, et al. The compact environmental anomaly sensor risk reduction: A pathfinder for operational energetic charged particle sensors. IEEE Transactions on Nuclear Science, 65(1):439–447, 2017.

[80] Jordan Maxwell and Hanspeter Schaub. Low earth orbit plasma wake shaping and applications to on-orbit proximity operations. IEEE Transactions on Plasma Science, 47(10):4760–4769, 2019.

[81] JP McFadden, CW Carlson, D Larson, M Ludlam, R Abiad, B Elliott, P Turin, M Marckwordt, and V Angelopoulos. The themis esa plasma instrument and in-flight calibration. Space Science Reviews, 141(1-4):277–302, 2008.

[82] Darren McKnight. Pay me now or pay me more later: start the development of active orbital debris removal now. In advanced Maui optical and space surveillance technologies conference, 2010.

[83] Darren McKnight. Examination of spacecraft anomalies provides insight into complex space environment. Acta Astronautica, 2017.

[84] Darren S McKnight and Frank R Di Pentino. New insights on the orbital debris collision hazard at geo. Acta Astronautica, 85:73–82, 2013.

[85] A Mohammadzadeh, H Evans, P Nieminen, E Daly, P Vuilleumier, P Buhler, C Eggel, W Hajdas, N Schlumpf, A Zehnder, et al. The esa standard radiation environment monitor program first results from proba-i and integral. IEEE Transactions on Nuclear Science, 50(6):2272–2277, 2003.

[86] SJ Moss and Ellis Hyman. Minimum variance technique for the analysis of ionospheric data acquired in satellite retarding potential analyzer experiments. Journal of Geophysical Research, 73(13):4315–4323, 1968.

[87] EG Mullen, MS Gussenhoven, DA Hardy, TA Aggson, BG Ledley, and E Whipple. Scatha survey of high-level spacecraft charging in sunlight. Journal of Geophysical Research: Space Physics, 91(A2):1474–1490, 1986.

[88] TA Nordheim, GH Jones, E Roussos, JS Leisner, Andrew J Coates, WS Kurth, KK Khurana, N Krupp, MK Dougherty, and JH Waite. Detection of a strongly negative surface potential at saturn's moon hyperion. Geophysical research letters, 41(20):7011–7018, 2014.

[89] DL Oltrogge, S Alfano, C Law, A Cacioni, and TS Kelso. A comprehensive assessment of collision likelihood in geosynchronous earth orbit. Acta Astronautica, 147:316–345, 2018.

[90] Per-Olof Persson and Gilbert Strang. A simple mesh generator in matlab. SIAM review, 46(2):329–345, 2004.

[91] C Pollock, T Moore, A Jacques, J Burch, U Gliese, Y Saito, T Omoto, L Avanov, A Barrie, V Coffey, et al. Fast plasma investigation for magnetospheric multiscale. Space Science Reviews, 199(1-4):331–406, 2016.

[92] Carolyn K Purvis, Henry B Garrett, AC Whittlesey, and N John Stevens. Design guidelines for assessing and controlling spacecraft charging effects. 1984.

[93] Hong Qin, Shuangxi Zhang, Jianyuan Xiao, Jian Liu, Yajuan Sun, and William M Tang. Why is boris algorithm so good? Physics of Plasmas, 20(8):084503, 2013.

[94] Benjamin B Reed, Robert C Smith, Bo J Naasz, Joseph F Pellegrino, and Charles E Bacon. The restore-l servicing mission. In AIAA SPACE 2016, page 5478. 2016.

[95] James AR Samson and RB Cairns. Photoelectric yield of aluminum from 300 to 1300 å. Review of Scientific Instruments, 36(1):19–21, 1965.

[96] NL Sanders and GT Inouye. Secondary emission effects on spacecraft charging: Energy distribution considerations. In Spacecraft Charging Technology-1978, volume 2071, page 747, 1979.

[97] Scott A Sandford, Edward B Bierhaus, Peter Antreasian, Jason Leonard, Christian W May, Jarvis T Songer, Jason P Dworkin, Dante S Lauretta, Bashar Rizk, et al. Outgassing from the osiris-rex sample return capsule: characterization and mitigation. Acta Astronautica, 166:391–399, 2020.

[98] Lois K Sarno-Smith, Brian A Larsen, Ruth M Skoug, Michael W Liemohn, Aaron Breneman, John R Wygant, and Michelle F Thomsen. Spacecraft surface charging within geosynchronous orbit observed by the van allen probes. Space Weather, 14(2):151–164, 2016.

[99] Abraham Savitzky and Marcel JE Golay. Smoothing and differentiation of data by simplified least squares procedures. Analytical chemistry, 36(8):1627–1639, 1964.

[100] Hanspeter Schaub and Daniel F Moorer. Geosynchronous large debris reorbiter: Challenges and prospects. The Journal of the Astronautical Sciences, 59(1-2):161–176, 2012.

[101] Hanspeter Schaub, Gordon G Parker, and Lyon B King. Challenges and prospects of coulomb spacecraft formation control. Journal of Astronautical Sciences, 52(1):169–193, 2004.

[102] Carl R. Seubert, Laura A. Stiles, and Hanspeter Schaub. Effective coulomb force modeling for spacecraft in earth orbit plasmas. Advances in Space Research, 2014.

[103] J Arol Simpson. Design of retarding field energy analyzers. Review of Scientific Instruments, 32(12):1283–1293, 1961.

[104] Daan Stevenson and Hanspeter Schaub. Multi-sphere method for modeling electrostatic forces and torques. Advances in Space Research, 51(1):10–20, Jan. 2013.

[105] Daan Stevenson and Hanspeter Schaub. Optimization of sphere population for electrostatic multi-sphere method. IEEE Transactions on Plasma Science, 41(12):3526–3535, 2013.

[106] Laura Stiles, Hanspeter Schaub, Kurt Maute, and Daniel Moorer. Electrostatic inflation of membrane space structures. In AIAA/AAS Astrodynamics Specialist Conference, page 8134, 2013.

[107] Laura Stiles, Hanspeter Schaub, Kurt Maute, and Daniel F Moorer. Electrostatically inflated gossamer space structure voltage requirements due to orbital perturbations. Acta Astronautica, 84:109–121, 2013.

[108] WK Stuckey and MJ Meshishnek. Space environmental stability of tedlar with multi-layer coatings: space simulation testing results. Technical report, Aerospace Corporation, 2000.

[109] Erwan Thébault, Christopher C Finlay, Ciarán D Beggan, Patrick Alken, Julien Aubert, Olivier Barrois, Francois Bertrand, Tatiana Bondar, Axel Boness, Laura Brocco, et al. International geomagnetic reference field: the 12th generation. Earth, Planets and Space, 67(1):79, 2015.

[110] MF Thomsen, MH Denton, B Lavraud, and M Bodeau. Statistics of plasma fluxes at geosynchronous orbit over more than a full solar cycle. Space Weather, 5(3), 2007.

[111] Claire Tonon, Carole Duvignacq, Gilbert Teyssee, and Magdeleine Dinguirard. Degradation of the optical properties of zno-based thermal control coatings in simulated space environment. Journal of Physics D: Applied Physics, 34(1):124, 2001.

[112] K Torkar, R Nakamura, Martin Tajmar, C Scharlemann, H Jeszenszky, G Laky, G Fremuth, CP Escoubet, and K Svenes. Active spacecraft potential control investigation. Space Science Reviews, 199(1-4):515–544, 2016.

[113] XD Wang, SY He, and DZ Yang. Low-energy electron exposure effects on the optical properties of zno/k2 sio3 thermal control coating. Journal of materials research, 17(7):1766–1771, 2002.

[114] Elden C Whipple. Potentials of surfaces in space. Reports on progress in Physics, 44(11):1197, 1981.

[115] Phyllis L Whittlesey, Davin E Larson, Justin C Kasper, Jasper Halekas, Mamuda Abatcha, Robert Abiad, M Berthomier, AW Case, Jianxin Chen, David W Curtis, et al. The solar probe analyzers—electrons on the parker solar probe. The Astrophysical Journal Supplement Series, 246(2):74, 2020.

[116] Kieran Wilson, Miles Bengtson, and Hanspeter Schaub. Hybrid method of remote sensing of electrostatic potential for proximity operations. In 2020 IEEE Aerospace Conference, Accepted.

[117] Kieran Wilson and Hanspeter Schaub. Electron-induced x-rays for remote potential sensing. In Applied Space Environments Conference, 2019.

[118] Kieran Wilson and Hanspeter Schaub. X-ray spectroscopy for electrostatic potential and material determination of space objects. IEEE Transactions on Plasma Science, 2019.

[119] Wenfu Xu, Bin Liang, Bing Li, and Yangsheng Xu. A universal on-orbit servicing system used in the geostationary orbit. Advances in Space Research, 48(1):95–119, 2011.

[120] Yang Zhaoming, Zhou Yanping, and Ge Reihong. Charging and discharging of dielectric films irradiated by high-/medium-/low-energy electrons. Acta Astronautica, 15(11):865–870, 1987.